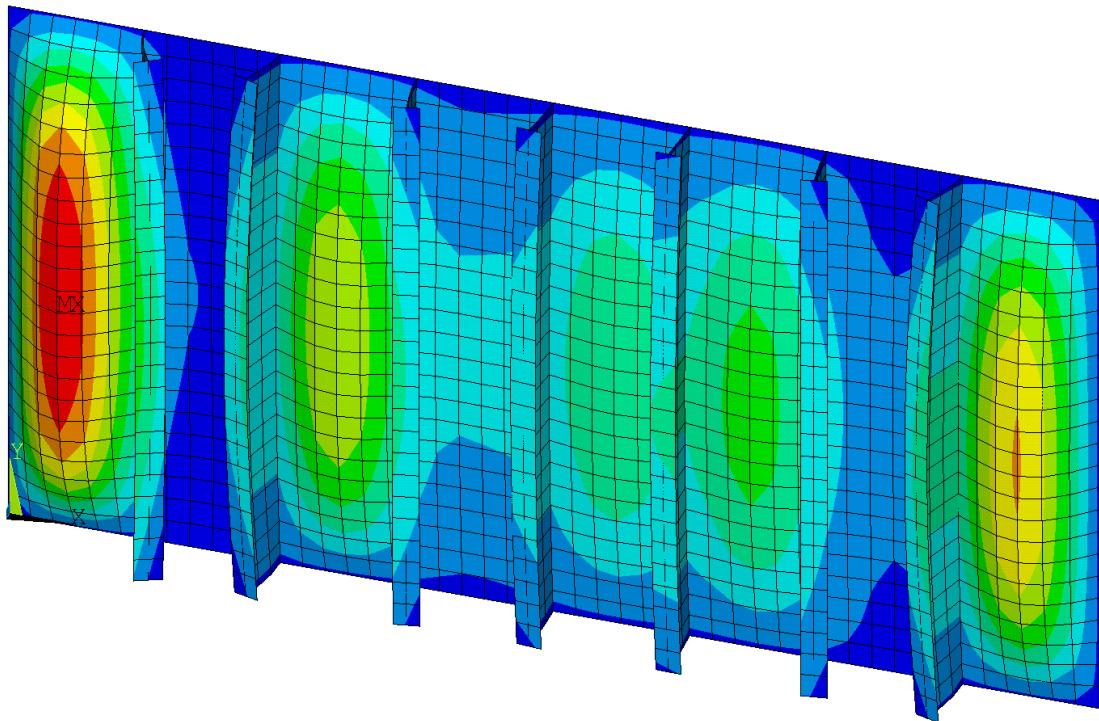


Hydrodynamic load simplification Through Ultimate Strength of a Stiffened Panel

R.W. Bos



Hydrodynamic load simplification Through Ultimate Strength of a Stiffened Panel

by

R.W. Bos

to obtain the degree of Master of Science at the Delft University of Technology, to
be defended publicly on Wednesday October 14, 2015 at 17:30.

Student number: 4114620
Project duration: Januari 1, 2015 – October 14, 2015
Thesis committee: Prof. dr. ir. M.L. Kaminski, TU Delft, Supervisor
Ir. H. Bogaert, MARIN, Supervisor
Dr. E. Lourens, TU Delft
Ir. M.R. Karimi, TU Delft
Dr. ir. P.T.L.M. van Woerkom, TU Delft

This thesis is not confidential.

An electronic version of this thesis is available at <http://repository.tudelft.nl/>.

Abstract

Stiffened panels at the water line of a ship experience in-plane loads due to ship bending and torsion, as well as out-of-plane loads due to wave impacts. Wave impacts weaken the panel with respect to in-plane loads, but are hard to predict because of complex physics. The in-plane strength of the panel supports the surrounding ship structure. Hence, it is important to know in what detail the wave impacts should be determined, while making minimum error in the in-plane ultimate strength.

The importance of load details is evaluated as follows. First, the complex loading is applied to the structure and the ultimate strength of the structure is evaluated. Then, details of the load are omitted, in this case by changing the resolution of the load. Finally the effect of omission of details becomes clear, by comparing the ultimate strength of different wave impact load resolutions.

Non-linear finite element calculations are performed to assess the unloaded ultimate strength, as well as the ultimate strength for different load resolutions. The load is a breaking wave on a rigid wall. Applied resolutions range from 0.1 m to uniform pressure over the stiffened panel.

It is found that the ultimate strength under static loading either over- or underpredicts the ultimate strength of the panel independent of resolution. Further, the ultimate strength under a dynamic uniform loading is also not representative. Different resolutions are, again, of minor influence. Tests with a different panel confirm the findings.

It is therefore concluded that, for the load and structure under investigation: there is little effect of load resolution, as long as it grossly resembles the pressure map. Dynamic calculations should be performed at all times.

Definitions and nomenclature

Definitions

ALPS/ULSAP	Semi-analytical method to determine the ultimate limit state of a structure, developed at Pusan University in South Korea.
Buckling	Displacement of a structure perpendicular to load direction often leading to loss of stability.
Collapse	Inability of a structure to sustain further loading.
Detail	Small feature of a pressure map, such as local peaks.
DNV/Puls	Semi-analytical method to determine the ultimate limit state of a structure, developed by Det Norske Veritas.
Failure	Moment from which a structure can no longer fulfil its task.
FEM	Finite Element Method, approximation technique often used to determine structural response.
FPSO	Floating Production Storage and Offloading unit, a floating structure used in offshore industry.
In-plane	Used to describe loading or displacement in the same plane as the ships hull.
Instability	Denotes a situation in which a motion no longer comes back to an equilibrium position.
ISUM	Idealized structural unit method, a semi-analytical method used to predict collapse behaviour of structures by subdivision in structural units.
Lateral	Denotes loading or displacement normal to the plane of the ship hull.
Limit state	State which limits operation of a structure. In this thesis the ultimate limit state is often used, which denotes extreme loading during normal operations.
Out-of-plane	See lateral
Paik	Metonymia used for the work of Paik, consisting of recent developments building on ISUM, mainly Paik and Thayamballi 2003b.
Plasticity	Irreversible process in which deformation remains after unloading.
Resolution	Information density of a pressure map.
US/ULCC	Ultimate strength, ultimate load carrying capacity. After this point collapse follows.
Wave impact	Very fast loading of a structure by a breaking wave.
Yield	Stress level after which plasticity starts.

Nomenclature

a	Stiffener spacing (m).
-----	------------------------

A	Total panel height (m).
$A_{m/s}$	Initial deformation (mm). Interpanel or stiffener initial out of plane deformation.
b	Stiffener length (m).
\mathcal{B}	A body.
\mathbf{C}, \mathbf{E}	Cauchy-Green and Green strain tensor.
\mathcal{C}	Linearized fourth order material tensor.
\mathbf{D}	Material properties \mathcal{C} in Voigt notation.
E	Elastic modulus (MPa).
\mathbf{F}	Deformation gradient.
G, Λ	Lamé constants.
\mathbf{g}	Basis vector.
J	Jacobian of deformation gradient.
p	Pressure (MPa). Uniform lateral pressure on a stiffened panel.
R	Residual.
\mathbf{U}, \mathbf{u}	Displacement field, from Lagrangian and Eulerian perspective.
\mathbf{t}	Traction.
\mathbf{X}, \mathbf{x}	Reference and current configuration, from Lagrangian and Eulerian perspective.
α	Displacement control angle ($^{\circ}$). Defined in Equation 4.1.
γ	Vector weight function.
δ	Shortening (-). Dimensionless shortening of a stiffened panel.
δ_c	Critical shortening (-). Dimensionless shortening of a stiffened panel at which the panel reaches its ultimate strength.
δ_{ij}	Kronecker delta.
ϵ	Strain in Voigt notation.
ϵ_{ij}	Strain (-). Numerical indices denote strain components.
ζ	Initial deformation (m). Defined in Equation 2.4.
λ	Eigenvalue buckling load (-).
ν	Poisson ratio (-).
ξ_i	Natural coordinate.
ρ	Density (kg/m^3).
$\boldsymbol{\sigma}, \mathbf{P}$	Cauchy and Piola-Kirchhoff stress tensor.
σ_{ij}	Stress (Pa, MPa). Numerical indices denote the stress components. Textual components denote stages of yield as denoted in Table 2.1.
σ_{fore}	Fore reaction stress (Pa, MPa). Reaction force on fore end of panel, divided by the area.
σ_{top}	Top reaction stress (Pa, MPa). Reaction force on top end of panel, divided by the area.
σ_{Yeq}	Yield equivalent stress (Pa, MPa). Defined in Equation 2.2, a measure of yield stress combined with load area.
$\sigma_{x/y}$	Stress (MPa). Used by Paik to denote the stress on the fore or side end of the panel.
τ	Shear stress (MPa).
ψ	Strain energy.
$\boldsymbol{\psi}$	Shape function in vector format.
ω	Angular velocity (rad/s).
$\Omega, \bar{\Omega}$	Domain of an element, unit domain of an element.

Contents

Abstract	i
Definitions and nomenclature	iii
1 Introduction	1
1.1 Wave loads on ship and offshore structures	2
1.2 Structural response	3
1.3 Problem and methodology	5
1.4 Thesis outline	5
2 Ultimate Limit State Assessment	7
2.1 Direct calculations using finite element method	8
2.2 Idealized structural unit methods	10
2.3 Example ultimate limit state calculation	13
2.4 Ultimate limit state with complex loadings	17
2.4.1 Approach	17
2.4.2 Parameters	18
2.4.3 Limitations	20
3 Finite Element Method	21
3.1 Governing equations in solid mechanics	21
3.1.1 Kinematics and strain	21
3.1.2 Stress and balance	22
3.1.3 Material model	23
3.2 Kinematic assumptions and limitations	25
3.2.1 Beams	25
3.2.2 Plates	26
3.2.3 Shells	26
3.3 Methods of weighted residuals	27
3.4 Element formulation	28
3.4.1 Linear solid element	29
3.4.2 Shell element	32
3.4.3 Solution strategies	32
3.5 Discussion	33
4 Model Development	35
4.1 Panel geometry	35
4.2 Boundary conditions	37
4.3 Elements and mesh	37
4.4 Geometric imperfections	40
4.4.1 Eigenvalue analysis	40
4.4.2 Quasi-static analysis	41
4.5 Biaxial strength	45
4.6 Discussion	46
4.6.1 Evaluation of results	46
4.6.2 Recommendations	47

5	Simplified Load Application	49
5.1	Load description and simplification	49
5.2	Dynamic pressure comparison	55
5.2.1	Breaking wave	55
5.2.2	Flip-through	61
5.2.3	Other scantlings	63
5.3	Static pressure comparison	67
5.4	Discussion	70
5.4.1	Evaluation of results	70
5.4.2	Further possibilities	71
6	Conclusions	73
6.1	Thesis goal	73
6.2	Main question	73
6.3	Recommendations	74
A	Classification of failure	77
B	Detailed results analysis	79
B.1	Dynamic load analysis $h = 0.1$ m, breaking wave	79
B.2	Dynamic load analysis $h = 2.0$ m, breaking wave	83
B.3	Dynamic load analysis $h = 7.64$ m, breaking wave	87
B.4	Dynamic load analysis $h = 0.1$ m, flip-through	90
C	Result tables	95

1 Introduction

Waves cause the most common yet complicated loads on ship and offshore structures. The hull of a ship is designed to withstand these loads, based on experience of previous designs and complex mathematics. To simplify the calculations, the hull can be seen as an assembly of simple elements, such as beams, plates and stiffened panels. Figure 1.1 shows an floating production storage and offloading unit (FPSO), of which one stiffened panel is highlighted.



Figure 1.1: An FPSO in offloading condition¹. Top left corner shows three wave impact loads from Guilcher et al. 2014, bottom right corner a limit state of Paik and Thayamballi 2003b and a stiffened plate field: the structure under consideration in this work.

This panel experiences different kinds of loadings: the global deformations of the ship due to long waves, wave impacts and loads of ballast tanks in the double hull. The bottom right corner of Figure 1.1 shows a detailed model of the stiffened panel. This

¹Figure from Bluewater <http://www.bluewater.com/wp-content/uploads/2013/02/4.1-Image-3-FPSO-Offloading.jpg>



Figure 1.2: A ship in waves, experiencing wave impacts.

stiffened panel is initially deformed (exaggerated in the picture), for instance during construction due to the welding. These initial deformations weaken the panel, as they are often similar in shape as a dangerous failure mode: buckling.

In the top left corner a detailed picture of a wave impact is shown. These impacts are extremely challenging to model and give very high, very local peaks, with a very short duration. These loads act on the side of the stiffened panel. Global deformations from hull bending and torsion exert loads in the plane of the stiffened panel. When these processes result in small deformations, they can be assumed to be uncoupled. However, for the most extreme situations such as harsh storms they will result in large deformations which interact with another. It is for these situations that in this thesis the relevance of the wave impact is investigated.

This chapter continues with an explanation of waves, both where they come from and how they are predicted. Then, the methods of determining structural response are evaluated. A gap becomes apparent, from which the methodology of this thesis is developed.

1.1 Wave loads on ship and offshore structures

The sea surface is formed by waves, caused by events propagating over large distances. Waves consist of swell and wind waves: swell is a long wave, whereas wind waves are short. Falinsen 1990. Ships encounter these waves, hence they experience complex combinations of loading. The most complex loads are impact loads, examples shown in Figure 1.2. These loads are characterized by multiple physical phenomena, such as wave breaking and gas entrapment, and are very localized in space and time. In general multiple approaches to predict loads can be distinguished.

Structures in the water are deformed by waves, and the deformation are the most dominant considering the ship as a beam over the length. The easiest way to predict wave loads on structural members is by class rules. Based on a few parameters, such as ship length and an assumed mass distribution, the maximum wave bending moment in 20 years is estimated.

A more advanced way to calculate longitudinal strength loads is by using a potential flow code, often solved with the boundary element method, see Larsson and Raven 2010. The potential flow is based on the assumption that there is some potential function $\phi(t, x, y, z)$, of which the gradient denotes the flow velocity, without viscosity or vorticity. On the hull the water is not allowed to flow through the hull (kinematic

boundary condition). The free surface has to have a pressure equal to the atmospheric pressure (dynamic boundary condition). At the bottom the velocity in z direction is zero and at the far field the flow is undisturbed. The pressures are calculated using Bernoulli's equation, which is valid along the path of a fluid particle, the stream line.

Instead of assuming a potential flow the loads can also be determined using the Navier Stokes equations. This is a momentum balance with a shear force model, Larsson and Raven 2010. The Navier Stokes equations can be solved using a volume of fluid method, where the domain is divided in numerous small cells, over which physical quantities are assumed to be constant, see Ferziger and Perić 2002 for numerical methods. Hence, to capture local effects such as eddies, a great number of cells are required. Besides that, a ship in rough seas has a free surface which evolves constantly, which becomes even more complex with breaking waves. As physical complexity increases, so does the computational challenge which is reflected in long calculation times for even simple academic problems.

Experimental research makes it possible to include all the physics by choosing the right test setup. Sensors are placed to measure relevant quantities, for instance wave impact pressures. The difficulty is, that these results are not directly usable for design. After all, the measured data is highly dependent on sensor size and placement, another experiment might yield another load. For different scales, such as model scale compared to full scale, the transfer of loads is not straightforward. It requires scaling according to scaling laws relevant to the physical phenomenon. However, often multiple physical phenomena are present, with quite different scaling laws. Hence it is not straightforward or possible to directly use the results of one scale on another scale. Some of the difficulties in obtaining and scaling tests from wave impacts, with very local effects, can be found in Lafeber, Brosset, and Bogaert 2012.

1.2 Structural response

The structure is designed to withstand external wave loads and able to carry the internal loads from the cargo. Classification societies have set up rules prescribing minimum scantlings required to be safe enough for the lifetime. Ships are typically designed for a lifetime of 20 years, and offshore structures can be designed for up to 40 years.

Failure of the vessel is to be avoided at all cost, but is complex to predict due to multiple failure mechanisms. The border between safety and failure is denoted as the limit state, first defined in the Eurcode (The European Union 2002). In shipbuilding four limit states are defined, for instance by Paik, Wang, and Thayamballi 2002:

- **Serviceability limit state (SLS):** This limit state is reached when the structure is not able to perform its normal tasks, due to deterioration of non-vital functions. An example is excessive vibration, which is most annoying and prohibits work, but is not life threatening.
- **Fatigue limit state (FLS):** Cyclic loading of a structural member can lead to fatigue, which is a cumulative damage mechanism often modelled stochastically. Ships decks and double bottoms are often strengthened against fatigue damage, since they carry a large part of the longitudinal bending moment. If the strengthening is not enough, the fatigue damage adds up and can come to a point of failure.
- **Ultimate limit state (ULS):** High loads may lead to failure right away, which connects the ULS to 'plastic collapse' and 'ultimate strength'. The loads leading to ULS occur by definition during normal operations.

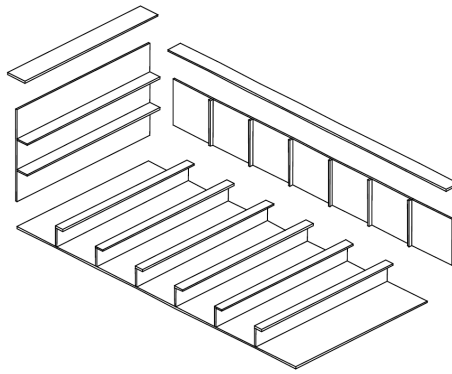


Figure 1.3: *Assembly of stiffened panels, one of the possible divisions of the ISUM method, Paik, Wang, and Thayamballi 2002. In this figure a structure is divided in three stiffened panels and two girders. Alternatively, unstiffened panels can be modelled.*

- **Accidental limit state (ALS):** Any limit state reached due to accident or misuse fall under the accidental limit state. Examples are grounding or fire, which accidentally occur but are certainly not normal operations.

The finite element method allows for modelling the geometry of the structure accurately, as well as modelling complex non-linear equations. The results rely very much on the placement of the elements (mesh), numerical solvers and the user. In shipbuilding, the finite element method is used for different design stages levels of the design. Reaching a maximum stress or strain during a simulation is considered as reaching the ULS.

The global vessel can be described by a beam with variable cross-section and the locally stiffened panels can be modelled using shell elements. This allows for modelling on multiple scales, without being restricted to geometry or load. The finite element method may be used to assess the limit states, depending on the loading condition, such as cyclic loading of wave bending moments or a wave impact load.

Another way to assess the ultimate strength of a ship is the idealized structural unit method (ISUM) and its successors, as described by Paik and Thayamballi 2003b. In this method the ship is divided in a number of idealized components: unstiffened or stiffened panels and girders. Figure 1.3 shows a possible subdivision by the ISUM method, where each stiffened panel is a component. The components are loaded by simplified loading conditions, a linear varying pressure on the sides, constant shear force and constant lateral pressure. Based on the geometry a maximum loading capacity can be determined: the ultimate strength. When the ultimate strength of a component is reached, it will no longer be able to carry an increase in load and collapses. The load then has to be carried by the surrounding structure, for which a similar analysis can be performed. This example shows the best use for this method: the analysis of the collapse of a structure. The ISUM method is used to assess the ULS, and is recommended in International Association of Classification Societies 2012.

By applying the class rules we can design a structure which can be analyzed, using FEM or ISUM. The former can be used for the most complex cases but is very demanding, the latter is simple to use but does not have the capability to assess complex cases.

1.3 Problem and methodology

From previous paragraphs the tendency is apparent to determine the load in as much detail as possible, whereas the structure is calculated by quite rough methods, without regard for highly complex local impact loads. Hence, the question is:

In what detail do loads need to be predicted, in order to predict structural failure?

The goal of this thesis is to: *develop a method to assess the maximum loss of resolution of a pressure map, while retaining the ability to predict failure of the local structure.* Two sub-questions have to be answered before the goal can be reached:

- How are limit states and failure modes described?
- How is the response of an arbitrary structure determined?

These questions are answered in Chapters 2 and 3.

The stiffened panel has under the wave impact a different ultimate strength than without wave impact. Different resolutions of the pressure map, which represents the wave impact, also influence the ultimate strength of the panel. It is considered that the best method to compare different pressure map resolutions, is by comparing the ultimate strength because reaching the ultimate strength is to be avoided at all times.

1.4 Thesis outline

First, the failure of structures will be discussed in Chapter 2 using two methods: structural unit methods and the finite element method. A sample calculation will be made, comparing different failure criteria. It will become clear that the finite element method has to be used with the ultimate load carrying capacity criterium. In Chapter 3 the finite element method is explained, starting from continuum mechanics and ending with the explanation of the mathematics behind this well-known method.

The knowledge of these two chapters will be applied in the model development and tests of Chapter 4 and Chapter 5. First the structural model is explained and a mesh convergence study is done. After that, a wave impact load is applied to the structure and its effects are investigated. Finally, the conclusions are presented.

2 Ultimate Limit State Assessment

As stated in the Chapter 1, the ultimate limit state is defined as the point of collapse of a structure. It occurs in the most extreme case of normal operation. Accidents are not included. The goal is to avoid failure of the vessel. But how could one define failure of the vessel, or of a component? A conceptual representation is given in Fig. 2.1, where a typical force-displacement plot is drawn. At first the relation is linear or proportional, after which softening occurs. After some displacement into the non-linear region buckling occurs (A), this is however stable buckling: the load still increases with the displacement. The breakdown point of the curve is the ultimate strength (B). After ultimate strength comes collapse, and is generally unstable: the structure is not able to carry the load anymore.

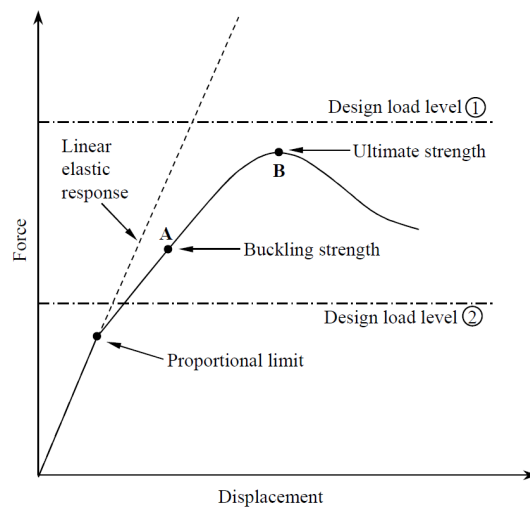


Figure 2.1: Force-displacement plot illustrating ultimate strength and two design load levels, from Paik, Wang, and Thayamballi 2002.

The question now rises where the feasible ultimate limit state is. In Figure 2.1 two design load levels are drawn. The first one is above the ultimate strength, reaching this state will lead to failure of this component. It may however still be a safe design load level when the rest of the structure is able to resist the extra loading. The second design load level is safe, as it is below the ultimate strength, it is however quite conservative and will lead to overdimensioning.

In this chapter two methods of determining the limit state are examined. The first is following the class rules for assessment of ship and offshore structures using the finite element method. In this section it is explained how FEM strength calculations are usually performed, the requirements for a good simulation and what failure criteria are used. The second is the ultimate limit state design as proposed by, among others,

J.K. Paik. Here the ultimate limit state is determined by semi-analytical equations for the stresses in the panel, describing the global behaviour of a stiffened panel. We will see that the method of Paik is simple to use and reliable for the failure it predicts. It lacks however the ability of FEM to have complex loading. Therefore an example is given where the failure criteria of FEM are compared to these of Paik. Then, a new approach is developed, which is applied to determine the relevance of lateral loads on ship and offshore structures.

2.1 Direct calculations using finite element method

The analysis of the structure is, according to *Rules for the classification of ships 2015* or Okumoto et al. 2009, subdivided in three levels. The first is the global analysis, which considers the ship as a beam and therefore provides the normal and shear stresses on structural units. Second, the cargo hold analysis is to determine the strength of primary stiffeners (girders and stringers), which carry large parts of the cargo. Last, the local structure analysis investigates the stresses in stiffeners, which are laterally loaded and supported by brackets. These analysis can be done as one calculation, or considered separately. The following rules and guidelines are used for calculations appropriate to the stiffened panel.

In the rules for the classification of ships direct strength calculations can be mandatory to check the chosen scantlings, *Rules for the classification of ships 2015*, Pt. 1, Ch. 2, Sec. 1C. These direct calculations can be performed by hand or finite element methods, provided that they include, for stiffened panels, in-plane, bending and shear stresses. In reporting, special attention should be given to boundary conditions and end brackets, effective shear area, effective plate width and the different loading types. Maximum stress values are put on different structural members, as long as the structure does not exceed these maximum values the design is admitted. The maximum stress is lower than the yield stress of the material, hence the structure remains in the elastic region.

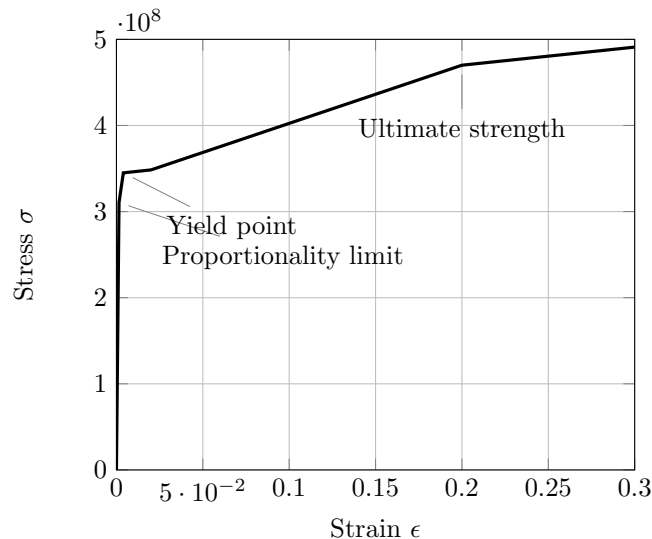


Figure 2.2: Material model example given by DNV in *Det Norske Veritas AS 2013*, p. 18 for S355 steel with a thickness of $16 \text{ mm} < t < 40 \text{ mm}$. Values in Table 2.1.

The importance of remaining in the elastic region becomes clear in Figure 2.2: a stress-strain diagram, with corresponding values in Table 2.1. This material (S355) is described in *Det Norske Veritas AS 2013*, p. 17-21, for the average thickness of

Table 2.1: Proposed material model as given by DNV in Det Norske Veritas AS 2013, p. 18 with a thickness of $16 \text{ mm} < t < 40 \text{ mm}$. Engineering stresses.

E	210,000	MPa
$\sigma_{\text{prop}}/\sigma_{\text{yield}}$	0.9	
E_{p1}/E	0.001	
σ_{prop}	310.5	MPa
σ_{yield}	345	MPa
σ_{yield2}	348.4	MPa
σ_{ult}	470	MPa
$\epsilon_{\text{p y1}}$	0.004	
$\epsilon_{\text{p y2}}$	0.02	
$\epsilon_{\text{p ult}}$	0.15	
E_{p2}/E	0.0043	
ν	0.3	
ρ	7850	kg/m ³

$16 \text{ mm} < t < 40 \text{ mm}$. At first the curve is straight, this is the elastic regime. At a certain strain the material yields and softens. The other stages describe further the softening of the material, until the ultimate strain is reached: at this strain the material ruptures. The material model shown in Figure 2.2 is also the typical outcome of material strength tests. These results are used in FEM by taking the Von Mises stress, which is a stress measure invariant of the coordinate system, Lubliner 2008 and Holzapfel 2000.

$$\sigma_v = \sqrt{\frac{(\sigma_{11} - \sigma_{22})^2 + (\sigma_{22} - \sigma_{33})^2 + (\sigma_{33} - \sigma_{11})^2 + 6(\sigma_{12}^2 + \sigma_{23}^2 + \sigma_{31}^2)}{2}} \quad (2.1)$$

Note that all the stress components are taken into account, hence the failure criterion is not uniaxial and can universally be applied. More details about yield, flow and hardening are explained in Paragraph 3.1.3.

Linear calculations may not be sufficient to determine the ultimate strength of a structure. Two additional non-linear phenomena come into play: instabilities such as buckling, and non-linear material behaviour such as shown in Figure 2.2. Not taking material behaviour into account is not a conservative approach when the yield stress is exceeded. While buckling may be predicted using linear (eigenvalue) methods, the buckling does not necessarily lead to collapse. Imperfections are often not taken into account correctly using eigenvalue buckling. Hence, the buckling analysis using non-linear finite displacement methods is important as well.

Guidelines for non-linear strength calculations are for instance presented by Det Norske Veritas AS 2013. The stresses predicted by linear analysis are often in the non-linear region, but no additional analysis is performed to check the safety of the design. Accumulation of plastic deformation may however be important when variable loading is considered, for instance in wave loads. Often materials are assumed to be ductile as opposed to brittle, whereas this depends on temperature and strain rate: a lower temperature or higher strain rate increases the elastic modulus but decreases the rupture strain. In the most extreme case, the structure is loaded fast enough to cause brittle failure, which generally propagates easily through the structure, more details in Shoemaker 1981. When ductile failure is considered, the criteria for failure are critical strain, or an arbitrary criterium obtained by comparison with test results.

While non-linear calculations may certainly improve assessment of structures, it comes at a cost of increased work. The results may be sensitive to another plate thickness or

loading condition, while this is not clear from the analysis. Thus, these results must be regarded with healthy caution. One of the clear downsides of FEM as described here, is that the failure modes are very local. Local stresses might not lead to failure of the structure or even be physical, such as stress concentrations at the boundaries due to constraints.

2.2 Idealized structural unit methods

Failure of the ship is not dictated by one structural member, but the collapse of multiple members. It is therefore necessary to investigate whether the collapse of one member leads to the collapse of other members. It is possible to assess this with the finite element method, using non-linear material models. It is however rarely feasible to do so, since a non-linear model with the size of a ship is too large to calculate, especially considering all the different cases in which it can fail.

Many examples exist of successfully applying analytical or (semi-)empirical equations for the analysis of ship structures, Paik and Thayamballi 2003a. It started in the 1970s with a paper by Ueda and Rashed 1974 in Japan and not long after that Smith 1977 developed a similar method in the United States. Both approaches and successors work as follows: the structure is divided in a number of structural members (units), stiffened plates and decks, as shown in Figure 1.3. These members are connected in a similar way as finite elements are connected. A load is applied which might lead to failure of one of the members. After that the progressive collapse of the other members is calculated. This is possible for large structures since the equations are straightforward.

A method developed, among others, by J.K. Paik considers three structural units: an unstiffened panel, a stiffened panel and a girder. For each unit and mode a failure point is defined using semi-analytical equations for a uniaxial case. These failure points can be combined into a failure surface therefore defining the failure of the structure.

A stiffened panel has six ways of reaching its ultimate limit state, the first five are shown in Figure 2.3¹:

- Mode I: Overall collapse of plating and stiffeners as a unit: in this limit state the stiffeners are small, and can be considered to be smeared out over the panel. The panel then buckles under compressive loading. The buckling is however not the point of failure, since it might be elastic or stable buckling. Therefore the maximum stress is calculated at the shaded regions. The external forces for which the maximum stress exceeds the yield point is taken as maximum load. Steel used in shipbuilding experiences significant softening after the yield point, as shown in Figure 2.2.
- Mode II: Biaxial compressive collapse without failure of the stiffeners: when the stiffeners are strong enough, they will not fail under compressive loading. The interstiffener plating will however fail. Hence, in Figure 2.3b the stiffeners are not deformed and the shaded region, defining the collapse, is located on the plate at the end of the stiffener.
- Mode III: Beam-column type collapse: a collapse dominated by the plate-stiffener combination, where the plate and stiffener both collapse. In determining the ultimate strength of this collapse type only the most stressed stiffener plate combination is examined. The limit state is reached when the extreme fibres of the stiffener yield.

¹Collapse mode names literally copied. Description from Paik and Thayamballi 2003b.

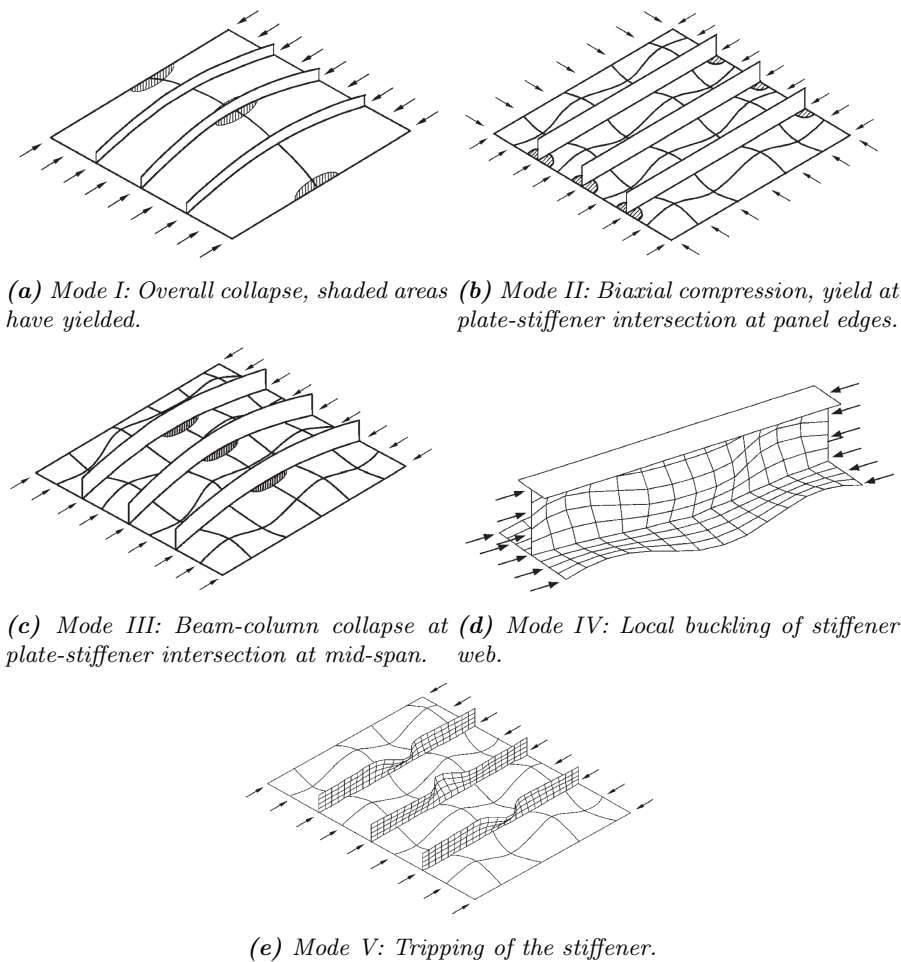


Figure 2.3: Five collapse modes of a stiffened panel. Figures from Paik 2010. The shaded regions denote yield of the material, gridded areas which are deformed denote buckling or tripping.

Mode IV: Local buckling of the stiffener web: thin plates tend to buckle easily under compressive loads, as happens in this collapse mode. The web is not thick enough, causing it to buckle. After buckling it will not be able to sustain further loading, hence the stiffened panel will reach its ultimate limit state.

Mode V: Flexural-torsional buckling or tripping of the stiffeners. Excessive loading causes the stiffeners to rotate, through which they lose their strength. This failure typically takes place with stiffeners with low torsional rigidity.

Mode VI: Gross yielding: this collapse occurs when the panel fails without buckling first.

The maximum loading of each collapse mode depends only on the geometry and material properties of the structure. Observe that the failure modes of Paik are well defined, hence the failure criteria of stress and stability can easily be applied. The first three and sixth failure modes use an allowable stress criterion in the shaded regions. The fourth and fifth failure mode use the point of buckling as ULS.

The validity of the method has for instance been shown in Paik, Kim, and Seo 2008, where a comparison of the aforementioned failure loads has been made with FEM, with good results. This comparison is shown in Figure 2.4. Two implementations of structural unit methods are used: ALPS/ULSAP from Pusan University and DNV

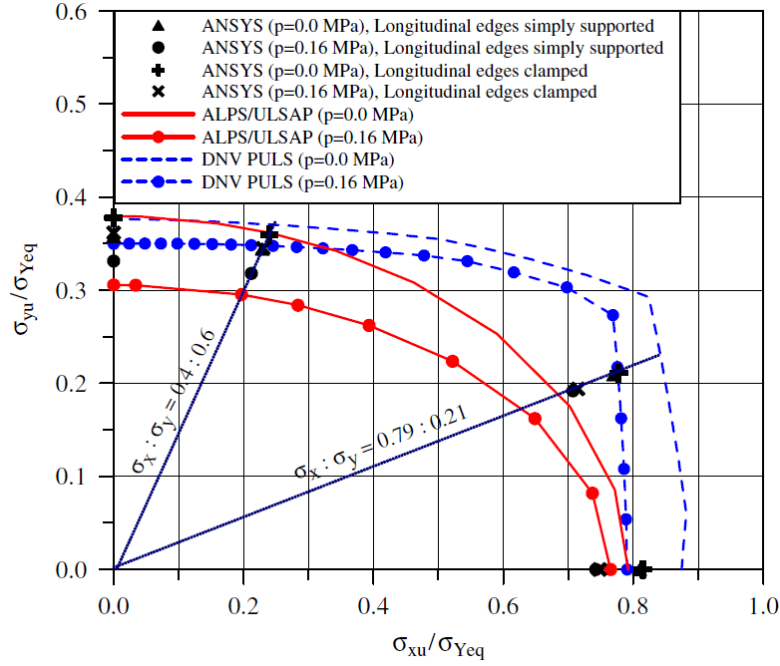


Figure 2.4: Ultimate limit state determined using FEM and two structural unit methods, Paik, Kim, and Seo 2008. Each line denotes a failure surface, calculated with semi-analytical formulations (ALPS/ULSAP and DNV PULS) as well as with full non-linear buckling/plastic analysis in Ansys.

PULS from Det Norske Veritas. These plots will be used throughout the report to show the ultimate strength (US) of a structure and should be read as follows. On the horizontal axis and vertical axis a dimensionless average stress on the side of the panel is plotted.

$$\frac{\sigma_{xav}}{\sigma_{Yeq}} = \frac{F_x}{A_x \sigma_Y} \quad (2.2)$$

where σ_{xav} ² denotes the average stress around the boundary, σ_{Yeq} is the yield equivalent stress taking into account the total area of the side of the structure (including stiffeners), F_x is the total reaction force, A_x is the total area (including stiffeners) and σ_Y is the yield stress of the material. The left hand side is from here on also called reaction stress ratio. The points in the graph show for which combination of loads the panel has failed, and a line through all of them from the failure surface of the panel³.

The procedure which Paik proposes, uses the maximum load of each individual collapse mode for each loading case: uniaxial compression in two directions, and shear. The lateral pressure is taken into account in all calculations. The collapse loads are then inserted into:

$$\left(\frac{\sigma_{xav}}{\sigma_{xu}^I} \right)^{c_1} - \alpha \left(\frac{\sigma_{xav}}{\sigma_{xu}^I} \right) \left(\frac{\sigma_{yav}}{\sigma_{yu}^I} \right) + \left(\frac{\sigma_{yav}}{\sigma_{yu}^I} \right)^{c_2} + \left(\frac{\tau}{\tau_u^I} \right)^{c_3} = 1 \quad (2.3)$$

²Later on, the subscript is changed to denote the fore or top end of the stiffened panel.

³The failure surfaces are not drawn, for two reasons. The first is, that the value on the horizontal and vertical axes are not known, and determining them would require other boundary conditions. The second point is, that drawing the line would imply knowledge of the surface, which is not necessarily present.

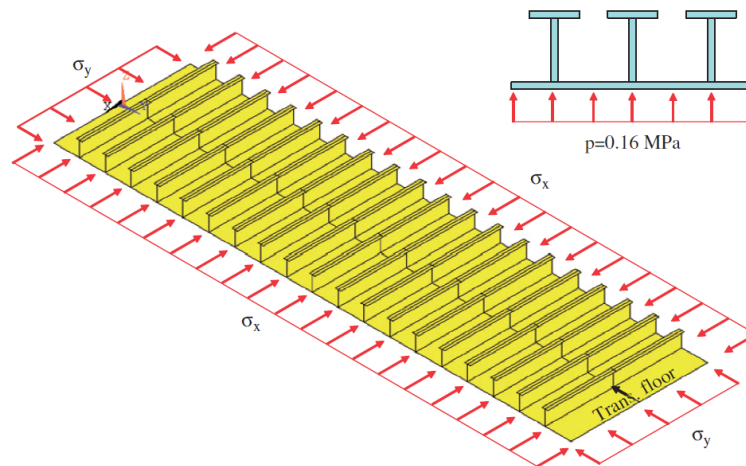


Figure 2.5: Stiffened panel geometry of a bottom structure, for test case of different Ultimate Limit State assessments, from Paik, Kim, and Seo 2008. The sides of the panel are loaded in-plane with σ_x and σ_y and the entire panel is subject to a uniform lateral load of $p = 0.16$ MPa.

which describes the yield surface. The numerators are the applied loads and the denominators the maximum loads determined for that single load case. The exponents $c_{1...3}$ are commonly chosen as 2, and α depends on tension or compression loading. The result is a failure surface described by the stresses in the numerator, where the failure surface is similar to the Von Mises criterion. Note that each collapse mode has its own failure surface, and this allows the formation of the failure surface for the unit structure.

Note that quite some assumptions surround this method. The construction is assumed to fail in one of the six predefined ways. These ways are calculated using a maximum allowable stress approach, hence the ultimate strength is determined by looking at very local stress concentrations. The uniform loading is applied quasi-static, hence dynamic or local effects are not taken into account. Naturally, it is possible to use a safety or dynamic amplification factor to be on the safe side, but these factors have to be determined as well. Finally, it should be noted that a Von Mises criterion is used, which extrapolates the uniaxial cases to biaxial cases. In the authors opinion, this might work for linear calculations, but not necessarily for non-linear calculations, as the failure modes cannot simply be assumed to have no interaction.

2.3 Example ultimate limit state calculation

Here an example is presented of a simulation, to determine the ultimate limit state of a stiffened panel. It is used as a test case for the script files developed in Chapter 4. Similar simulations were chosen as in Paik, Kim, and Seo 2008, where a bottom structure of an oil tanker is investigated. Alternatively the results of Özgüç, Das, and Bartrop 2007 could be used, who compares far more cases as well as experimental results. However, it seems appropriate to use the results of Paik, who compares the FEM results to well established ways of calculating the ultimate limit state.

The simulated panel is the bottom of a longitudinally stiffened oil tanker and has the dimensions stated in Table 2.2. Figure 2.5 shows the problem geometry. Initial

deformations are given by following:

$$\zeta = A_m \left| \sin \frac{\pi x}{a} \sin \frac{\pi y}{b} \right| + A_s \left| \sin \frac{\pi x}{A} \sin \frac{\pi y}{b} \right| \quad (2.4)$$

where a is the stiffener spacing, A the total panel size, b the stiffener length and ζ the resulting deformation. The maximum initial deformations for the stiffeners A_s are the web thickness over 200, and the initial deformations between the stiffeners A_m is the span over 200.

The material model is as described in Figure 2.2, implemented in Ansys using MKIN, which features kinematic hardening. The elements are SHELL281 elements, which are second order shell elements with full non-linear analysis options. The sides are simply supported, and all nodes on one side are coupled in the in-plane direction. Automatic timestepping is used, with at least 20 steps to reach the maximum displacement of $\delta = 2.5 \cdot 10^3$ and a maximum of 1000 steps. To follow the complete curve displacement control is used, for the uni-axial cases one end is moved and one end is free, for the biaxial cases both ends are controlled. This does not allow for snap-through buckling, but this is not relevant since we are interested in the ultimate strength: the point just before (snap-through) buckling. Note that both sides of the panel are displacement controlled, hence there are two reaction forces due to the Poisson effect.

Ansys produced warnings regarding small pivot terms and extremely large motions. The small pivot terms are expected after buckling due to breakdown of the load-end shortening curve. The large motions arise during iterations and are clearly wrong, yet ignoring them and checking the results afterwards is seen as sufficient handling of these errors. In any case, the deformed configuration at ultimate strength is checked to be realistic, as well as the stresses and plastic strains.

Before running the model, an estimate of the allowable error is to be provided. In Paik, Kim, and Seo 2008 the difference between two (semi-)analytical methods and the finite element method is shown, for the aforementioned structure. Depending on the loading, the maximum absolute difference between FEM, ALPS/ULSAP and DNV PULS (the latter two are semi-analytical methods) are in the order of $0.1\sigma_{Yeq}$, where σ_{Yeq} is the equivalent yield stress, see also Equation 2.2. It is observed that the maximum difference is between the analytical methods, and FEM is between them.

In Paik et al. 2012 a comparison is made between FEM calculations of different institutions by different programs. For an unstiffened panel, the order of the difference is at most $0.1\sigma_{Yeq}$. For the stiffened panel the order of difference is also at most $0.1\sigma_{Yeq}$, but often at most half of it.

Results at the point of ultimate strength for a load direction of $\alpha = 45^\circ$ are presented in Figure 2.7. Figure 2.7a shows the out-of-plane deformation of the base panel. This deformation follows the initial deformation: one half wave over the span of a

Table 2.2: Tee stiffened panel dimension, in the bottom of a tanker.

Panel breadth	16,300	mm
Panel length / stiffener span	4,300	mm
Panel thickness	17.8	mm
Stiffener web height	463	mm
Stiffener thickness	8	mm
Flange width	172	mm
Flange thickness	17	mm
Stiffener spacing	815	mm

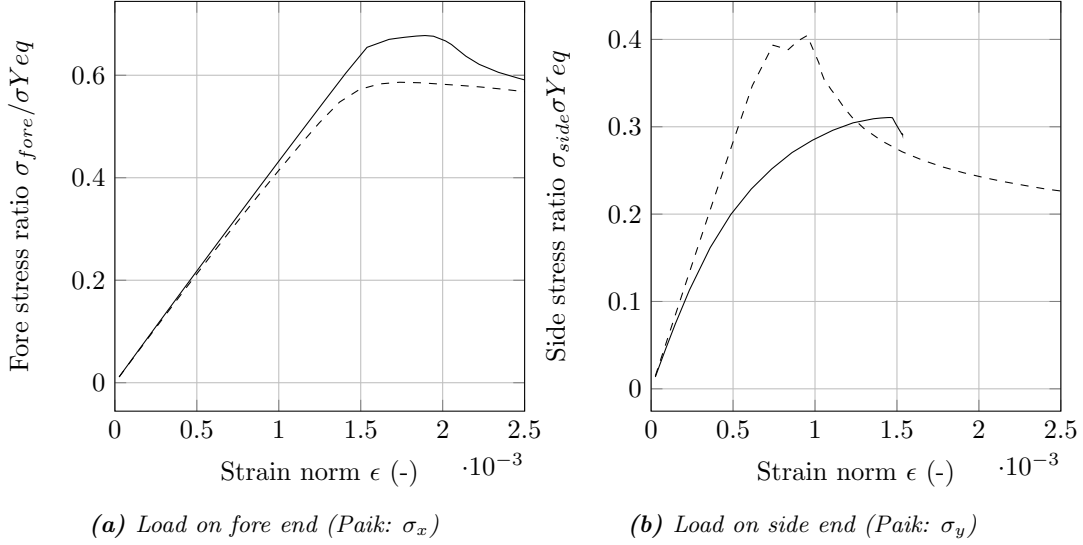


Figure 2.6: Load-end shortening curve of uniaxially loaded panels with an initial deformation of one — or five --- half-sine waves over the short end. The maximum of each curve is taken als ultimate strength, and plotted in Figure 2.8 as \blacklozenge and \blacksquare respectively.

stiffener. Figure 2.7b shows the equivalent (Von Mises) stress in the panel, which follows roughly the same pattern as the deformation. Note that the maximum stress of 460 MPa is far above the yield and ultimate stress of this stiffened panel. Figure 2.7c shows the first principle plastic strain, which are small and far from the rupture strain of $\epsilon = 0.15$. Hence the stress concentration is local, but did not induce local failure of the panel. This difference justifies using the ultimate strength of a stiffened panel as failure criterion, and will be used from here on.

The ultimate strength of the panel is determined from Figure 2.6: a load-end shortening curve. On the vertical axis the average stress divided by the yield stress of that end is taken, the horizontal axis is the end shortening divided by the panel length, hence strain. The maximum of each curve is the ultimate strength, which is discussed in Appendix A. The curves shown are for four uni-axial cases, where one end has a given displacement, the other ends are free, yet constraint to remain straight. In any case, the edges of the panel have no out-of-plane displacement.

The first maximum of the reaction forces as function of edge displacement is taken as ultimate strength. Figure 2.8 shows the US of the structure under uniaxial loading (\blacklozenge and \blacksquare , two load directions) and biaxial loading (\blackstar and \blackplus , five load directions⁴). Tests have been done using a single half wave (\blackstar and \blacklozenge) and five half waves (\blackplus and \blacksquare), where the former correspond to the uniaxial test in y direction of Paik, and the latter correspond to the uniaxial test in x direction of Paik (\bullet).

First, the results show that the uniaxial tests are not in line with the biaxial tests. It might possible to fit the Von Mises stress criterion, resulting in an ellips with centre at the origin, to the test results. At glance, the error of doing this would be lower using an initial deformation of a single half wave solution, compared to five half wave solution. Also, the reference solution seems to be matched best with the single half wave solution. Hence, the model using the single half wave is considered best and will be used for further analysis.

⁴The load directions are $\alpha = [0^\circ, 30^\circ, 45^\circ, 60^\circ, 90^\circ]$, where $\tan \alpha = \frac{\delta_{fore}}{\delta_{top}}$

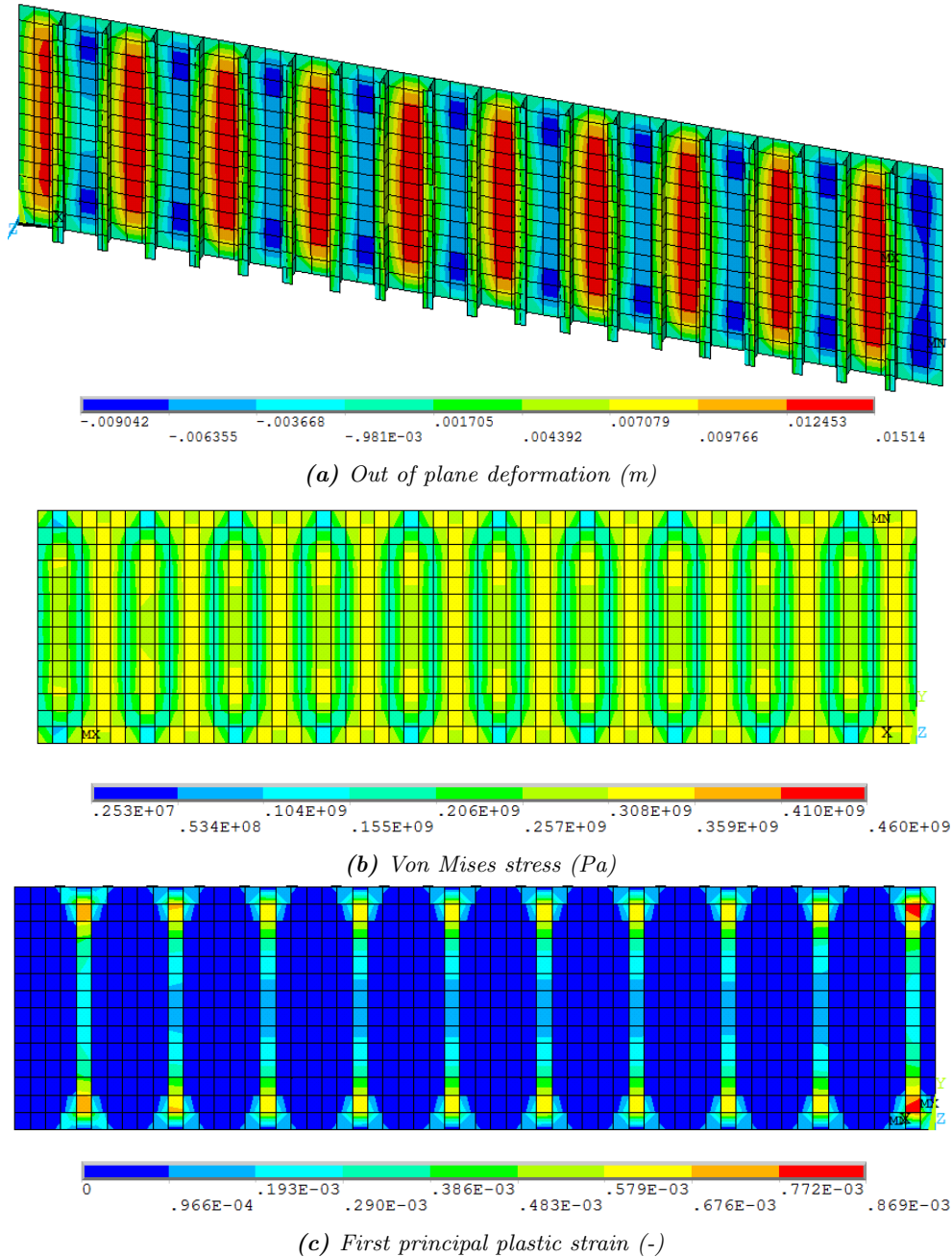


Figure 2.7: Results of quasi-static buckling analysis of the panel described in Table 2.2. Most interesting perspectives, containing maxima, are shown. Both ends of the plate have equal displacement, and the panel has an initial deformation of one half wave between each stiffener.

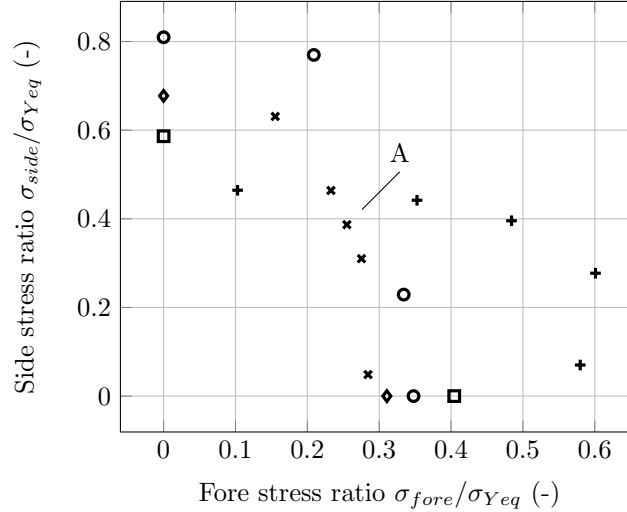


Figure 2.8: Ultimate strength calculated in five different ways: * is with one half sine wave as initial deformation, constraining both ends, ◆ has one sine wave and the unloaded end free, + is with five half sine waves as initial deformation, constraining both ends, ◻ has five half sine waves and the unloaded end free, ○ is the reference solution by Paik, Kim, and Seo 2008, using five half sine waves for the x direction, and one half sine wave for the y direction. Point A is elaborated in Figure 2.7.

The difference between the literature of Paik, Kim, and Seo 2008 and the presented solution might be attributed to a number of things. First, see also Figure 2.5, the area under consideration in the literature is shifted half a stiffener span forward, considering two half panels connected to a transverse stiffener. The transverse stiffener is then modelled by restricting the out of plane displacement of the plate and the sideways displacement of the stiffeners. The fore and aft edges have symmetry conditions (not coupled with another) and the sides are simply supported. The initial deformation are not the same. Finally, from the literature it is not clear what material model is used or how the equivalent yield stress is calculated.

2.4 Ultimate limit state with complex loadings

Loading conditions involving impact loads are complex, as stated in the introduction. Hence, it is of importance to know what parts of the loading have to be predicted in detail, and which parts are suitable for simplification. The complex impact loads are fast, in the order of 1 – 10 ms whereas the wave loading is much slower, 1 – 10 s. Sizes of load and panel are also of entirely different scale: the impact loads have peaks sized the order of 1 – 10 mm, while the panel is sized order 1 m. It is questionable whether these loads are important at all, but reality has shown that impact loading can lead to structural failure, such as described by Buchner and Bunnik 2007 for the Schiehallion FPSO. In literature no standard approach was found which could predict the relevance of different loading components. Hence, a new approach is proposed here.

2.4.1 Approach

In investigating the relevance of the load, it makes sense to look at the situation which is to be avoided at all cost: the limit state. To be more precise, the ultimate limit state is investigated, since the loads are considered to be extremely high and rare, but still occur in normal operations.

A starting point are the existing formulations of ULS, for instance the aforementioned method of Paik. However, this method is only defined for membrane stresses varying linear over the panel length and breadth, and for uniform lateral pressures. An approach which could take local pressure variations into account is the finite element method. In the previous section it was shown that FEM compares well to the literature, but has at the failure criteria of the class rules not the same in-plane load level as the ultimate strength.

Hence, it is proposed to use FEM to model the highly localized loading processes. The boundary conditions and failure criteria of the ISUM method is used, hence the US is determined for a certain lateral pressure load representing a wave impact.

From literature it is however known that realistic lateral (impact) loads will not plastically deform a stiffened panel. And even if the wave impact would deform the panel, then it is also known that localized plastic deformations will not by definition induce failure of the entire stiffened plate. The US will therefore be taken in-plane, which is also the direction in which the panel provides strength to the rest of the structure.

The usual way of determining US was explained by Figure 2.6: the maximum reaction forces of a displacement controlled calculation are taken. These calculations are without inertia or damping effects (quasi-static). The impact loads under consideration are highly dynamic, which requires another way of assessing the US. The following is proposed:

1. US and critical strain without lateral loads are determined
2. Panel is loaded quasi-static in-plane to 'just before' critical strain
3. Dynamics are turned on, out-of-plane wave impact load is applied
4. Dynamics are turned off, panel converges to new equilibrium
5. Panel sides are brought back to original location
6. Panel is loaded quasi-static in-plane to determine new US

which is illustrated in Figure 2.9. Because of this method, the new US is determined as a function of the plastic strain induced during the dynamic loading under prestrain.

Important parts of the loading are identified by decreasing the resolution of the load, which smears out the local pressures over a larger area. Then the procedure is repeated. By comparison with the US found previously, it becomes clear whether the resolution decrease is conservative or not; if the filtered peaks are significant for failure, then filtering them out introduces a significant difference in US.

This gives the hydrodynamicist a guideline how exact local effects should be modelled, while the structural engineer knows that the approach is safe. It is instrumental that the load resolution change is based on a method accessible to both the hydrodynamicist and structural engineer. Hence, it is not useful to the hydrodynamicist to talk about natural frequencies of the structure, nor is it useful to the structural engineer to use distinction of physical processes.

2.4.2 Parameters

Parameters of influence can be identified based on the literature review in this chapter. It is expected that the compressive loading on the panel makes the panel 'softer' in the out-of-plane direction and a larger out-of-plane deformation makes buckling easier.

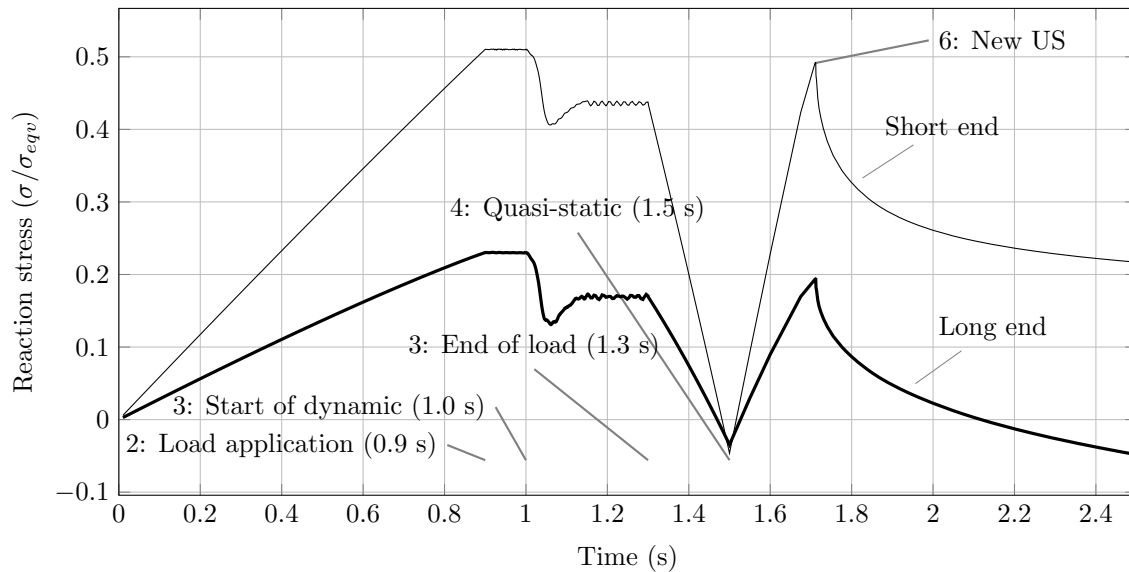


Figure 2.9: Load-time curve of ULS determination of highly dynamic impact loads, with annotated phases of determination.

- **Geometry of the panel** - Large influence, the geometry of the panel determines for a large part the failure mode under compressive loading. It is easier to get into a failure mode when the external loading presses strongly on the 'weak points' of this failure mode.
- **Material model and properties** - Medium influence, in literature only the yield strength and elastic modulus are used, after which the material softens. It is expected that change of other material (model or properties) will mostly influence the post-US behaviour.
- **In-plane prestrain** - Large influence, stresses in the stiffened panel increase with a larger compressive prestrain. A small out-of-plane deformation will then lead to a large moment of force compared to a panel with little prestrain. A large prestrain might also introduce plastic deformation of the panel, weakening the structure.
- **Out-of-plane load shape and magnitude** - Large influence, the out-of-plane load should induce earlier failure, and it is expected that when the panel is deformed by the out-of-plane load in a way which promotes buckling, that this will decrease the US.
- **Initial deformations and imperfections** - Large influence, without initial deformations and imperfections the panel will not fail during quasi-static non-linear analysis. Difference between two initial deformations was earlier shown in Figure 2.6.
- **Boundary conditions** - Small to large influence, as shown in Paik, Kim, and Seo 2008, the boundaries have an influence which falls within the aforementioned error range. However, when the boundary conditions are completely unrealistic, they will have a large effect.
- **Mesh size and structure** - Small to large influence, when the mesh has converged, the error is already small and the discretization error minimal. However, when the mesh has not converged the effect of another mesh is large.

To answer the main question of this thesis the in-plane prestrain and out-of-plane load shape and magnitude are evaluated, by using two wave impacts. The geometry of the

structure is also varied. The initial deformations and imperfections are investigated in the modelling and convergence study, but not studied with simultaneous out-of-plane loads. Boundary conditions and material are all constant.

2.4.3 Limitations

In the review of current approaches little mention was made about impact loading. This was done on purpose, as some literature on impact loading takes approaches comparable to the idealized structural unit method, Paik and Hughes 2012, whereas other publications use FEM, Cho et al. 2012. However, no mention is made of simplification of loading, nor of assessing the ultimate in-plane strength, which is required for ship strength and collapse analysis.

A few notes are placed at the developed approach. First, the approach is set up for ductile failure of the structure. Brittle failure is not taken into account, and would likely require a different test setup. Second, the method does not explicitly include or exclude one or two way coupling between load and response. In this report one way coupling is used: the load acts on the structure and not the other way around. Except for initial deformation, no imperfections such as cracks, heat affected zones or local corrosion are included. This is however possible within the defined method.

3 Finite Element Method

In order to simulate the behaviour of any structure the most versatile tool is the finite element method. Many options are available and at the start of the thesis it was chosen to develop a finite element code. The reason was twofold: in order to really get to know the assumptions, possibilities and constraints of a package, it is best to develop it. The second reason was, that a 'homebrew' code would be easy to implement and adapt, depending on the further course of the graduation. However, after thorough examination of the theories and listing the requirements of this code, it was abandoned after some time.

After that a commercial code was chosen to work with: Ansys version 16. Again a few reasons were enough to choose this package, the most important being that the author was familiar with this code and no further time should be lost in learning a new package. The second reason is, that Ansys is one of the most well-known and often used packages and is therefore trusted to be robust and accurate.

This chapter shows the fundamental knowledge gained during the process of making the FEM program. First, the governing equations of solid mechanics are laid out, consisting of kinematics, strain, stress, balance and material models. Then a few well-known kinematic assumptions are explained. An explanation of the method of weighted residuals is given third. An example of finite element derivation is given, which shows the complex beauty of FEM. Finally, a discussion on the theory is added, which motivates choices of elements and mesh.

3.1 Governing equations in solid mechanics

To predict the behaviour of a structure, relevant partial differential equations (PDE's) need to be known, following from continuum mechanics. Here a short introduction will be given how the PDE's are set up. Most theory and conventions come from Holzapfel 2000 and additional explanations were found in Bonet and Wood 1997 or McGinty 2012.

3.1.1 Kinematics and strain

The start of the continuum approach is a body \mathcal{B} , which is continuous: all individual particles are smeared out over space. This assumption is valid as long as the macroscopic behaviour of a body is considered. Body \mathcal{B} has a state or configuration which describes the body at that time: geometry, stresses, temperature, et cetera. The configuration at which the body starts is the reference configuration \mathbf{X} , and the configuration at this time (or any other time) is the current configuration \mathbf{x} . The transformation from the reference to current configuration is called motion. The motion is a bijective mapping, Sayas 2008: it uniquely maps one point of the reference

configuration to a point in the current configuration and vice-versa.

Taking the difference between the current and reference configuration gives the displacement field:

$$\mathbf{U}(\mathbf{X}, t) = \mathbf{x}(\mathbf{X}, t) - \mathbf{X} \quad (3.1)$$

$$\mathbf{u}(\mathbf{x}, t) = \mathbf{x} - \mathbf{X}(\mathbf{x}, t) \quad (3.2)$$

These two equations above are the same at glance. There is however a fundamental difference. Equation 3.1 is the displacement as function of the reference configuration \mathbf{X} , whereas Equation 3.2 looks at the displacement from the current configuration \mathbf{x} . The first is called the material or Lagrangian approach, the second the spatial or Eulerian approach. For structural mechanics it is most common to use the Lagrangian approach and for fluid mechanics the Eulerian approach is used, the reason will later be made clear.

A displacement is not yet a deformation, for instance in the case of rigid body motions or rotations. It is called deformation when the distance between two close points changes:

$$d\mathbf{x} = \mathbf{F}(\mathbf{X}, t)d\mathbf{X} \quad (3.3)$$

which defines the deformation gradient \mathbf{F} as:

$$\mathbf{F}(\mathbf{X}, t) = \frac{\partial \mathbf{x}(\mathbf{X}, t)}{\partial \mathbf{X}} = \text{Grad}\mathbf{U}(\mathbf{X}, t) \quad (3.4)$$

for the Lagrangian approach. If there is no difference between the reference and current configuration, the deformation gradient is the unit tensor. It is possible to measure the volumetric change of an infinitesimal cube in the reference configuration, when it is transformed to the current configuration.

$$dv = J(\mathbf{X}, t)dV, \quad J(\mathbf{X}, t) = \det(\mathbf{F}(\mathbf{X}, t)) > 0 \quad (3.5)$$

The deformation gradient can be used to define various strain measures, of which two will be introduced here: the Cauchy-Green strain tensor \mathbf{C} and the Green strain tensor \mathbf{E} .

$$\mathbf{C} = \mathbf{F}^T \mathbf{F} \quad (3.6)$$

$$\mathbf{E} = \frac{1}{2}(\mathbf{C} - \mathbf{I}) = \frac{1}{2} \left(\text{Grad}\mathbf{u} + \text{Grad}^T \mathbf{u} + \text{Grad}\mathbf{u}\text{Grad}^T \mathbf{u} \right) \quad (3.7)$$

Both strain measures are non-linear. It can be shown that these non-linear terms ensure that large (rigid-body) rotations do not induce strains, and have only slight effect on the strain magnitude as long as the strains are small, Bonet and Wood 1997, §IV.F. Omitting the nonlinear terms, or approximating them by a Taylor expansion, yields an error increasing with the rotation angle, Wriggers 2008, p. 8.

3.1.2 Stress and balance

On the outer surface of the body, forces can be applied and measured. These forces need to be applied in order to give the body its deformation, and are therefore linked to the deformations through stresses and tractions. Stresses and tractions in the current configuration are defined as follows:

$$\boldsymbol{\sigma} \mathbf{n} = \mathbf{t} \quad (3.8)$$

with $\boldsymbol{\sigma}$ as Cauchy stress tensor, \mathbf{n} as unit normal and \mathbf{t} as traction, all in current configuration. Traction can be seen as a force which is measured, only this force depends on the direction of the unit normal. This defines the Cauchy stress tensor, which has the axial stresses on the diagonal, and shear stresses on the off-diagonal positions. Equation 3.8 can also be used within the material.

The Cauchy stress has to satisfy two equations at all times: the linear momentum balance and the angular momentum balance. The former is satisfied by the Cauchy momentum balance:

$$\operatorname{div}\boldsymbol{\sigma} + \rho\ddot{\mathbf{u}} = \mathbf{b} \quad (3.9)$$

which is a generalization of Newton's laws, ρ denoting the density, $\ddot{\mathbf{u}}$ denoting acceleration and \mathbf{b} body forces, all in current configuration. An example of a body force is gravity. The angular momentum balance is satisfied by requiring:

$$\boldsymbol{\sigma} = \boldsymbol{\sigma}^T \quad (3.10)$$

In the initial configuration the Piola-Kirchhoff stress is used, calculated by:

$$\mathbf{P} = J\mathbf{F}^{-1}\boldsymbol{\sigma}\mathbf{F}^{-T} \quad (3.11)$$

Where the combination of left multiplication with $J\mathbf{F}^{-1}$ and right multiplication with \mathbf{F}^{-T} is called a pull back operation: doing this pulls a tensor back from the current to the initial configuration. A pull-back operation can also be performed on a strain tensor.

3.1.3 Material model

The link between deformations and stresses is made by the material (or constitutive) model. A comprehensive treatment of material models is for instance given by Willam 2002 or Holzapfel 2000, Ch. 6. Two material models are required for the intended modelling. One model for the linear elastic response and one for the non-linear plastic response.

One note should be placed before delving into material models. Countless models exist, each with their own purpose. According to Willam 2002, p. CMM-3, they can be subdivided in four scales:

- Meter level: the scale of 'practical problems in civil, mechanical and aerospace structures', which is also the scale of problems in shipbuilding.
- Millimeter level / macro-scale: the scale of laboratory experiments, at which the material properties are determined.
- Micrometer level / meso-scale: scale of the grain size and micro-defects, such as fatigue cracks. The continuum approach becomes questionable.
- Nanometer level / nano-scale: scale of single crystals where 'cause-effect relations in many cases reach beyond Newtonian mechanics'.

The first two scales have a justified continuum approach, for non-composite materials. These are also the scales most relevant to this thesis.

Linear elastic model: Saint-Venant Kirchhoff

A model for linear elasticity, often called the most simple constitutive model¹, is the Saint-Venant Kirchhoff model (Holzapfel 2000, p. 251 and Willam 2002, p. CCM-6), in elasticity tensor and strain energy density form:

$$\mathcal{C} = \Lambda \mathbf{1} \otimes \mathbf{1} + 2G\mathcal{I} \quad (3.12)$$

$$\mathcal{I}_{ijkl} = \frac{1}{2} (\delta_{ik}\delta_{jl} + \delta_{il}\delta_{jk}) \quad (3.13)$$

$$\psi(\mathbf{E}) = \frac{\gamma}{2} (\text{tr}\mathbf{E})^2 + \mu \text{tr}\mathbf{E}^2 \quad (3.14)$$

with Λ and G as Lamé constants, which define the material behaviour:

$$\Lambda = \frac{E\nu}{(1+\nu)(1-2\nu)} \quad (3.15)$$

$$G = \frac{E}{2(1+\nu)} \quad (3.16)$$

and E as elasticity modulus, ν as Poisson ratio and G representing the shear modulus also known from introductory mechanics courses. The stress is:

$$\mathbf{S} = \mathcal{C}\mathbf{E} = \frac{\partial\psi}{\partial\mathbf{E}} \quad (3.17)$$

where the middle equation is only valid for linear material models and the latter uses the strain energy density ψ . For non-linear material models the elasticity tensor depends on the state of the system:

$$\mathcal{C}(\mathbf{E}) = \frac{\partial^2\psi}{\partial\mathbf{E}^2} \quad (3.18)$$

The resulting Piola-Kirchhoff stress in the original configuration can be pushed forward to the Cauchy stress in the current configuration, by Equation 3.11.

A lot can be learned from a material model by just looking at the formulation. The Saint-Venant Kirchhoff model has two terms, the first will result in an addition of all diagonal strain components and is therefore a volume related term. Even more correctly, it represents the hydrostatic stress state, Holzapfel 2000, p. 125. The second term is symmetric and has values zero where the first term has nonzero values. That component takes care of the shear deformation, hence the use of the shear modulus.

Plasticity model

The largest difference between an elastic and a plastic material model is that the former depends only on the current configuration, whereas the latter depends on the entire deformation history. The plastic material 'remembers' when it has been stretched beyond a limit and changes its equilibrium configuration accordingly. This is called the memory effect, hysteresis or the Bauschinger effect. An comprehensive source on plasticity is the book by Lubliner 2008.

The goal of a plasticity model is to describe the yield strain ϵ^p , which relaxes the stress by:

$$\boldsymbol{\sigma} = \mathcal{C}(\boldsymbol{\epsilon} - \boldsymbol{\epsilon}^p) \quad (3.19)$$

In other words, the yield strain brings the stress back to the yield surface. A plasticity model consists of three components:

¹According to Holzapfel 2000, p.251 the Saint-Venant Kirchhoff model has problems for large compressions. These are however not expected within the scope of this thesis.

- Yield criterion
- Hardening rule
- Flow rule

The yield criterion determines when the material leaves the elastic zone. Various yield criteria exist, based on the different stress components, such as maximum shear stress (Tresca), deformation energy (Von Mises, Equation 2.1) and stress angles (Mohr-Coulomb). The hardening rule defines the material behaviour after the yield point. The flow rule describes how the material flows after yield, hence it describes to what extent the material deforms permanently. A flow rule can be derived from the yield criterion, in which case it is called an associative flow rule.

For metals the Von Mises yield criterion is often chosen. It is attractive because it is continuous and invariant to coordinate transformations, making it also a suitable choice for shell structures. The yield surface is an elliptic cone, therefore also taking care of multi-axial stress states. The hardening behaviour of metals is kinematic (direction dependent) rather than isochoric (volume dependent).

3.2 Kinematic assumptions and limitations

Combining the material model and balance laws yields the differential equation which has to be solved, also called the strong form. The strong form is formulated in three dimensions, but this might not be necessary. An axial force on a beam has a force in the largest direction of the domain. When the force is evenly applied, it is logical to assume constant strains over the cross section of the beam. This is called a kinematic assumption: the kinematics - displacement field- is assumed to be of a form. Explanations will be given for beams and plates. An example for a shell is presented.

3.2.1 Beams

A comprehensive treatment on the derivation of linear beam equations is given in Rogers 1993, here the approach and assumptions are presented. A member which has one dimension much larger than the other two is called a beam². A beam has a neutral line, stress-free under pure bending, and cross-sections. In the initial configuration, the cross-sections are perpendicular to the neutral line. It is assumed that the cross-section is rigid, and therefore the current configuration of the beam is fully determined by the orientation of the cross-sections. Instead of having a cross-section with infinite degrees of freedom (three for each dA), the orientation can be described with six degrees of freedom: three for translation of the neutral axis³, and three for the rotation around the neutral axis.

From here there are two ways to proceed. The first assumes that the rotation around the neutral axis is zero, yielding the Euler-Bernoulli beam. Hence the entire configuration of the beam is determined by the neutral axis. In practice, this means the beam has no shear deformation. The second way does not make this assumption, resulting in the Timoshenko beam, which does have shear deformation. Depending on the situation one of these models is more suitable. The Euler-Bernoulli beam is used when the beam is slender, the Timoshenko beam is used when the beam is stocky. However, for computations only the Timoshenko beam is used, for reasons made clear in Sec. 3.3. The resulting equations are still nonlinear, but this is remedied by taking the derivative with respect to the degrees of freedom at the initial configuration.

²The name beam also denotes some kinematic assumptions. A beam without bending is called a bar or truss element.

³Which is a point in the cross-section.

3.2.2 Plates

A member with one dimension much smaller than the two others is a plate⁴. For a plate the same approach is taken as for a beam, only in two dimensions. A neutral plane is set-up, which is stress-free under pure bending. Perpendicular to the neutral plane are rigid fibres, which have only displacement lateral (perpendicular to the larger dimensions) and rotation around the neutral plane.

As with the beam theory, the rotations can be either coupled to the neutral plane, or free. Coupled rotations yield a Kirchhoff-Love plate which has one degree of freedom per fibre: the lateral direction. Uncoupled rotations give a Reissner-Mindlin plate. For thin plates the former is more suitable, for thick plates the latter is used. The Reissner-Mindlin model with shear is used in computational methods, which is explained in Sec. 3.3. The linearity is again gained by deriving to the initial configuration. An extensive explanation of plate elements can for instance be found in Reddy 1991.

3.2.3 Shells

A combination of a plate and membrane element yields a shell, which has these properties:

- Two dimensions much larger than the other one
- Fibres are perpendicular to a neutral surface, which coincides with the dominant directions
- The fibres cannot be rotated around their length, but otherwise they can
- In general a shell can be curved in the initial configuration

These properties together make a shell theory one of the hardest theories in mechanics. This will be underlined by the following derivation of the shell governing equations.

The kinematic assumptions for a shell element can for instance be found in Arciniega and Reddy 2007 or Chapelle and Bathe 2003, p. 81-96⁵. The two larger directions are ξ^1 and ξ^2 , the smaller direction is ξ^3 . Note that the superscript denote the curvilinear coordinate, as defined in for instance Brannon 2004. A point \mathbf{X} on the shell neutral surface in three dimensional space is defined as:

$$\bar{\mathbf{X}} = \bar{\mathbf{X}}(\xi^1, \xi^2) \quad (3.20)$$

The great thing is, that \mathbf{X} is an arbitrary function, which allows for any shape of shell to be used. For instance, a cylinder, a dome or a corrugated plate. A local coordinate can be established, by taking the contravariant derivative of the neutral surface with respect to the natural coordinates:

$$\mathbf{g}_\alpha = \frac{\partial \mathbf{X}}{\xi^\alpha} \quad (3.21)$$

where the Greek index denotes a value of 1 or 2, as opposed to Latin indices denoting a value of 1, 2 or 3. The third basis vector is defined as:

$$\mathbf{g}_3 = \frac{\mathbf{g}_1 \times \mathbf{g}_2}{\|\mathbf{g}_1 \times \mathbf{g}_2\|} \quad (3.22)$$

⁴A plate also implies kinematic assumptions. Other variants are a membrane, which can only deform in-plane and a shell, which is a combination of a membrane and a plate.

⁵The second reference uses a different notation for the Green-Lagrange strain tensor and derives a linear shell instead of a non-linear shell. For the kinematic assumption (displacement field) this is however not of effect.

Note that the third vector is the only unit vector, and perpendicular to both other unit vectors. This is not necessarily true for the other two basis vectors. The total initial configuration including the thickness is:

$$\mathbf{U}(\xi^1, \xi^2, \xi^3) = \bar{\mathbf{X}}(\xi^1, \xi^2) + t\xi^3 \mathbf{g}_3 \quad (3.23)$$

with t as shell thickness.

The shell deformation is made up of two parts: the neutral plane part, and the out of plane part. The neutral plane has by definition no bending and is located at $\xi^3 = 0$. It is possible to state the current configuration in the same way as the initial configuration, but in my opinion it is clearer to write the current configuration as $\mathbf{x} = \mathbf{X} + \mathbf{u}$. The deformation at the neutral surface is then written as:

$$\bar{\mathbf{u}} = \bar{\mathbf{u}}(\xi^1, \xi^2) \quad (3.24)$$

of which the components can be expressed in the local coordinate system. The second deformation term describes the out of plane components:

$$\mathbf{u}^* = t\xi^3 \theta_\alpha(\xi^1, \xi^2) \mathbf{g}^\alpha(\xi^1, \xi^2) \quad (3.25)$$

The rotations θ_α are assumed to be small, to justify not taking an exact rotation tensor. Small rotations around the midplane do not imply small deformations of the shell, nor does it imply relatively straight shells. The bending deformations of the shell are governed by the curvature of Equation 3.24, in which no kinematic assumptions are made. Shear deformations on the other hand, are cases in which the fibres are not perpendicular to the neutral plane, as explained in beam and plate kinematics. The notion of small rotations for a shell is therefore a limitation to small strain deformations.

The total deformation field becomes:

$$\mathbf{u}(\xi^1, \xi^2, \xi^3) = \bar{\mathbf{u}} + \mathbf{u}^* = \bar{\mathbf{u}}(\xi^1, \xi^2) + t\xi^3 \theta_\alpha(\xi^1, \xi^2) \mathbf{g}^\alpha(\xi^1, \xi^2) \quad (3.26)$$

3.3 Methods of weighted residuals

Often it is not straightforward or even possible to obtain the solution for a PDE. In these cases the solution of the equation can be approximated. Here an approximation is made for the same PDE which was solved in the previous section. The solution will be approximated by using a method of weighted residuals, as explained in Reddy 1984.

A trial solution $\bar{u}(x, y)$ is substituted in the partial differential equation, which gives a residual $R(\bar{u})$, the value which remains after substituting the trial solution. Obviously the residual depends on the trial function and vanishes when the trial solution is the exact solution. Often \bar{u} is constructed to depend on a number of variables c_i : $\bar{u}(x) = \bar{u}(x, c_i)$, for instance by a polynomial:

$$\bar{u} = \sum_{i=1}^n c_i x^i \quad (3.27)$$

with n as order of the approximation. If the equation depends on multiple independent variables, all combinations between the addends of the polynomials in each independent variable are to be used. This can be represented by Pascals triangle⁶.

⁶This is also called Pascals Christmas tree for three independent variables.

In order to have an approximation which is as good as possible, the residual is to be minimized. This is done in an integral sense: the residual is weighed over the domain using a weighting function $v(x)$. This weighted integral should be zero.

$$\int_{\Omega} v(x)R(\bar{u}(x, c_i), x)d\Omega = 0 \quad (3.28)$$

Another (valid) interpretation of this equation is, that the residual R should be orthogonal to the weighting function v over the entire domain Ω . This is often dubbed the variational approach. There are various options for v . The end goal is to determine the constants c_i which determines the shape of the trial function. Therefore as many weight functions are required as parameters, to have as many equations as unknowns. Below a few of the numerous methods of weighted residuals, Reddy 1984, p. 44-49:

- The same functions can be used for v , that are used for u . This is called the Bubnov-Galerkin method.
- A number of points can be chosen for which the residual should vanish: $v_i = \delta(x - x_i)$, where x_i is a point in the domain. This is the collocation method.
- Minimization in general can be performed by the least squares method, using $v_i = \partial R/\partial c_i$. The boundary conditions are also included in the minimization problem.

In general, each of these methods is suitable for a category of problems. For linear problems of even order the Bubnov-Galerkin method is the easiest to use. The least-squares method yields results for even the most difficult problems, but is too complex to apply to simple linear problems.

3.4 Element formulation

The method of weighted residuals is traditionally applied on the entire domain. This is however not convenient if various geometrical details have to be applied, nor if the geometry cannot be described by continuous functions. To overcome these difficulties the domain is divided into a number of finite sized elements. Each of these elements is described by the same equations as in Paragraph 3.1.1: \mathbf{x} and \mathbf{X} . These are however determined by a few degree of freedom, which define a polynomial. Consulted works are Bathe 1996 and Hughes 2003.

For a quadrilateral element the shape in x direction is:

$$x_1 = a_0 + a_1\xi_1 + a_2\xi_2 + a_3\xi_1\xi_2 \quad (3.29)$$

where $-1 < \xi_1 < 1$ and $-1 < \xi_2 < 1$ are natural coordinates of a reference quadrilateral, illustrated in Figure 3.1. It is however more convenient to express the coefficients as function of the location of the nodes. The coefficients $a_{0...3}$ have to make sure that the locations of the nodes in the natural coordinates are mapped to the world coordinates. For this quadrilateral element the nodes are situated in the corners, yielding four equations (one for each node). Each equation has four unknowns, namely the coefficients $a_{0...3}$. This can be written as:

$$\begin{bmatrix} x_1^{(0)} \\ x_1^{(1)} \\ x_1^{(2)} \\ x_1^{(3)} \end{bmatrix} = \begin{bmatrix} 1 & -1 & -1 & 1 \\ 1 & 1 & -1 & -1 \\ 1 & 1 & 1 & 1 \\ 1 & -1 & 1 & -1 \end{bmatrix} \begin{bmatrix} a_0 \\ a_1 \\ a_2 \\ a_3 \end{bmatrix} \quad (3.30)$$

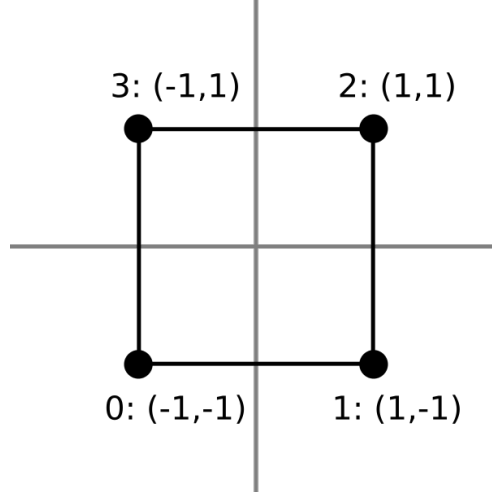


Figure 3.1: Node locations of a quadrilateral element (4 node in 2 dimensions).

where $x_1^{(n)}$ refers to the location in x_1 direction of node n , in order to avoid mixing up node index and exponents. The matrix is hereafter referred to as A and the vector as \mathbf{a} , the left hand side is \mathbf{x}_1 . To determine x_1 at an arbitrary location in the element the following equation is used:

$$x_1(\xi_1, \xi_2) = \mathbf{x}_1^T A^{-1} \begin{bmatrix} 1 \\ \xi_1 \\ \xi_2 \\ \xi_1 \xi_2 \end{bmatrix} \quad (3.31)$$

$$= \mathbf{x}_1^T \boldsymbol{\psi} \quad (3.32)$$

which only relies on the rightmost vector. Note that \mathbf{t} is the only variable, which allows easy calculation of for instance derivatives, by simply taking the required derivative of $\boldsymbol{\psi}$. The multiplication of A^{-1} with $\boldsymbol{\psi}$ is also called the approximation function $\boldsymbol{\psi}$.

The next step is to take a differential equation which has to be solved. Before going into the complicated shell theory, a linear solid element is set up. The concepts will be clear after that, which allows for a short evaluation of more complicated models.

3.4.1 Linear solid element

The relations from Section 3.1 are used. The configuration of the solid is expressed as polynomial function of arbitrary degree. The degree of the polynomial defines how many nodes should be placed: a polynome of degree n requires $n + 1$ nodes in the direction in which it acts, as the degree is not required to be equal for all directions. It is convenient to define a reference element in natural coordinates: $-1 \leq \xi_{1..3} \leq 1$. The polynome is then found by the dyadic product of the polynomes in the individual directions, same for the nodes. Each node has three degrees of freedom, hence we obtain:

$$X_i(\boldsymbol{\xi}) = X_i^{(n)} \psi_n(\boldsymbol{\xi}) \quad (3.33)$$

where X_i denotes the i th component of a 3-vector (a position), $\boldsymbol{\xi}$ is the natural coordinate in the reference element, $X_i^{(n)}$ is the i th component of the location of node n and ψ_n is the shape function corresponding to $\psi(\boldsymbol{\xi}^{(n)}) = 1$ ⁷. These same shape functions are used for the displacement $\mathbf{u}(\boldsymbol{\xi})$.

⁷Assuming Lagrangian interpolation functions.

At the end of this paragraph the deformations of the solid have to be known. Therefore a balance law is required, as well as a constitutive (material) model. Here the Cauchy momentum balance is used (Equation 3.9) with the linear elastic material model. The material model can be simplified by using the Voigt notation:

$$\boldsymbol{\sigma} \equiv \mathbf{D}\boldsymbol{\epsilon} \quad (3.34)$$

$$\boldsymbol{\epsilon} = \begin{bmatrix} u_{1,1} \\ u_{2,2} \\ u_{3,3} \\ u_{3,2} + u_{2,3} \\ u_{1,3} + u_{3,1} \\ u_{1,2} + u_{2,1} \end{bmatrix} \quad (3.35)$$

where stress and strain are represented by a vector, and a matrix \mathbf{D} represents the (linear) material properties. Note that the shear deformations are twice the off-diagonal terms of the strain tensor, this is due to different definitions of strain. The shear deformation in the vector are also called engineering shear.

This material model is substituted in the balance law, which is now only a function of deformation, acceleration and force:

$$\operatorname{div}(\boldsymbol{\sigma}) + \rho\ddot{\mathbf{u}} - \mathbf{b} = 0 \quad (3.36)$$

Now the method of weighted residuals is applied, by substituting an approximation function for \mathbf{u} , and taking the inner product of the vector equation with a test function $\boldsymbol{\eta}^T(\boldsymbol{\xi})$. Note that no explicit substitution of the approximation function is made, to keep notation clear, the same is done for the arguments of the functions.

$$\int_{\bar{\Omega}} (\boldsymbol{\eta}^T \operatorname{div}(\mathbf{D}\boldsymbol{\epsilon}) + \boldsymbol{\eta}^T \rho\ddot{\mathbf{u}} - \boldsymbol{\eta}^T \mathbf{b}) \det J d\bar{\Omega} = 0 \quad (3.37)$$

where $\bar{\Omega}$ denotes the reference element. The determinant of the Jacobian $\det J$ allows for the translation from the real domain of the element to the unit element. It is clear that the integral can be divided in three parts: an internal stress part, a dynamic part and a body force part. The internal stress part contains a derivative (divergence operator) which will require the deformation approximation function to be at least of second degree. It is convenient to weaken this requirement by applying the Gauss divergence law, yielding:

$$\int_{\bar{\Omega}} \boldsymbol{\eta}^T \operatorname{div} \boldsymbol{\sigma} \det J d\bar{\Omega} = \int_{\Gamma} \boldsymbol{\eta}^T \boldsymbol{\sigma} \mathbf{n} \det J d\bar{\Gamma} - \int_{\bar{\Omega}} \operatorname{grad} \boldsymbol{\eta}^T \boldsymbol{\sigma} \det J d\bar{\Omega} \quad (3.38)$$

where the last term can be simplified with the Voigt notation:

$$\int_{\bar{\Omega}} \operatorname{grad} \boldsymbol{\eta}^T \boldsymbol{\sigma} \det J d\bar{\Omega} = \int_{\bar{\Omega}} \boldsymbol{\gamma}^T \mathbf{D}\boldsymbol{\epsilon} \det J d\bar{\Omega} \quad (3.39)$$

where $\boldsymbol{\gamma}$ denotes the weighting function in vector form.

Before continuing with the derivation of the solid element it is informative to note that in the Bubnov-Galerkin method the test functions are taken equal to the approximation functions. Hence, Equation 3.37 is equivalent to the energy in the element minus the work performed on the element by body forces. The right hand side of Equation 3.38 defines the tractions t on the boundary of the element.

Depending on the case, one or more of these integrals have to be solved. As stated before, this is done by minimizing the weighted residual, which only depends on the accelerations, deformations and forces at the nodes. Hence, the minimization is of a

discrete equation. For now, only the integrals in Equation 3.38 are considered, the treatment for the other integrals is the same. In the end a stiffness matrix, force and displacement vector are desired. The other terms will lead also to a mass matrix and acceleration vector.

First consider the vector ϵ , this vector function contains the strains as function of location. As stated previously, the Voight notation is used for strains and only linear strains are considered. Therefore the strain vector can be written as:

$$\underbrace{\begin{bmatrix} u_{x,x} \\ u_{y,y} \\ u_{z,z} \\ \frac{u_{z,y}+u_{y,z}}{2} \\ \frac{u_{x,z}+u_{z,x}}{2} \\ \frac{u_{x,y}+u_{y,x}}{2} \end{bmatrix}}_{\epsilon(\xi)} = \begin{bmatrix} \frac{\partial}{\partial x} & 0 & 0 \\ 0 & \frac{\partial}{\partial y} & 0 \\ 0 & 0 & \frac{\partial}{\partial z} \\ 0 & \frac{\partial}{\partial z} & \frac{\partial}{\partial y} \\ \frac{\partial}{\partial z} & 0 & \frac{\partial}{\partial x} \\ \frac{\partial}{\partial y} & \frac{\partial}{\partial x} & 0 \end{bmatrix} \underbrace{\begin{bmatrix} u_x \\ u_y \\ u_z \end{bmatrix}}_{\mathbf{u}(\xi)} \quad (3.40)$$

The other unknown vector is η . It is the core of the Bubnov-Galerkin method to weigh the residual with the displacement function. Hence, $\mathbf{u}(\xi) = \eta(\xi)$. In tensor notation this would lead to a tensor $\text{grad}\eta(\xi)$ being the transpose of the strain tensor, which is symmetric by definition. Therefore, also in Voigt notation, this vector is the same as the strain vector. Note however that the strain vector as well as the gradient function both contain derivatives with respect to the global coordinates. The underlying deformation functions are however related to the natural coordinates. The transformation of the derivatives is made by the chain rule:

$$\frac{\partial u}{\partial x} = \frac{\partial u}{\partial \xi_1} \frac{\partial \xi_1}{\partial x} + \frac{\partial u}{\partial \xi_2} \frac{\partial \xi_2}{\partial x} + \frac{\partial u}{\partial \xi_3} \frac{\partial \xi_3}{\partial x} \quad (3.41)$$

which has to be done for each derivative. This translates multiplication with the inverse of the gradient of the world coordinates with respect to the natural coordinates.

All integrals are then minimized, for all kinematically admissible nodal coordinates of the weight function. Hence, the nodal coordinates of the weight function are eliminated, leaving the derivatives of the approximation functions. Hence, the integral for the stiffness matrix is often written as:

$$K = \int_{\bar{\Omega}} \mathbf{B}^T \mathbf{D} \mathbf{B} d\det J \bar{\Omega} \quad (3.42)$$

which is evaluated by numerical integration. Gauss quadrature is often used for this and explained as follows. For a number of points the integral is evaluated. The point value, which is actually the stiffness matrix at that point, is weighted and summed with the other weighted points. The mass matrix is evaluated similarly. The forces are calculated by taking the Gauss quadrature around the boundary of the element.

The element stiffness matrices are assembled by defining global node numbers and adding the local stiffness matrices to the global stiffness matrix, node by node. Hence, a system of equations is formed:

$$M\ddot{\mathbf{u}} + K\mathbf{u} = \mathbf{F} \quad (3.43)$$

where \mathbf{u} denotes the global node location vector, M the mass matrix, K the stiffness matrix and \mathbf{F} the force vector. Note that there is no explicit writing of the forces on individual nodes, or pressures on faces. These have been 'smeared out' by the weighted integration of the boundary terms.

3.4.2 Shell element

The kinematics of a shell element have shortly been discussed in Paragraph 3.2.3: a mid-surface is defined, which has fibres perpendicular to it. The fibres can rotate, which allows for shear deformation. The shell itself can also be deformed in-plane, distinguishing it from the plate element. The combination of rotations around a surface with in-plane deformation makes the mathematics behind a shell element complicated. Much literature is devoted to the derivation of these elements since many problems are encountered in their use, such as element locking (leading to excessive stiffness).

In general, there are three ways to derive a shell element stiffness matrix, Cook et al. 2002:

1. Flat elements, by combining membrane and plate bending elements. This results in simple elements, without coupling between bending and membrane stresses.
2. Degenerated solid elements, by taking a 3D solid finite element, imposing degrees of freedom which represent the degrees of freedom of a shell. It allows for use of all the continuum mechanics, material models and large deformations. See for instance Dvorkin and Bathe 1984 and Hughes 2003.
3. Curved elements based on shell theory, which are quite hard to derive. The difficulty here is that the coordinate system is connected to the mid-surface and the gradients therefore contain Christoffer symbols: derivatives of the local coordinate system with respect to the global coordinate system, for instance Arciniega and Reddy 2007.

The first way is quite obvious, it requires a plate and shell element with coinciding nodes. The second approach (degenerated solid) is explained by, for instance, Cook et al. 2002. A solid element with for instance 20 nodes is selected. A thin direction is identified, and along the thin direction the shell kinematics of the displacement field are enforced. Hence, the configuration of the 20 nodes depends on 48 degrees of freedom: 8 nodes with 6 degrees of freedom per node.

Elements based on shell theory directly introduce the shell kinematic assumptions from Section 3.2.3 into the continuum equations. Calculating the strains becomes cumbersome because of the locally varying coordinate system. This method can for instance be found in Chapelle and Bathe 2003, and will not be repeated here due to its complexity.

3.4.3 Solution strategies

When a static case is examined an iterative solver, such as a conjugate gradient method, is used to find \mathbf{u} and \mathbf{F} , since the matrix systems are often too large to invert directly. In time domain the equations are integrated using either explicit or implicit integrators. An explicit integrator satisfies the differential equations going from the current point to the next point. The implicit integrator satisfies the differential equations from the next point to the current point. The former is easy to calculate and often not stable, the latter is harder to calculate but unconditionally stable.

The results of the finite element method may result from solving the right equations, yet there may still be a modelling error. It is known that the results of FEM are highly dependent on choosing the right element distribution and element order. In most FEM packages the amount of elements can be varied, but the polynomial order of the elements is fixed, called the h -version, after the characteristic size h of the element. An alternative is increasing the polynome order in the p -version, which can be quite succesful as well as for instance described by Düster and Rank 2001 for

plasticity. To verify the element distribution a mesh convergence study is typically performed, decreasing element size and comparing the difference.

3.5 Discussion

The theory presented in this chapter gives a guidelines how to use the finite element program Ansys. Regarding the kinematics, there is not much choice but to use a Lagrangian approach, typical for solid mechanics. The kinematical assumptions will be that of a shell element. Alternatively plate elements could be chosen to investigate the effect of lateral loads, but plates cannot take in-plane deformation into account. Beam models could be used for one dimensional analysis, but fail to take bi-axial stress states into account. Solid elements would require multiple elements across the panel thickness, drastically increasing calculation time. Another advantage of shell elements is that they are able to couple axial stresses and bending, which induces moments in the initially deformed model.

The initial deformations are necessary to induce the buckling, which was also shown in Section 2.3. When no initial deformations are present, no bending stresses will be induced hence the straight panel will remain straight, until elements are too degenerated to converge. Eigenvalue buckling does not suffer from this, but is only able to predict the buckling load; not the post-buckling nor transient behaviour.

Ansys offers linear and quadratic elements, both triangular and quadrilateral. Quadratic quadrilateral elements are chosen, as they have the most nodes and therefore the best mesh convergence properties. Also, stresses and strains, which depend on the second derivative of the displacement, are not approximated as constant but as linear curve and are therefore C^0 continuous, whereas otherwise they would be discontinuous. The quadratic elements allow the modelling of phenomena such as tripping of the stiffeners to be modelled with two elements over stiffener height, whereas usually at least four elements are to be used.

Ansys uses a Newton-Raphson solver to find a solution. This solver is known to find fast solutions for quadratic optimization problems and is often used for FEM. Time integration is performed using Newmarks method, which is an implicit method, tuned with parameters to be unconditionally stable. Clearly this has an advantage over explicit solvers, but the calculation time is much longer. This is not feasible for the dynamic calculations in Chapter 5, but to use another solver, another FEM package would have to be used. Time constraints forbade this.

4 Model Development

In this chapter the finite element model for a stiffened panel is set up. Parts of the modelling choices have been given in Section 2.3 and Section 3.5. Based on this the stiffened panel is modelled and investigated. The goal of investigation is based on the sensitivity parameters in Section 2.4:

- **Geometry of the panel** - The geometry of the panel is changed by the plate thickness, which represents corrosion damage of the structure. This parameter is assumed to have a large influence, as the cubes of thickness of the flange and plate are taken to determine the moment of area of the cross-section, which is directly linked to buckling load.
- **Mesh size and structure** - Three element sizes of a structured mesh are investigated and convergence is shown. At first using eigenvalue analysis and then by quasi-static analysis of the deformed panel.
- **Initial deformations and imperfections** - The amplitude of initial deformations is varied, which represents the initially deformed structure out of a welding shop.

The effect of these parameters are studied using eigenvalue analysis. Mesh convergence is studied using eigenvalue analysis and quasi-static calculations. The second goal of this chapter is to define a baseline for strength of the stiffened panel, to be used in further analysis.

The preparations for the approach of Section 2.4 will be given here. A stiffened panel is modeled, using similar boundary conditions to the panels assessed by in the Ultimate Limit State Chapter 2, which is explained in Section 4.1. Then, elements and a mesh are chosen through a convergence study using eigenvalue buckling and quasi-static non-linear analysis. A geometric sensitivity analysis is performed last, by checking the effect of various imperfections and corrosion thicknesses. Last, the biaxial strength of the stiffened panel is investigated by looking at the complete ellips of loading conditions.

4.1 Panel geometry

A stiffened panel in the side shell an FPSO is considered, with dimensions as in Table 4.1. It is a tee-stiffened panel, enclosed by floors and stringers. The smaller dimension of the panel is in longitudinal direction, which is the same direction as the seven stiffeners stiffeners. The waterline in cyclone condition is put at 3.0 m from the bottom of the panel. Note that the values between parentheses are the minimum thicknesses after corrosion. The resulting model is shown in Figure 4.1, including initial deformations as explained in Section 4.4. The boundaries of the model have been named to place the stiffened panel in the ship's context.

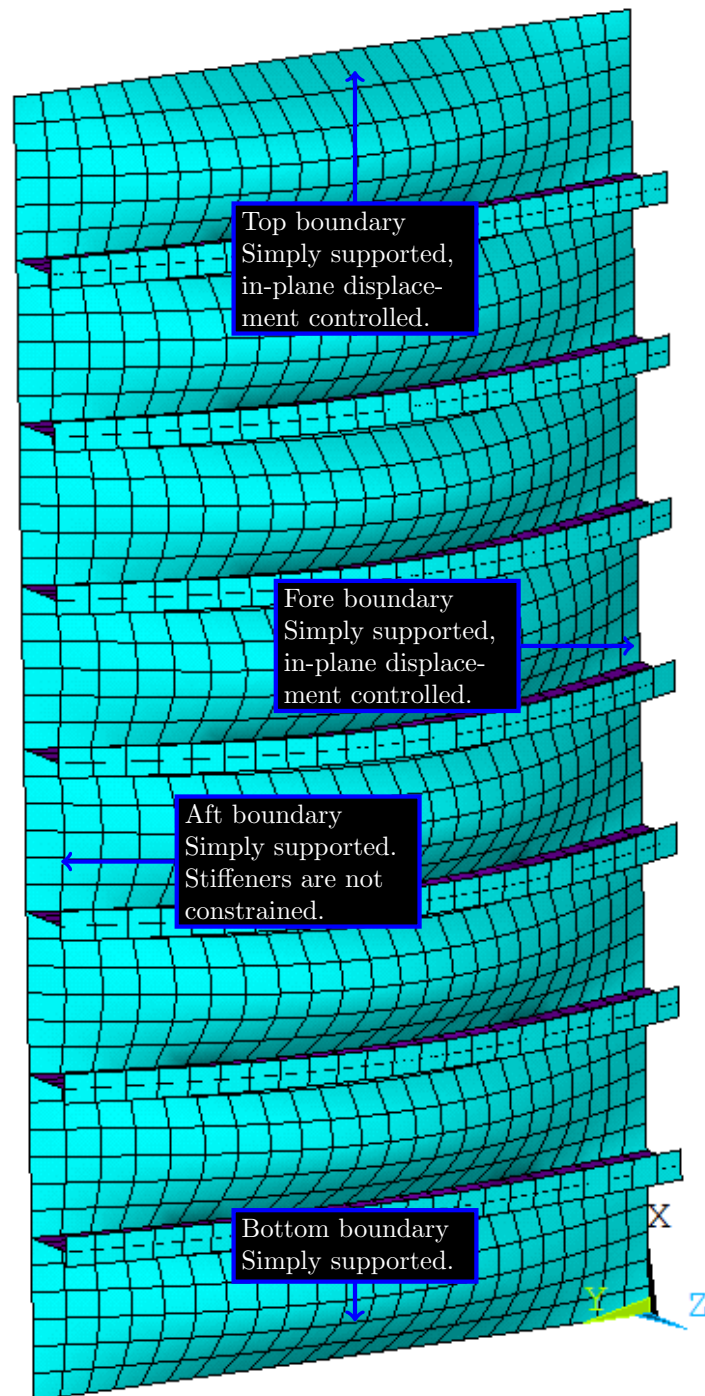


Figure 4.1: Geometry of an FPSO side structure, meshed with uniform element size of the width of the flange, with exaggerated ($\times 100$) initial deformation.

Table 4.1: Tee stiffened panel dimension, representative for side structure at the waterline of an FPSO. Values between parentheses denote minimum allowable thickness after corrosion.

Panel height	7640	mm
Panel length / stiffener span	4000	mm
Plate thickness	39 (24)	mm
Stiffener web height	400	mm
Stiffener thickness	20 (12.5)	mm
Flange width	175	mm
Flange thickness	25 (20)	mm
Stiffener spacing	955	mm
Waterline at cyclone	3000	mm

4.2 Boundary conditions

A thorough investigation of the assessment ultimate limit state of stiffened panels is also made in Paik et al. 2012, where various methods are compared. A bottom panel of a container vessel is investigated. The panel is simply supported¹ along all edges, and the edges are enforced to stay straight. Then, a comparison is made for these boundary conditions with a (1/2, 1, 1/2) bay model, where the girders are modelled by restricting the out of plane displacement. After the girder half a panel is modelled with symmetry boundary conditions. The models are in good agreement. The boundary conditions seem strange, since the girders also restrict the rotation of the plate welded to it.

In Paik, Kim, and Seo 2008 the difference between clamped and simply supported longitudinal edges is examined, for a number of in-plane load situations, both with and without external pressure. For a load on the transverse edge the difference is negligible; for bi-axial and longitudinal edge loads the US difference increases with pressure increase. Other investigations are performed by Xu et al. 2013, on periodic and symmetric boundary conditions with the transverse floor or girder in the centre of the panel. The difference between boundary conditions was very small, a larger effect coming from different initial deformations.

Based on these references the following boundary conditions are chosen. Each side of the panel is simply supported, as shown in Figure 4.1. The knees and brackets are not modelled, it is expected that the real boundary conditions will be stiffer than this and thus result in a lower critical load. Hence, the structure will fail less easy in real life than in the simulation.

These boundary conditions exclude the effects of girders and stringers, while this might be considerable. An alternative would be to have the stiffeners restricted in some direction, however the attached plate free in that direction and the choice for this is quite arbitrary.

4.3 Elements and mesh

In the end the mesh is to be used for quasi-static buckling and non-linear transient analysis. The convergence is checked through the eigenvalues of the panel, for buckling and vibrations. Eigenvalue buckling also captures higher order buckling modes, whereas quasi-static buckling only gives one buckling mode and load. The eigenval-

¹Simply supported for a shell means the displacements are fixed, as well as the in-plane rotations.

ues for vibrations are straightforward to determine and the eigenvalues for buckling depend on prestress in the panel. A force is put on the free edges of the plate, corresponding to load direction of $\alpha = [0^\circ, 30^\circ, 45^\circ, 60^\circ, 90^\circ]$, where α is defined as:

$$\tan \alpha = \frac{\delta_{top}}{\delta_{fore}} \quad (4.1)$$

where δ defined as dimensionless edge displacement, in Appendix A. Note that there are no free edges, each edge is displacement controlled or kept in position.

With this force prestress is calculated, allowing the calculation of eigenvalue buckling load. The first eigenvalues (frequencies, buckling load multipliers) are examined. The ultimate strength is used as failure criterion, hence when ultimate strength is converged, the mesh is considered to be refined enough.

As a starting point, the SHELL281 of Ansys was chosen, described in ANSYS, Inc. 2013, p. 654-656. This is a shell with a quadratic shape function and geometrical non-linear capabilities, further discussed in Section 3.5. The material model is the same as in Section 2.3.

A structured mesh is automatically generated over the entire structure, with a constant mesh size. The initial element size is as large as the width of the flange. Figure 4.1 shows the mesh². The meshing algorithm uses two elements to model the flange, three over the height of the web and six elements between each stiffener.

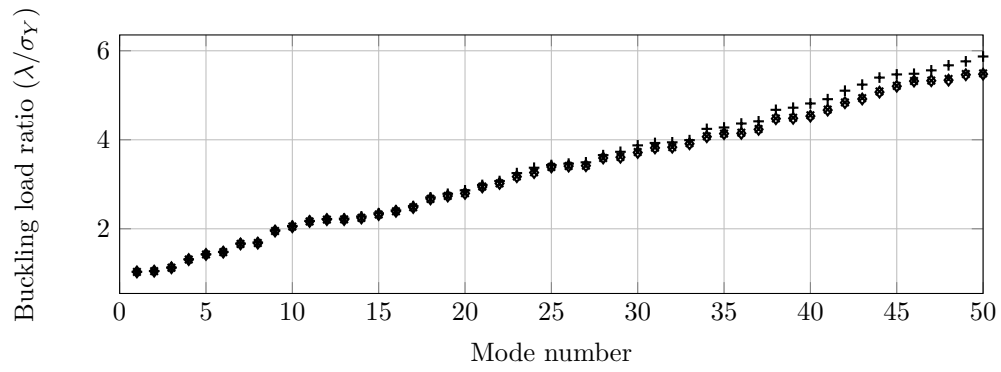
The following observations are made from Figure 4.2:

1. The panel is much stronger in the fore direction, which is expected since the Euler buckling load of a beam is inverse proportional to the length squared.
2. The buckling load ratio is higher than one, indicating that elastic buckling occurs after the material yields.
3. The mesh sensitivity of the buckling eigenvalues is higher for loading in the fore direction than for the top direction.
4. All buckling eigenvalues of the middle mesh are between the coarse and fine mesh.
5. Figures for other loading directions (not shown) have similar convergence properties.
6. Relatively, the errors are negligible for the low eigenvalues and errors of up to σ_Y for the highest eigenvalues and the coarse mesh, errors of $0.1\sigma_Y$ for the middle mesh.

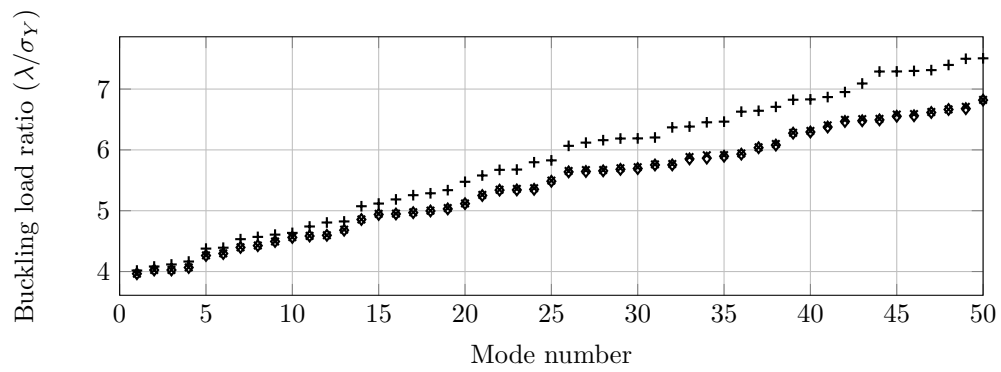
These observations can be explained by looking at the buckling modes. The first buckling modes are one half wave over the span of a stiffener, and one half wave between each stiffener. The amount of elements of the coarse mesh is already able to describe the buckling mode quite well. Higher buckling modes have more half waves, hence more elements are required to model them well. This explains why the difference in buckling load increases for higher modes.

The explanation is similar for vibration eigenvalues, however the first vibration mode is global over the entire panel. Hence, even more elements are used to describe the vibration, which gives an even better approximation of the vibration mode even for

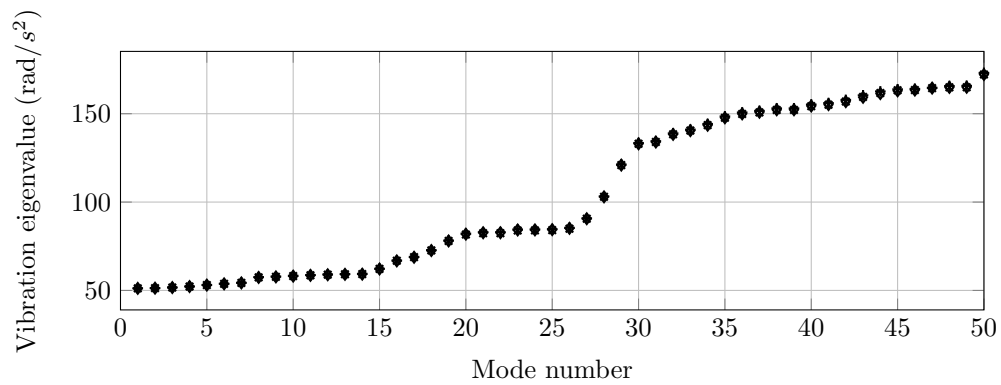
²From now on the structure will be displayed sideways and from the inside of the vessel, which gives figures which show clearly the stiffeners and deformation of the panel. It also allows more three figures to be plotted on one page and still be readable.



(a) Buckling at 0° (top direction)



(b) Buckling at 90° (fore direction)



(c) Vibration

Figure 4.2: Convergence of buckling and vibration eigenvalues, two load directions and for vibrations. Markers +, × and • denote absolute values of coarsest, middle and finest mesh respectively.

the higher modes.

The errors of the coarse and middle mesh are small enough for further calculations, in the sense of Section 2.3. The calculation time scales approximately quadratic with the time: the finest mesh has a much longer calculation time than the middle mesh. On the other hand, a finer mesh is able to represent a more detailed load. The middle mesh is chosen for further calculations to have relatively short calculation times, while a high resolution load can be applied.

4.4 Geometric imperfections

In this section the geometry is varied, to represent a realistic structure. First the thicknesses of the plates are chosen to be equal to the corroded thickness. After that, an initial deformation is applied to the panel, representing a deformation pattern, typical for initial deformations of floating offshore structures. The amplitude of the deformation between the stiffeners A_m and deformation of the stiffeners was determined using the DNV offshore standard DNV-OS-C401 Table 2-1 and rounded down to 0.5 mm. Table 4.2 shows the different test setups. The initial deformations shown are the maximum in the center of the interstiffener plate and stiffener respectively. The deformations over the rest of the panel are sinusoidal shaped, as shown in Figure 4.1 and from Equation 2.4.

4.4.1 Eigenvalue analysis

The same prestress directions have been chosen as in the convergence study. The mesh size is the middle mesh, which has an element size as large as the flange width. Figure 4.3 shows the results of eigenvalue analysis, with the buckling load factor normalized with the yield stress of the material. The following observations are made:

1. The effect of reduced thickness is much larger than that of the initial deformations, as all the points with same initial deformation are overlapping. The reduced thickness has between minimum and maximum a factor 4 in strength and the initial deformation a factor 1.7 between minimum and maximum.
2. Initial deformation strengthens the panel in eigenvalue analysis contrary to the expectation of weakening it by inducing strains in the shape of the buckling mode.

Checking the eigenmodes shows that the first eigenmodes are comparable to Equation 2.4, but without the absolute marks. Hence, the first eigenmodes are orthogonal to the initial deformation. The reason to still apply initial deformations lies in the quasi-static and dynamic analysis, where initial deformations are required to 'trigger'

Table 4.2: Test matrix for different geometries, all in mm.

Setup	t_p	t_w	t_f	A_m	A_s	Legend
1	39	20	25	0	0	+
2	31	16	22	0	0	×
3	24	12.5	20	0	0	*
4	39	20	25	2	3	□
5	31	16	22	2	3	◇
6	24	12.5	20	2	3	○
7	39	20	25	4.5	6	■
8	31	16	22	4.5	6	◆
9	24	12.5	20	4.5	6	*

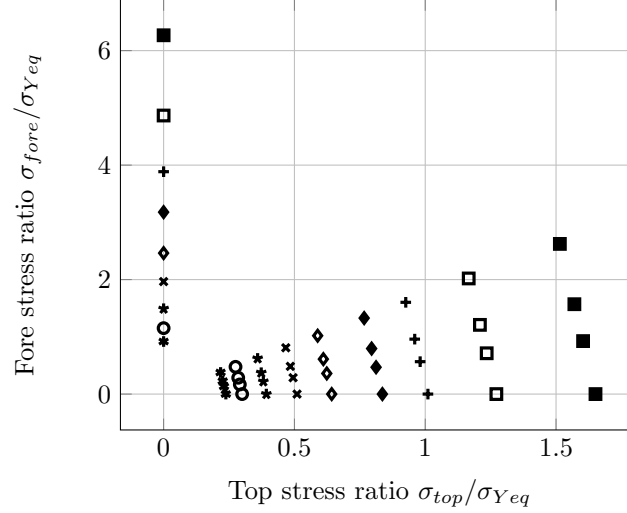


Figure 4.3: First eigenvalue buckling modes, legend explained in Table 4.2. The buckling eigenvalues are divided by the yield equivalent stress of that side, and set to the angle of the load direction.

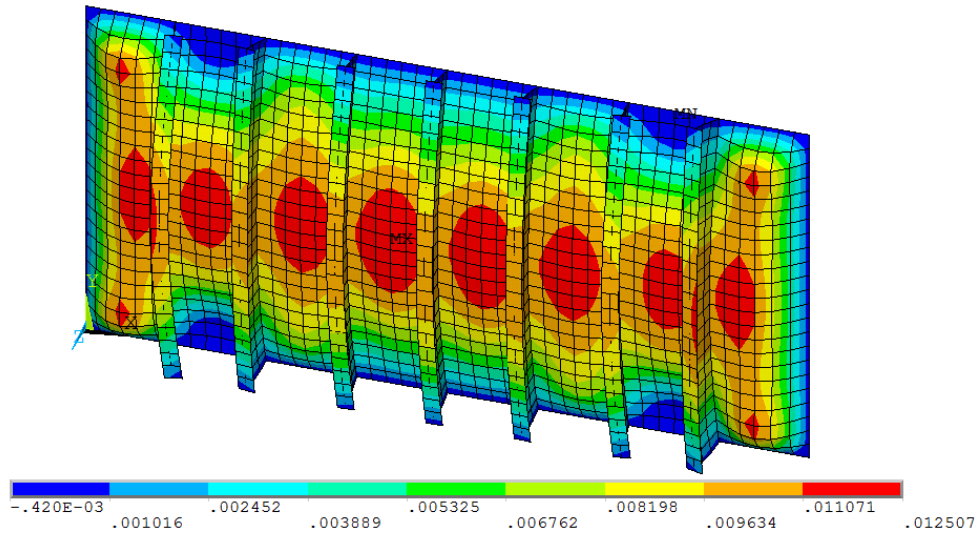
the various buckling modes. The effect of different shapes of initial deformations are already mentioned in Section 2.3, for a different panel.

4.4.2 Quasi-static analysis

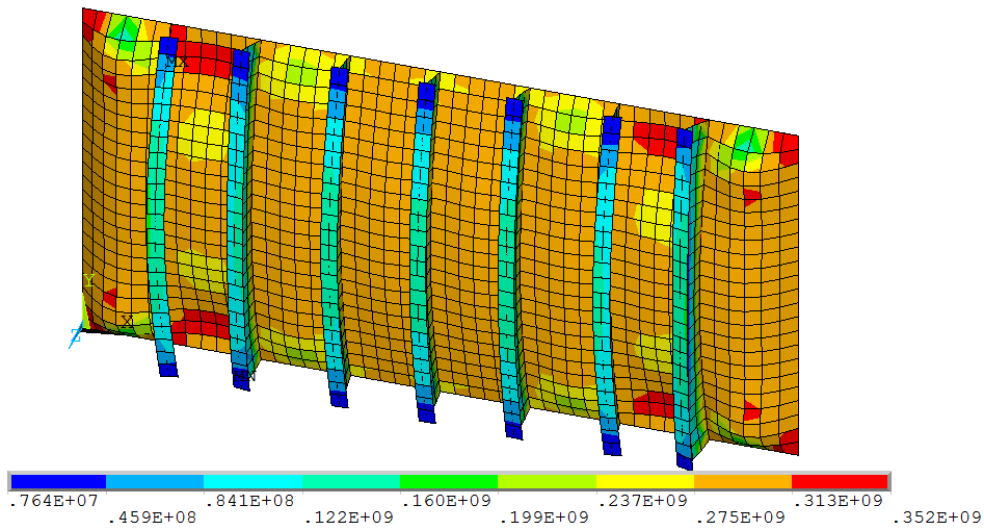
For the calculations later on, quasi-static and transient behaviour will be examined. The buckling modes and load factors obtained from eigenvalue buckling analysis do show a good convergence of the mesh and higher order modes. To be sure the mesh is chosen at the right size, the quasi-static buckling load is also examined. All sides are simply supported. The fore and top boundary of Figure 4.1 are displacement controlled, giving displacement angles of $\alpha = [0^\circ, 30^\circ, 45^\circ, 60^\circ, 90^\circ]$, defined by Equation 4.1.

A selection of the results is plotted in Figure 4.4, containing the out of plane deformation, Von Mises stress and first principal plastic strain. These plots correspond to the moment where the ultimate load carrying capacity is reached, where the panel is displaced in direction of the stiffeners. At this point the displacement is 6.2 mm and the total load on the panel 60 MN, distributed over the side of the panel. The following observations are made:

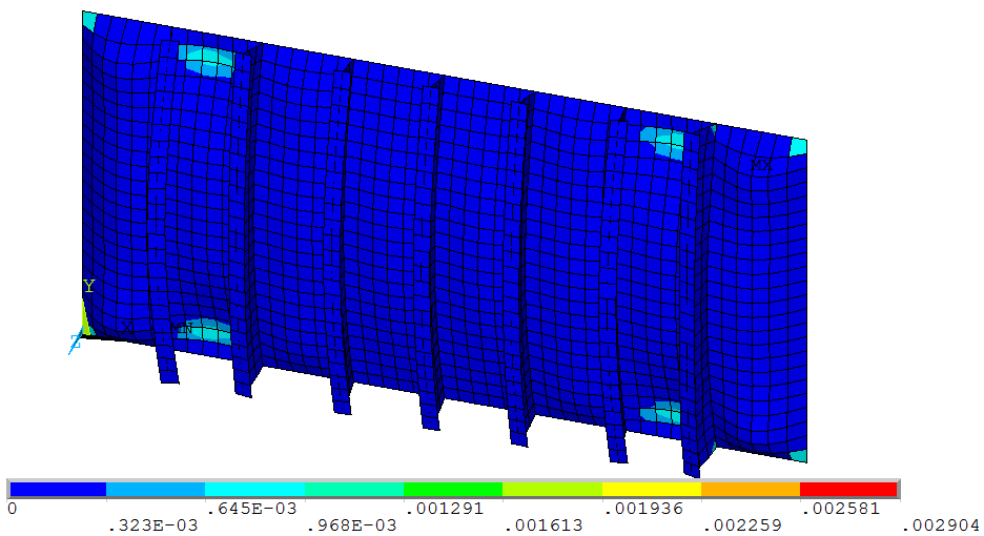
1. The out of plane deformations are of order of 0.01 m and clearly localized between the stiffeners.
2. The buckling is symmetric over both the height and width of the panel, which is reasonable considering the symmetric geometry and applied boundary conditions. Note also that the panel buckles with one half sine wave along the middle four panels, has three peaks along the sides and has three peaks (opposing directions) at the second and second to last panel.
3. The principal plastic strains are also the highest at the boundary between the inward out of plane peak and the two outward out of plane peaks at these panels. The stresses at the plotted side are not too high, yet the other side experiences higher compressive stresses, due to the bending compressive stresses and the total compression of the panel. Note here that for the shown panel the stresses far exceed the allowable stresses and the plastic strains are far below the



(a) Out of plane deformation (m)

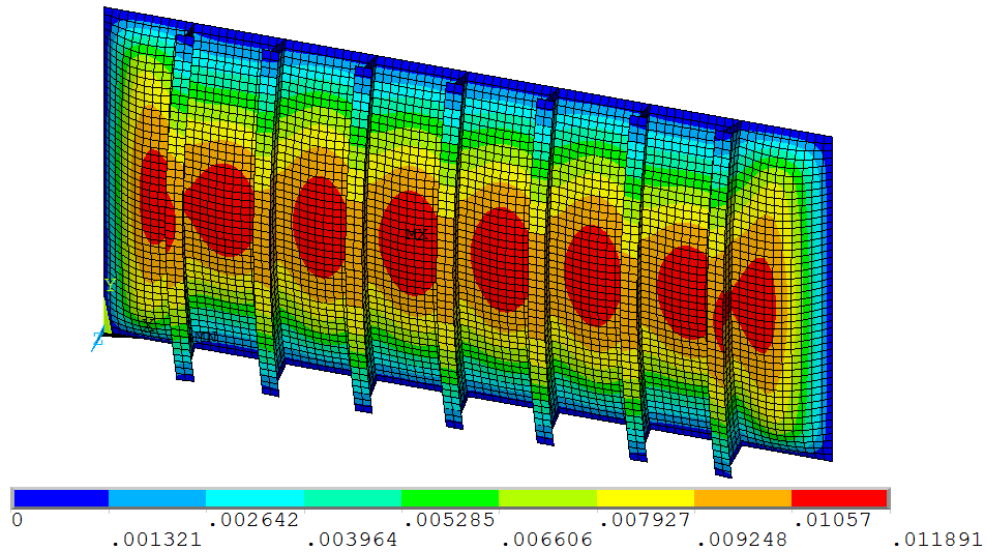


(b) Von Mises stress (Pa)

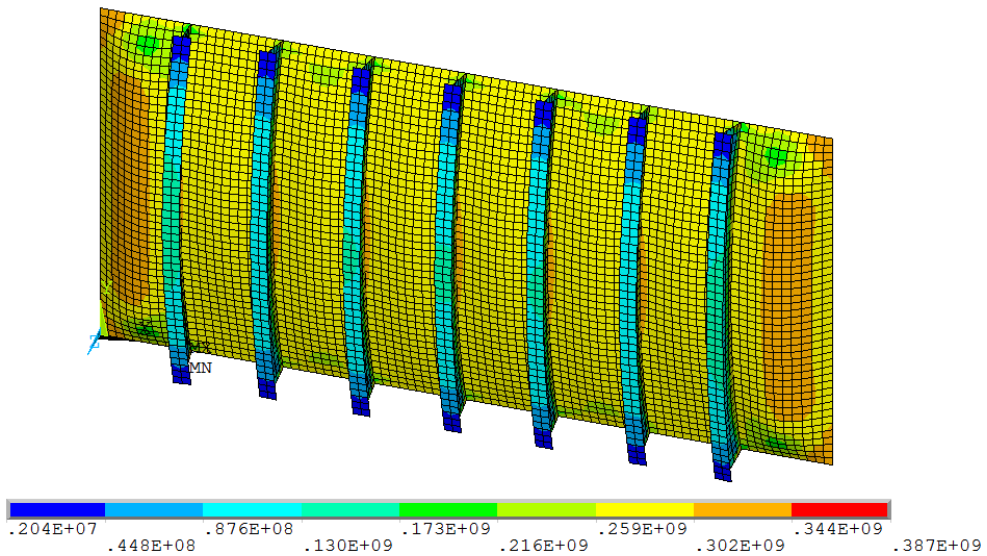


(c) First principal plastic strain (-)

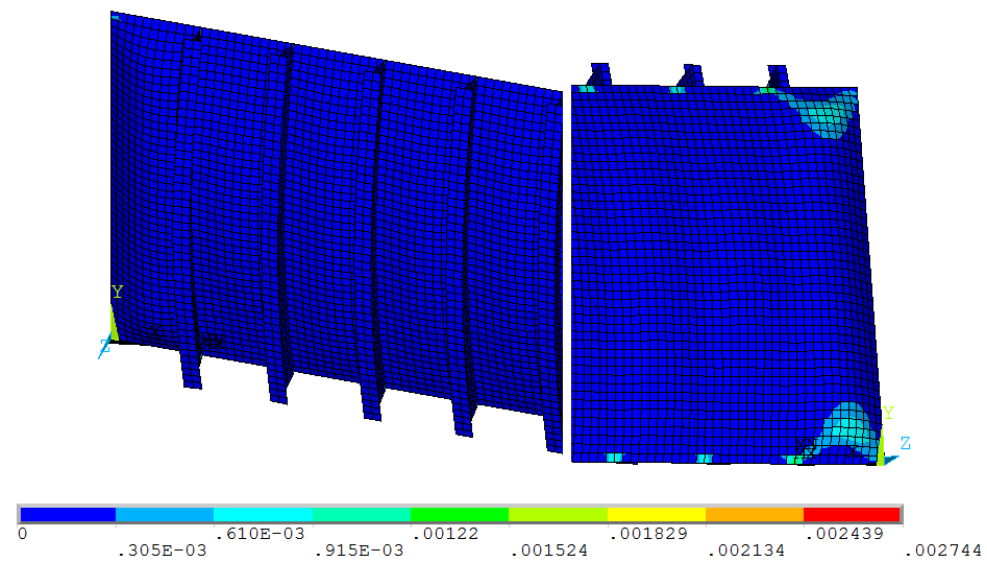
Figure 4.4: Results of quasi-static buckling analysis, using the most deformed and corroded plate. These figures were generated with an element size equal to the flange thickness, loaded in ship longitudinal direction (on the long end). Image is rotated clockwise for better display.



(a) Out of plane deformation (m)



(b) Von Mises stress (Pa)



(c) First principal plastic strain (-), the insert shows the other side of the panel.

Figure 4.5: Results of quasi-static buckling analysis, using the most deformed and corroded plate. These figures were generated with an element size half of the flange thickness, loaded in ship longitudinal direction (on the long end).

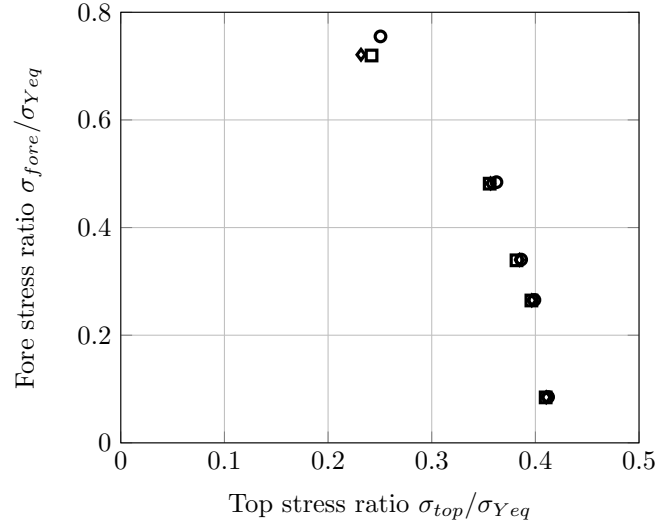


Figure 4.6: Convergence of quasi static buckling, using geometric non-linearities and a non-linear material model. Markers \square , \diamond and \circ denote a mesh size of half the flange width, flange width and twice the flange width respectively.

allowable plastic strains. Hence, locally the material has failed, but no rupture has occurred.

Another result is plotted in Figure 4.5, containing the same plots but for an element size half shown in Figure 4.4. These plots are also made at the ultimate strength, at a displacement of 6.2 mm and a total load of 60 MN: the same result. Other observations are:

1. Comparison of the first two plots, out of plane displacement and Von Mises stress, gives quite similar results. The finer mesh seems to result in a higher, yet smoother stress distribution. The real difference is found in the plastic strain, which is non-existent on the inside of the panel.
2. On the outside of the panel the plastic deformation is visible at the outmost stiffened panel, whereas the plastic deformation of the other mesh seems to occur at the panel next to it. Hence, the plastic deformation is not predicted well enough using the middle mesh.

It is however also seen, that a criterion on strain is not sufficient for failure of the panel. Hence, the ultimate strength of each mesh is compared. Checking the maximum elastic strain criteria separately gave failure of the stiffened panel at half of the ultimate strength value, but with much larger strain.

The ultimate strength is plotted in Figure 4.6, obtained as explained in the methodology. Based on the shown results, the following observations are made:

1. The coarsest mesh has in general the highest US, the finest mesh the lowest US. This is predicted by the eigenvalue analysis and confirmed by the quasi-static analysis. The differences are however lower than eigenvalue analysis predicts.
2. Uniaxial compression with the 'free' edges fixed in position give a compressive reaction force due to the Poisson effect. In the figure this is visible by having no test with zero reaction force in one of the directions.
3. Examination of the load-end shortening curves showed that for all loading directions, except only fore direction, the maximum in top stress is reached before the maximum in fore stress.

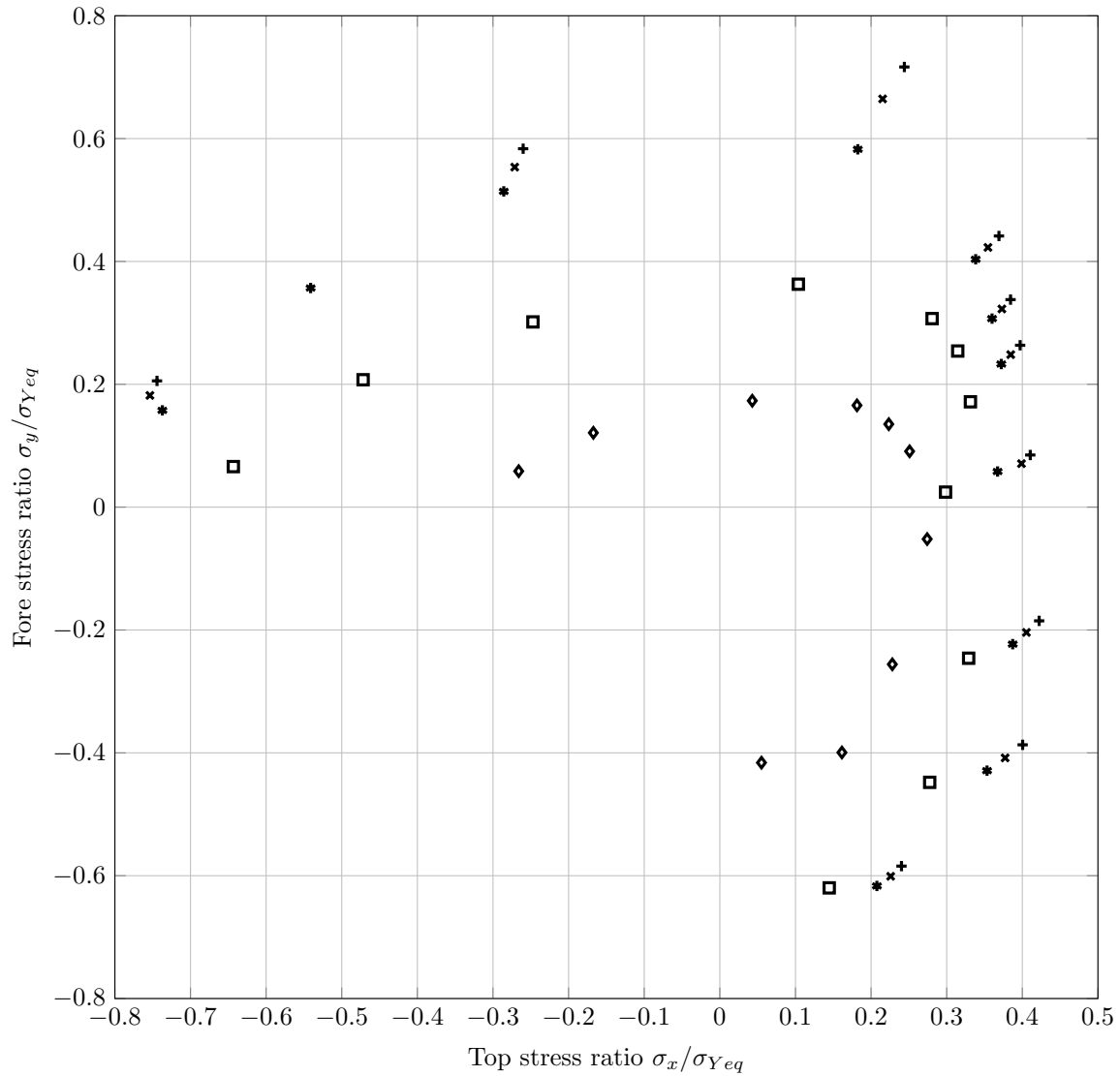


Figure 4.7: Full ellips of US for lateral pressure of $p = [0, 1, 2, 5, 10] \cdot 10^5 \text{ Pa}$ for $+$, $*$, $*$, \square and \diamond respectively. Element size is same as flange width.

4.5 Biaxial strength

In the previous calculations the implicit assumption was, that the biaxial compressive load case is the most critical. This is not the only load case, as compressive-tensile and tensile-tensile is also possible. For the tensile-tensile cases, it is straightforward to predict that the ultimate load carrying capacity is defined by the rupture strain of the stiffened panel, as no instabilities will form. This can not be said about the compressive-tensile cases, which motivates Figure 4.7. In this figure the complete failure surface of compressive-(compressive/tensile) cases is drawn. As before, each point is determined by the maximum reaction force of a displacement controlled test. The maximum displacement ratio was $\delta = 2.5 \cdot 10^{-3}$, and if no maximum is found no point is plotted.

In Figure 4.7 the US of the panel is plotted for five uniform lateral pressures: $p = [0, 1, 2, 5, 10] \cdot 10^5 \text{ Pa}$, hence ranging from equal inside and outside pressure, to the hydrostatic pressure on a panel at a depth of 100 m. The following is observed:

1. The panel is the strongest in compression from the fore end and tension from the top end. However, the US is most sensitive to lateral pressure loaded compressive-compressive.
2. A higher lateral pressure results in a smaller failure surface.
3. The failure surface of $p = [2, 5]10^5$ Pa is not convex.
4. An increase in lateral pressure does not give a linear scaling of the failure point towards the origin, but also a shift to a relatively higher fore stress ratio.
5. The figure is the result of displacement controlled tests, for each quadrant with the same angles. The reaction forces in the compressive-compressive regime are more sensitive to the displacement angle, as they are closer.

Especially item 3 is interesting, as from the theory presented in Section 2.2 a convex failure surface is expected since it is formed by the largest possible area enclosed by all failure surfaces of each failure mode. It is also curious that the 'dent' causing the non-convexity is caused by the same points for $p = [2, 5] \cdot 10^5$ Pa but is not present for the other loadings. The difference between theory and computations can be caused by interaction of failure modes, which might cause weakening of the stiffened panel.

4.6 Discussion

A side shell of an FSPO was investigated, with different corroded thicknesses and initial deformations. The input files used are modified from Section 2.3 and are therefore taken as verified. The mesh convergence for biaxial loading was at an element size equal to the flange width. The final geometry of the panel was chosen as maximally corroded and deformed, within design and class range respectively. The mesh was also converged for this setup.

4.6.1 Evaluation of results

Regarding the criteria mentioned at the start of the chapter, the following is observed:

- **Geometry of the panel** - The corrosion has a large influence on the eigenvalue buckling of the panel. This is in line with for instance the Euler buckling equation:

$$F_c = \frac{\pi^2 EI}{(KL)^2} \quad (4.2)$$

where F_c is the critical (buckling) load, E the elastic modulus, I the moment of area of beam cross-section, K a factor denoting boundary conditions and L the length of the beam. Here, the moment of area depends cubic on thickness of the panel, which explains the large effect of thickness.

- **Initial deformations and imperfections** - In eigenvalue buckling analysis, the effect of initial deformations stiffens the panel, due to orthogonality with the first eigenmode. Yet, the initial deformations are required to trigger buckling in quasi-static analysis. Alternatively it was also tried to trigger the buckling using a (small) external pressure, but this did not deliver realistic results.

The initial deformations applied are not the same as the first eigenvalue of buckling, which usually the case, for instance by Paik, Kim, and Seo 2008. For two reasons it was not chosen to do this:

- The first eigenvalue of buckling is not the same for all loading cases. It should therefore be determined for each load case, using an applicable prestress. However, the prestress direction is not equal to the direction of the reaction forces using displacement control. Also, the buckling and dynamic eigenmodes are not the same: buckling shows a half wave over each interstiffener panel and dynamic eigenmode shows a single half wave over the entire panel.
- All eigenmodes do not look like any initial deformed configuration encountered in real life.

Hence, an unbiased yet realistic looking initial deformation is justified.

- **Mesh size and structure** - Only small differences were observed between the three mesh sizes, hence even the coarsest mesh represents the structure well enough. This can probably be attributed for a large part to the use of quadratic elements, which allow displaying elaborate displacements also for relatively coarse meshes.

In eigenvalue analysis of Figure 4.2 it was shown that the higher eigenvalues are not represented well with the coarsest mesh. The coarse mesh is not able to deform in the 'finer' deformation patterns of higher eigenmodes. This is especially true in loading from the fore direction, considering that the stiffeners are likely to deform as well as the plate, and the stiffeners have only 2 elements over their height in the coarsest mesh.

The result which counts the most is the quasi-static mesh convergence of the deformed and corroded panel in Figure 4.6. It uses the same analysis method as will be used later to assess the panel strength, hence convergence is most important. Except for the fore-aft compression, all results nearly coincide. The results in Figure 4.4 and 4.5 show that the deformation pattern is mainly between the stiffeners and has only 1 or 3 half waves. This explains why the mesh dependency is virtually absent, the quadratic elements themselves can represent one peak per element, which is not nearly required.

All the above lead to choosing the middle mesh size, with maximum corrosion and initial deformations, following Equation 2.4.

The biaxial strength is evaluated for various uniform lateral pressures with compressive-compressive and compressive-tensile in-plane stresses. Cases without compression do not give an extreme value for the stress, their failure is dominated by maximum strain (rupture). It is clear that in some cases a solution was not found within the defined calculation time or deformation.

A surprising observation is that the failure surface is not necessarily convex, which is quite contrary to what is found in literature. This would mean several failure modes interact with each other. Another unexpected observation is, that all points which have the same controlled displacement, are not on one line. Hence, the external pressure does not give a linear scaling of the failure surface, but also changes the stress-strain relation. Clearly the non-linear calculations have an effect.

4.6.2 Recommendations

In the previous sections the focus was on bi-axial loading of the panel, which is not the most likely load scenario of the chosen structure. Rather, a combination of fore-aft compression and shear should be investigated. It was however chosen to investigate fore-aft compression and top-bottom compression to have a better connection to the

cases evaluated in literature.

Other improvements might be the investigation of more initial deformations. Currently only deformations applied are local between stiffeners and global over the panel length and width. Besides varying the number of half-waves, the web and flange of the stiffener might be initially deformed as well, possibly triggering also web buckling or stiffener tripping.

5 Simplified Load Application

This chapter adds a new load with respect to Chapter 4: a lateral loading due to a wave impact. This wave impact is three to four orders of magnitude faster than the in-plane loading on the stiffened panel. To test the procedure proposed in Section 2.4, a realistic load is applied to the structure and the ultimate strength (US) evaluated. This is done for a number of prestrains, which represent the bending of the vessel. Hence, the following points are examined:

- **In-plane prestrain** - A critical strain δ_c is varied, representing the compression the panel experiences during bending. A large influence is expected, since the prestrain effectively weakens the panel.
- **Out-of-plane load shape and magnitude** - Two numerically determined loads are used with various resolutions and change of impact location. The difference in US between two load resolutions shows the importance of the details which are lost. Load magnitude is not varied.
- **Geometry of the panel** - After the main testing it was found that all failure modes of the panels were very much alike, as described in Appendix B. Therefore, also another panel is investigated, with a beam column collapse.

In this chapter the out-of-plane pressure load, caused by a wave impact, is explained first. After that the load is dynamically applied to the structure, which gives the new ultimate load carrying capacity (US) for the structure. Third is a comparison with static pressure, which is close to the analysis of Chapter 2. Finally a discussion of the results follows.

5.1 Load description and simplification

The load of a breaking wave on a rigid wall is used, as described by Guilcher et al. 2014, Figure 5.1a. The load is determined in one spatial dimension, height, and in time. In this thesis a reduced version of the loads are used, where the resolution is decreased on relatively flat portions of the load map. The breaking wave is a water wave, and the gas is air. The wave impacts at 4.7 m from the bottom of the wall, and the wave crest is at 6.4 m for the wave investigated here.

The wave before impact is modelled using a non-linear potential flow code (FSID). The breaking wave impacts are then simulated using a smoothed particle hydrodynamics code (SPH-Flow). SPH uses distinct particles, as opposed to control volumes. Density and velocity of these particles correspond to the density and velocity of the fluid, hence the flow can be determined. An advantage of SPH is that the method is meshless, which makes it easier to model free-surface flows. This is especially relevant in multi-fluid flows. More details of SPH can be found in Monaghan 1992.

Similarities between breaking waves were found by Lafeber, Brosset, and Bogaert 2012, and distinguished in three elementary loading processes (ELP):

1. Direct impact, due to the fluid motion being stopped by the wall, related to fluid compressibility.
2. Building jet, due to change of momentum, leading to a travelling pulse.
3. Compression / expansion of gas, due to the gas entrapped in the wave.

One or more ELPs are prominent depending on the wave shape before impact.

The first load under consideration is by Guilcher et al. 2014 with a large air pocket, see Figure 5.1a. The peak is caused by ELP 1 and the bulge behind it is due to ELP 3. The ridge on the bulge is due to ELP 2. Figure 5.2 shows pressure over the panel height at the time just before impact, and some time after the impact, corresponding to Figure 5.1a. The second load under investigation is a flip-through impact, which has a dominant ELP 2, shown as a travelling pulse, see Figure 5.1b.

Simplification of the load is necessary to study the effects of local details, as explained in Section 2.4. The simplification mechanism should be useful for both the hydrodynamicist and the structural engineer. Hence, natural frequencies of the structure are excluded, as are physical processes such as the ELP's. Besides that, the simplification should match the original pressure closely and have the same total weight.

It could be argued that an energy-based simplification is more useful. However, this would require basing the simplification on the deformation of the structure. The deformation changes during the simulation, hence it is thought that this is too complex (for this study). The same is thought about image processing techniques, filters and wavelets: they are promising and interesting to look at, but for now not feasible.

The following simplification procedure is proposed. Pressures corresponding to a new resolution \bar{x}_i are to be found, using:

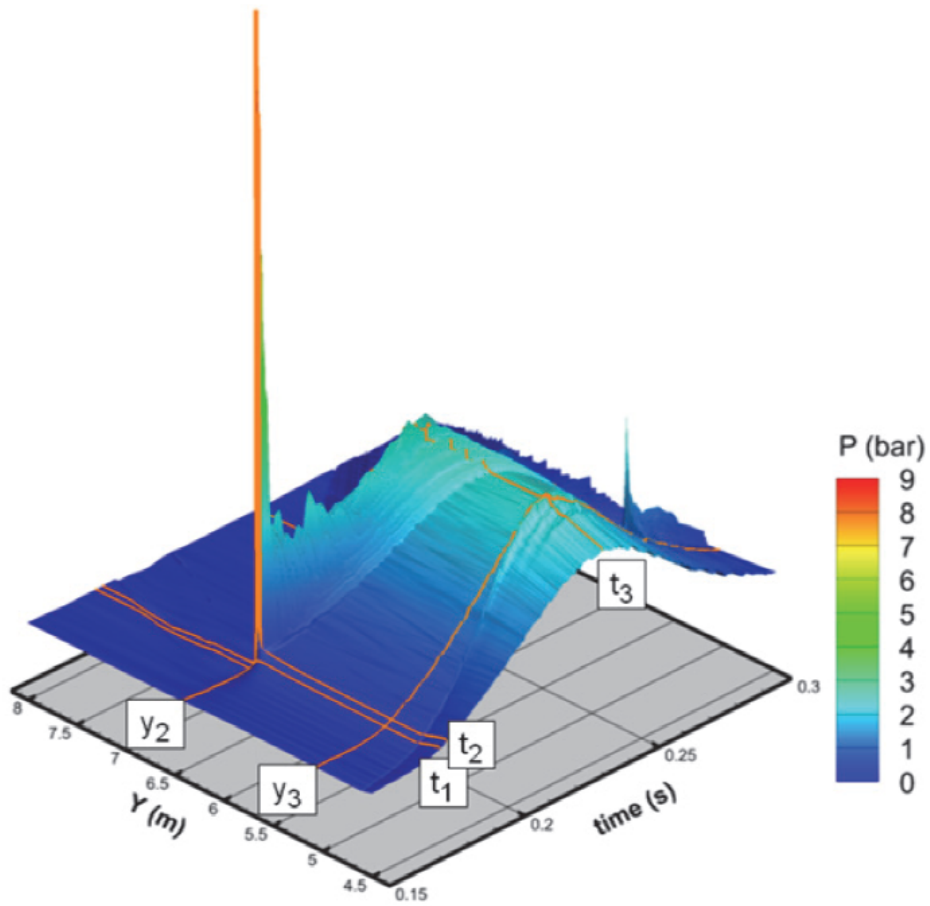
$$w_i = \frac{x - x_{i-1}}{x_i - x_{i-1}} \quad (5.1)$$

$$\bar{y}_i = \frac{\int_{\bar{x}_{i-1}}^{\bar{x}_i} y(x)w_i(x)dx + \int_{\bar{x}_i}^{\bar{x}_{i+1}} y(x)(1 - w_{i+1})(x)dx}{x_{i+1} - x_{i-1}} \quad (5.2)$$

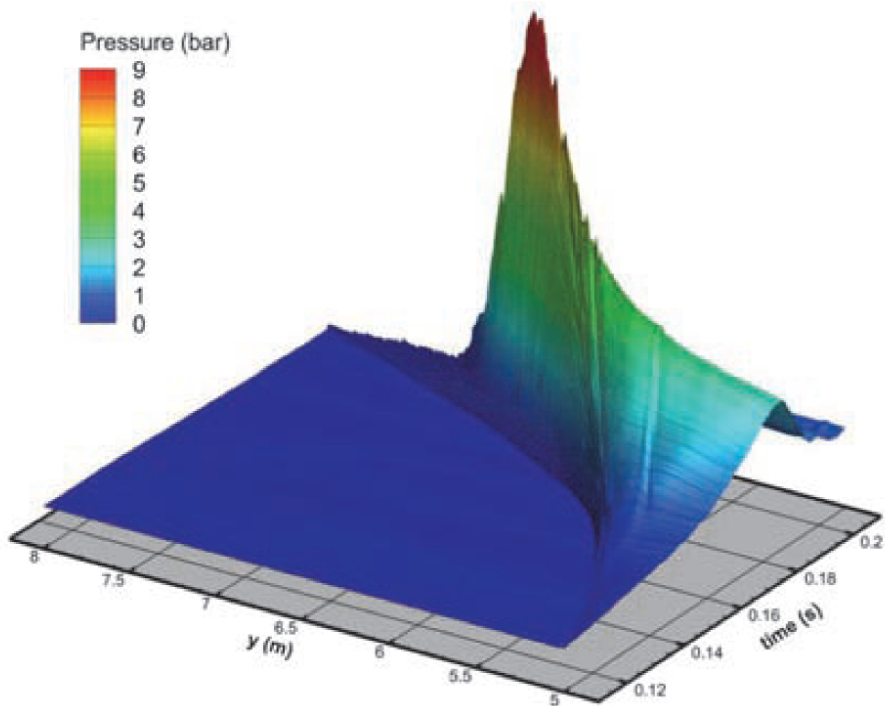
hence, the value of the original function is integrated, weighted linear in distance to \bar{x}_i , where points closer to \bar{x}_i are more important. The first and last point are integrated (trapezoid rule) in the same way, and their values doubled. After that, the weight of the new pressure map \bar{y}_i is made equal to the weight of the original pressure map. Ansys automatically interpolates linearly between the points of the pressure map, hence the pressure map is C^0 continuous.

Figure 5.3 shows the first simplified wave impact. The change of resolution is visible in the height dimension, the pressure is equal over the length of the panel. From coarse to fine, the figures gradually show more details. For instance the highest pressure in the coarsest load is at the top of the bulge, but at the finest resolution the peak is visible at $t = 1$ s, $h = 2.5$ m, which is the peak also visible in Figure 5.1a at t_1 . Note that time and space were shifted to accommodate the procedure sketched in Section 2.4 and have the bottom of the load at the bottom of the stiffened panel. The load is not stretched or slowed down and zero pressure is taken above the known load map, since the stiffened panel is taller than the load map.

A second thing can be learned from Figure 5.3. As the resolution in space changes, the time scale is changed as well. The slope of a pressure iso line denotes the speed with which a pressure propagates. When the spatial resolution is severely decreased, the pressure iso line is constant over space. The finer spatial resolutions show that the



(a) Breaking wave with ELP 1 and 3.



(b) Flip-through impact with ELP 2.

Figure 5.1: Pressure map in height and time, from Guilcher et al. 2014. Minimum height is put on the bottom of the panel.

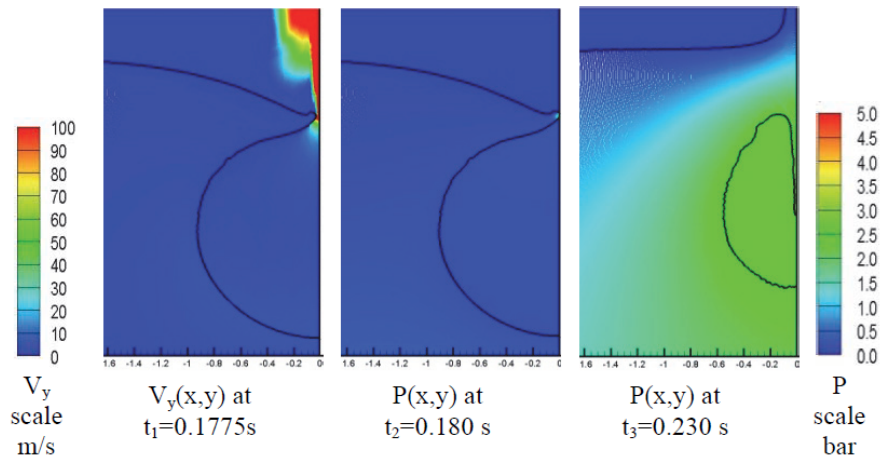


Figure 5.2: Velocity and pressure map at impact, Guilcher et al. 2014.

pressure moves with a velocity over the panel. It is therefore concluded that changing the spatial resolution has an effect on the temporal resolution, as velocities are not correctly represented.

Comparing the different load resolutions of the second wave impact in Figure 5.4, the following is observed:

1. The time at which the uniform load has a maximum is the same as the time at which the resolution $h = 0.1$ m has its maximum.
2. For resolution $h = 0.1$ m the load map shows a boundary between atmospheric pressure (dark blue area) and the wave impact. This boundary is not well represented at lower resolutions $h > 0.5$ m.
3. The wave impact takes place only on the bottom of the stiffened panel, hence it is expected that the failure mode is not symmetric over the height of the panel.
4. Remarks regarding the ability to display a pressure propagation speed can be made here as well, the coarse resolution has a faster pressure propagation (steep contour) than the fine resolution.

Now the load is applied to the same stiffened panel considered in Chapter 4 and 5, using also the analysis method described in Section 2.4.

Note that the smallest spacing of the points at which the load is known, $h = 0.1$ m in Figure 5.3f, is higher than the node spacing 0.175 m/2, since quadratic elements with midside nodes are used. From here on resolution denotes the resolution of the load, coarse being $h = 2$ m and fine being $h = 0.1$ m, uniform is explicitly stated.

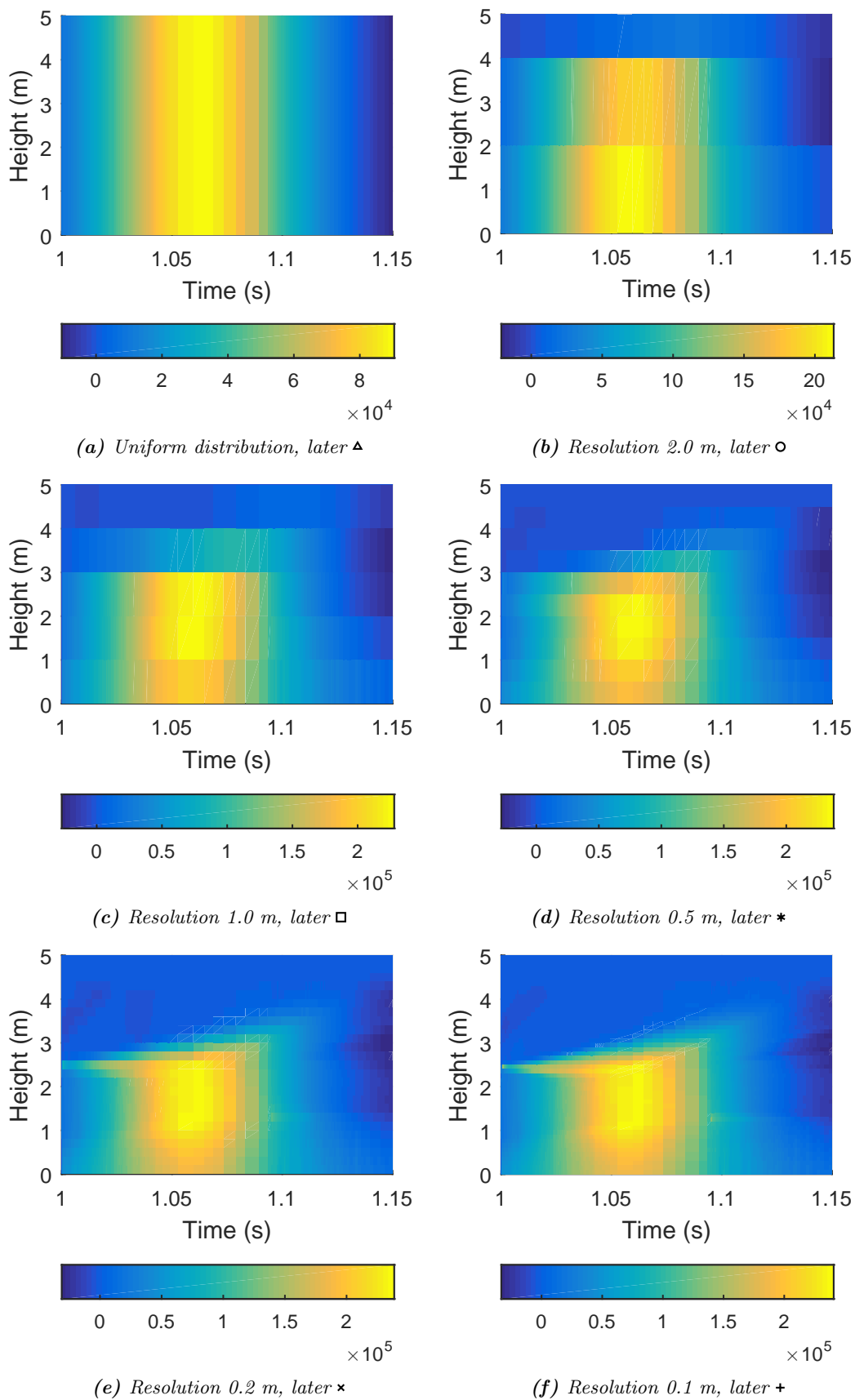


Figure 5.3: Pressure maps (Pa) with different resolutions, near the impact location from start of the impact, derived from the first wave (Figure 5.1a). Time and height scale are shifted to coincide with bottom of the panel and starting time of dynamic simulation.

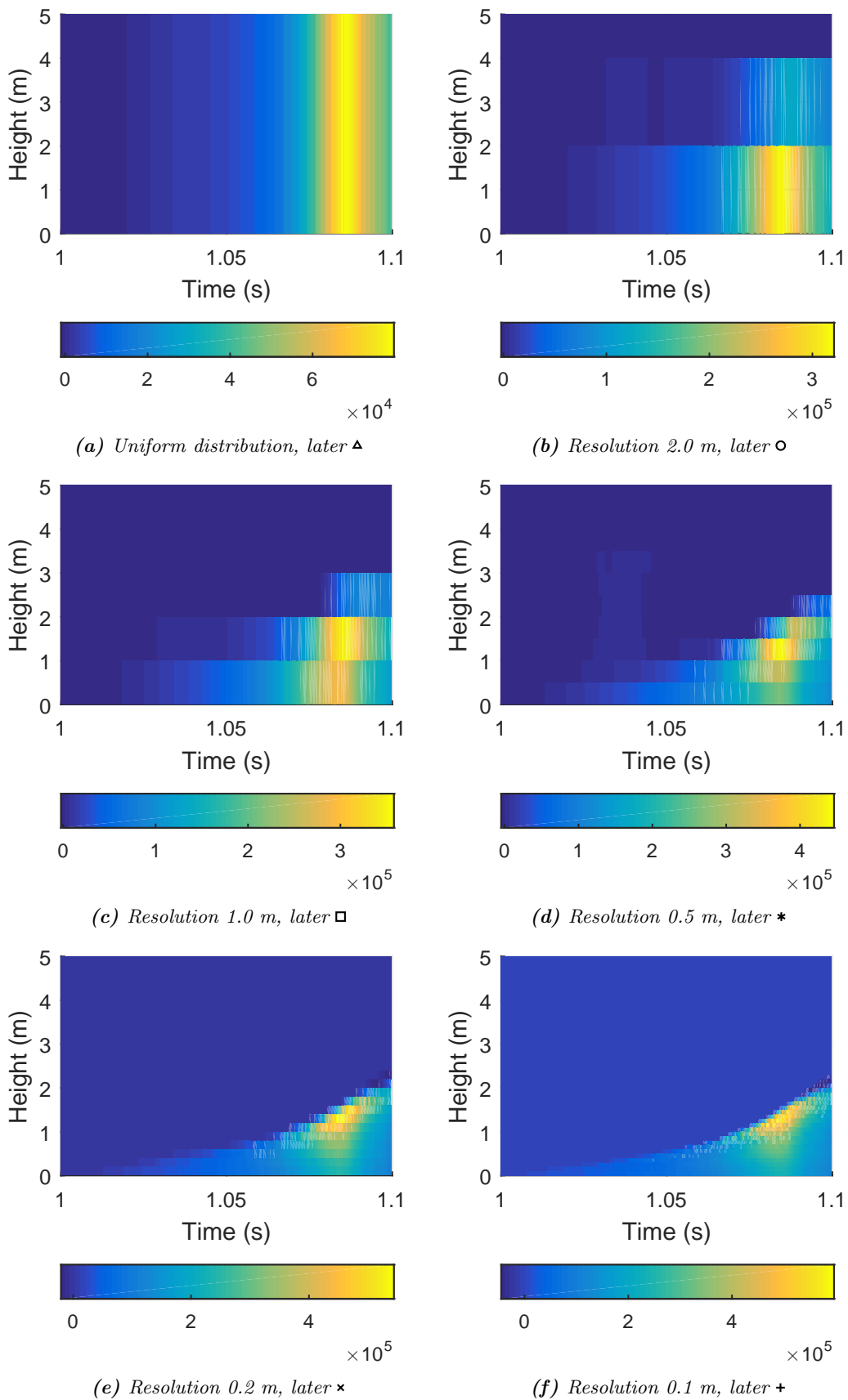


Figure 5.4: Pressure maps (Pa) with different resolutions, near the impact location from start of the impact, derived from the second wave (Figure 5.1b). Time and height scale are shifted to coincide with bottom of the panel and starting time of dynamic simulation.

5.2 Dynamic pressure comparison

A short preview and explanation of the dynamic pressure comparison was given in Section 2.4. The proposed method is tested here. The exact same panel is used, that was described in Chapter 4, with the element size of the flange width, using second order SHELL281 elements of Ansys.

Two loads are applied: an in-plane load and an out-of-plane load (pressure map). The in-plane load is an initial deformation (prestrain) of the boundaries of the stiffened panel, representing wave loads which induce bending moments. These pre-strains are chosen to be at $[0.80, 0.90, 0.95]\delta_c$, where δ_c is the critical displacement of the edges, where the panel fails due to buckling without lateral loading. The critical strains for all directions are shown in Figure 5.5, which is taken from the convergence study for the used mesh density.

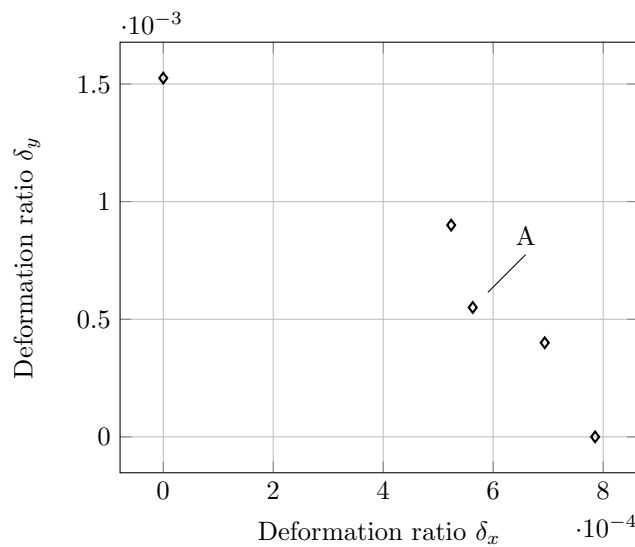


Figure 5.5: Strain at ultimate strength.

As stated before, the comparison of the results is solely based on the ultimate strength of the stiffened panel, after a dynamic wave impact load. A more elaborate discussion of the results of this section is given in Appendix B, by evaluation the state of the structure at different stages of the simulation. It can be read as complementary analysis of the results.

5.2.1 Breaking wave

Figure 5.6 shows a comparison of two time traces following the procedure explained in Figure 2.9. The thick lines represent the fore end mean stress ratio and the thin lines represent the top end mean stress ratio; two reaction forces for two displacement controlled directions. The solid lines are for a fine resolution of $h = 0.1$ m and the fine lines for a coarse resolution of $h = 2.0$ m. The following observations are made regarding the reaction forces:

1. The results are exactly the same in the linear region ($t < 0.7$ s). After that, differences are noted due to applying a very small pressure load (prior to impact) statically to the structure.
2. The dynamic part of the calculation ($1.0 < t < 1.3$ s) is very similar. During this period the plastic deformations are introduced that will later on lower the ultimate strength of the panel.

3. Negative reaction forces are observed at the initial position ($\delta = 0$), indicating that the panel has a new equilibrium position, for which the boundaries are moved.
4. The new ultimate strength of the panel is, for both resolutions, at approximately the same level. The strain, which is the same at same time for both resolutions, is however not the same. Hence, there is a difference between the structures as a consequence of dynamic loading with both resolutions. However, this difference does not show in the comparison criterion, which is based on normalized reaction force and not strain.

The analysis of load-time curves was simplified by only considering $t > 1.5$ s and then applying the failure criterion explained in Appendix A.

For some points with the highest prestrain, the panel was close to or past the US. The used prestrain is calculated without lateral loading, but the dynamic calculations are performed with lateral loading. The lateral loading therefore contributes to weakening the panel from the start, hence the prestrain in the dynamic calculations is not necessarily before the US. This is however not considered to be bad, as the exceedance of the US is small and the US is a design value of the panel.

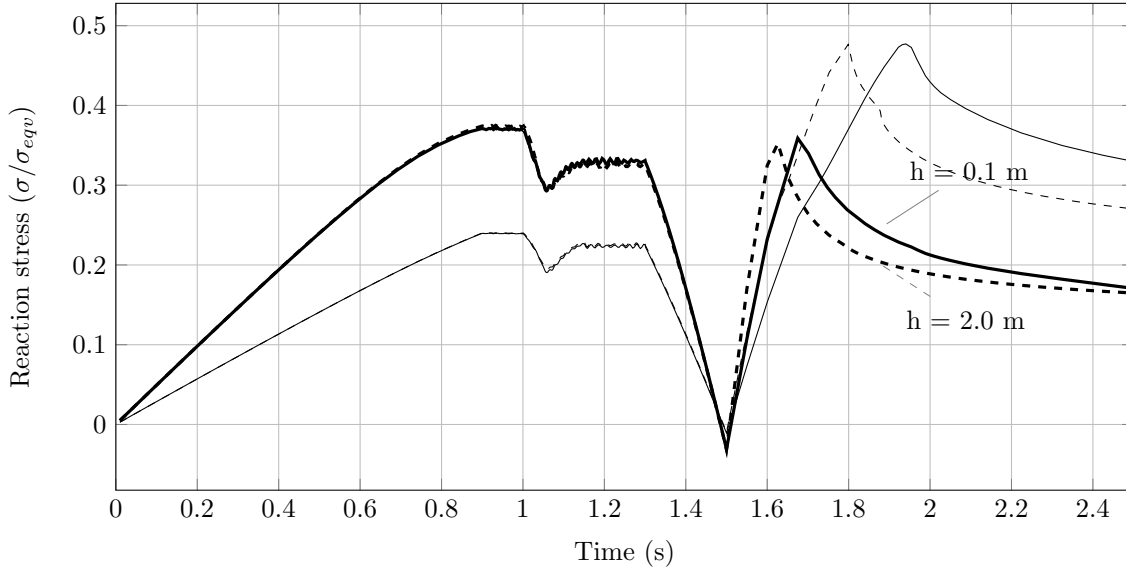
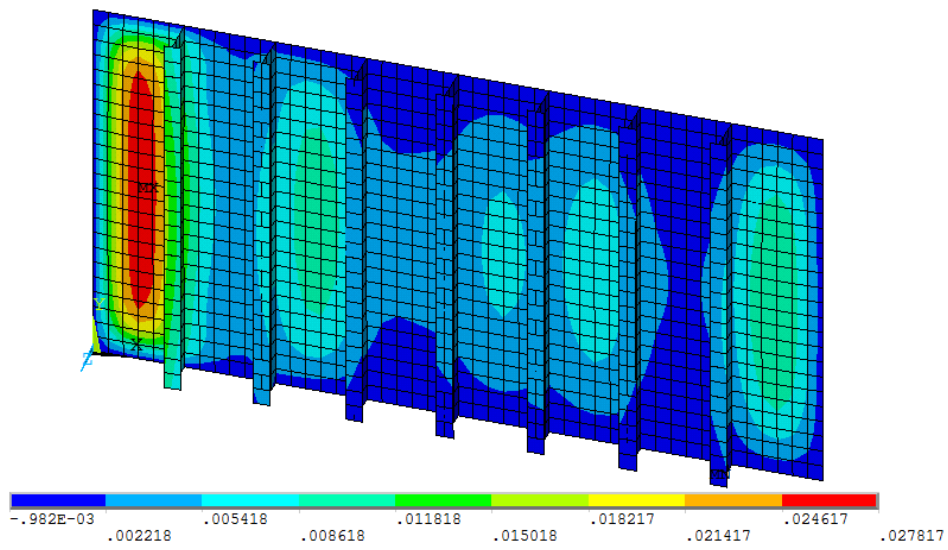


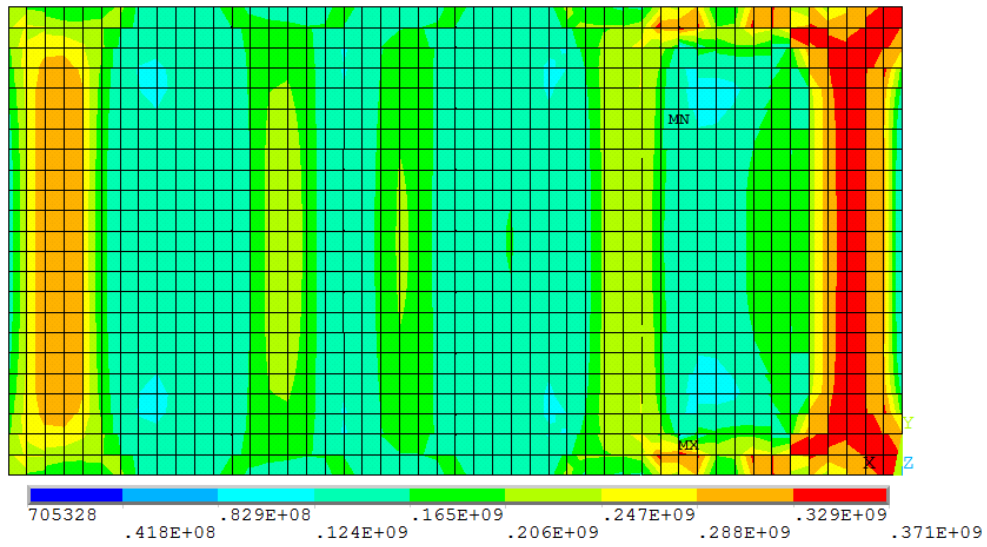
Figure 5.6: Load-time curve of ULS determination of highly dynamic impact loads, with resolution of 0.1 m and 2.0 m (solid and dashed). Load case denoted A in Figure 5.5. Thick lines represent the fore end mean stress ratio and the thin lines represent the top end mean stress ratio.

The out-of-plane displacement, Von Mises stress and first principal strain at the new US of the dashed lines in Figure 5.6 are shown in Figure 5.7. It is directly clear that the buckling mode is not symmetric over the long side of the panel, which it is in Figure 4.5. The external pressure has broken the symmetry, which is also shown in Figure 5.7b (stress). Almost no plastic strain is visible on the panel, only at the corners of the stiffeners near the pressure-loaded area. This detail is shown in Figure 5.7c. This plastic deformation is present from the start of US determination (point 4 in Figure 2.9), hence is introduced during the dynamic loading.

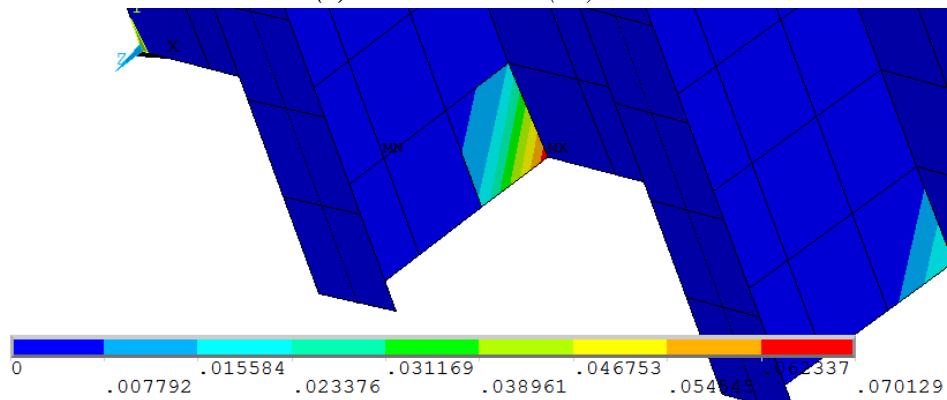
Figure 5.8 shows the ultimate load carrying capacity after dynamic loading for three prestrain levels. The reference US \diamond is determined in the convergence study, shown in Figure 4.6. The following observations are made:



(a) Out of plane deformation (m)



(b) Von Mises stress (Pa)



(c) First principal plastic strain (-) at ends of stiffeners

Figure 5.7: Results of dynamic buckling analysis at the US for equal prestrain on both sides, as denoted 'A' in Figure 5.5.

1. The US after dynamic loading is in all cases lower than without external dynamic loading. Furthermore, the difference between reference and dynamic solution increases as the prestrain increases.
2. The US for different resolutions are, for a prestrain of $0.8\delta_c$ and $0.9\delta_c$, close, in the sense that their magnitude differs no more than $0.05\sigma_{Yeq}$ for each direction.
3. The largest prestrain is most sensitive to variations in the resolution, yet this sensitivity is not related to resolution (the outliers are not always of the same resolution) or loading direction. This observation is confirmed by the other two prestrains.
4. Results of different resolutions are not in line with each other and the origin, hence a different resolution does not result in a 'perfect scaling' of the US.
5. The coarsest resolution with the largest prestrain encloses a non-convex failure surface.
6. The uniform resolution in space is comparable to the reference solution without external loads.

In conjunction with Figure 5.3 it can be questioned whether the location of the pressure has an effect on the US. For the uniform resolution there will obviously not be an effect. For the coarse resolutions $h = [1, 2]$ m the resolution is of the same order as the stiffener spacing (0.955 m) hence the pressure on the panel between a stiffener is quite uniform. For the finer resolutions this is not the case. Hence, finer resolutions are to be more sensitive to location than coarse resolutions.

Following the same procedure as before, a shifted load is applied to the stiffened panel. The load with finest resolution is shifted $s = [0, 0.2, 0.4]$ m downwards, corresponding roughly to the direct impact taking place between stiffeners, at a quarter and on a stiffener. The rest of the load map shifts accordingly, which leads to a slight decrease of the weight of the load.

Figure 5.9 shows the new US for the load shifts, with prestrains of $\delta = [0.8, 0.9, 0.95]\delta_c$. The following observations are made:

1. The difference between load shifts is small, even smaller than of the different resolutions.
2. The loads which are shifted 0.4 m give in most cases the lowest US, whereas the unshifted loads give in most cases the highest US.
3. The shift of load seems to have a larger effect for the middle three cases, in comparison with the two outer cases.
4. A larger prestrain increases the effect of the load shift.

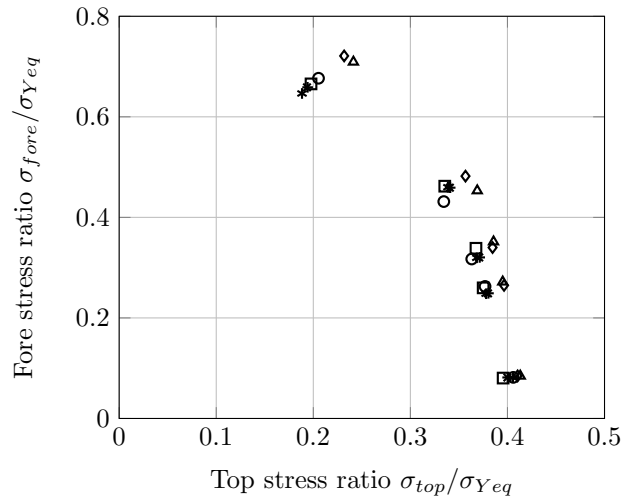
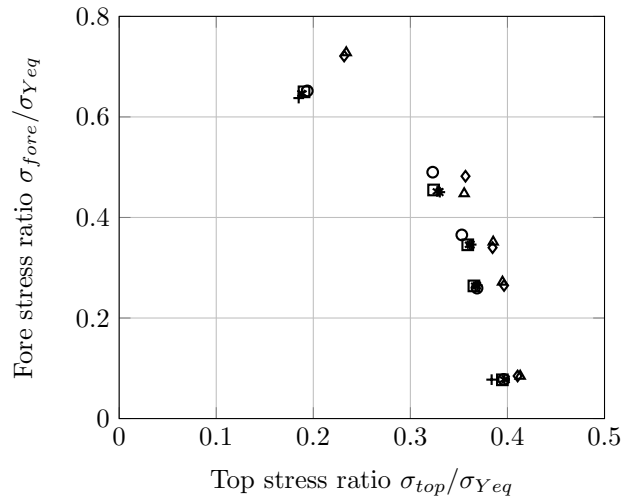
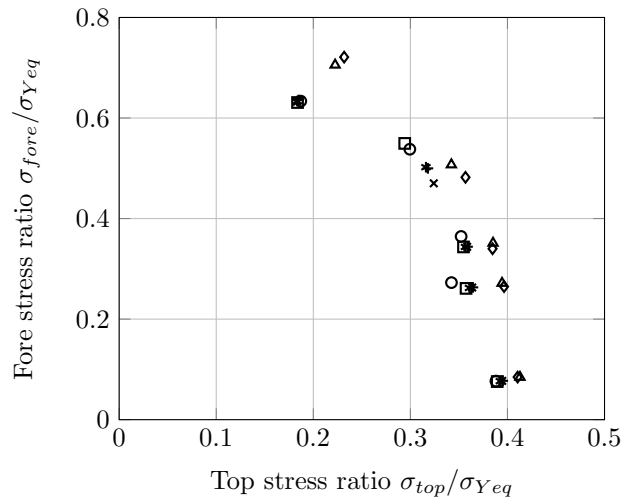
(a) Prestrain of $0.8\delta_c$.(b) Prestrain of $0.9\delta_c$.(c) Prestrain of $0.95\delta_c$.

Figure 5.8: Ultimate strength after lateral impact. Different pressure map resolutions were used for the lateral impact load: +, ×, *, □ and ○ are for a resolution of $h = [0.1, 0.2, 0.5, 1, 2]$ m respectively and ◇ as ultimate strength without lateral loading. Marker △ is uniform in space, but changes in time.

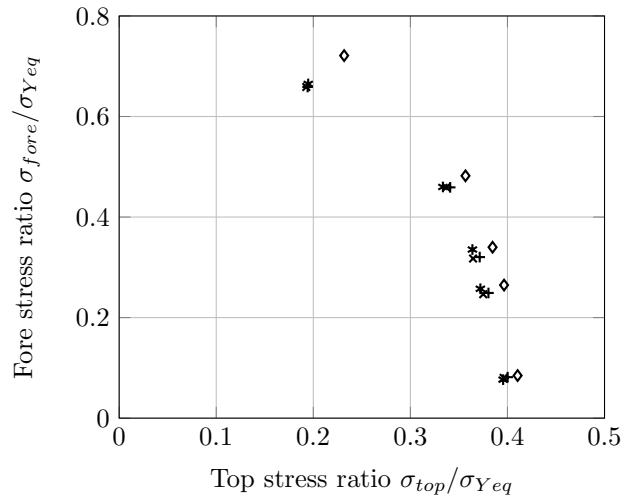
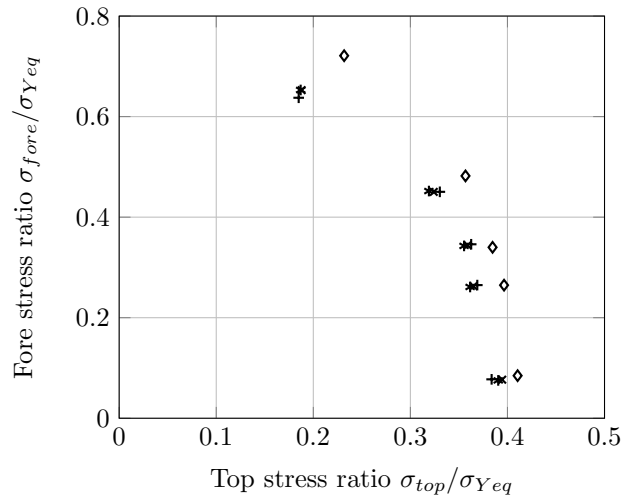
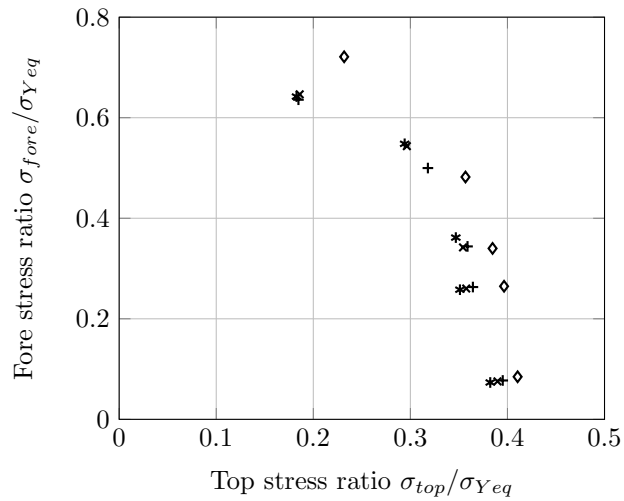
(a) Prestrain of $0.8\delta_c$.(b) Prestrain of $0.9\delta_c$.(c) Prestrain of $0.95\delta_c$.

Figure 5.9: Ultimate strength after lateral impact. Different pressure map shifts were used for the lateral impact load: +, * and * are for a shift of $s = [0.0, 0.2, 0.4]$ m respectively and \diamond as ultimate strength without lateral loading.

5.2.2 Flip-through

Now, the wave described in Figure 5.4 is applied to the structure. The analysis method is the same. The results of the numerical experiment are plotted in Figure 5.10. The following observations are made:

1. The US after dynamic loading is in almost all cases lower than the US without dynamic loading, the only exceptions are a uniform dynamic pressure for a low prestrain.
2. The difference in US between resolutions is, for some loading directions, close to $0.5\sigma_{Y_{eq}}$.
3. The largest prestrain is most sensitive to the change of resolution, as is the loading from fore direction.
4. Different resolutions are not in line, hence there is no scaling caused by resolution change.
5. Regardless of the prestrain it is noted that the $h = 2$ m resolution has the highest US, and is often the biggest outlier.
6. US without loading is in general close or equal to US with dynamic uniform loading.
7. The finest load resolution does not yield the lowest US.

For this load type it can be concluded that there is a difference between the uniform dynamic load and the other resolutions. Especially the resolution of $h = 2$ m overestimates the US of the panel. It however not be said that any of the other load resolutions should be used instead, as the resolutions of $h = [0.1, 0.2, 0.5]$ m compete for this honour.

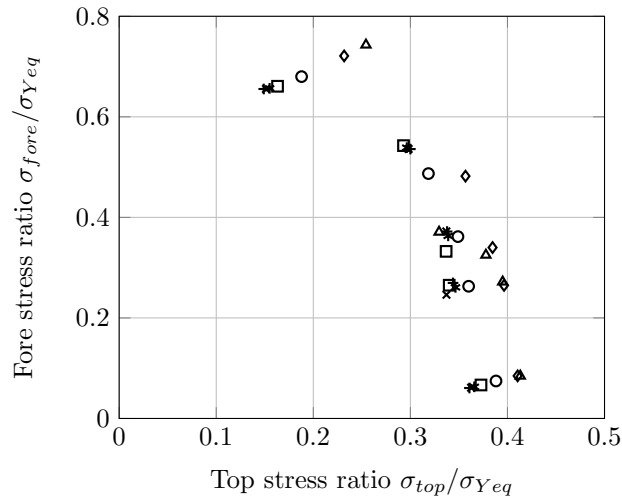
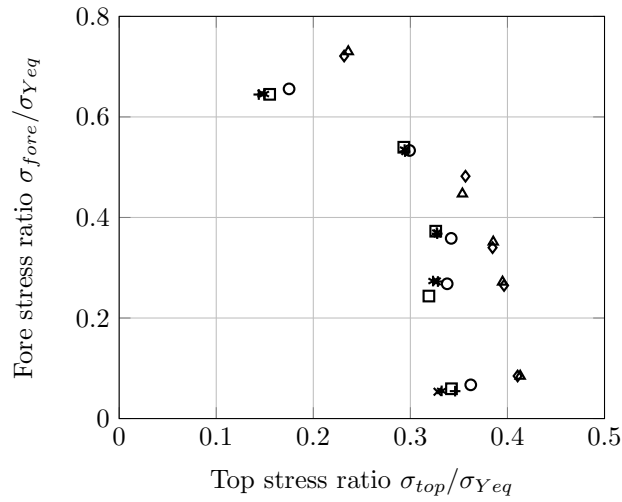
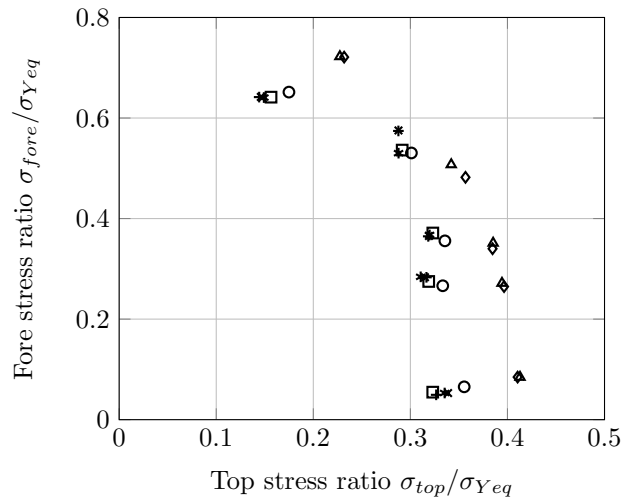
(a) Prestrain of $0.8\delta_c$.(b) Prestrain of $0.9\delta_c$.(c) Prestrain of $0.95\delta_c$.

Figure 5.10: Ultimate strength after lateral impact. Different pressure map resolutions were used for the lateral impact load: +, ×, *, □ and ○ are for a resolution of $h = [0.1, 0.2, 0.5, 1, 2]$ m respectively and ◇ as ultimate strength without lateral loading. Marker △ is uniform in space, but changes in time.

5.2.3 Other scantlings

In Appendix B is observed that the plastic deformation induced by the wave impact occurs always at the end of the stiffener. It might be that the low effect of the resolution is due to the location of the plastic deformation, hence, the failure mode. As an alternative, the size of the stiffeners are drastically decreased, leading to beam-column collapse of the structure, determined from the work of Kaminski 1992. The new dimensions of the stiffened panel are given in Table 5.1. The ultimate strength of the panel is shown in Figure 5.12. The deformation and plastic strain at the yield point in fore compression is shown in Figure 5.11. The panel has a smaller cross-section in the fore direction, hence the ultimate strength in this direction is significantly lower.

Table 5.1: Tee stiffened panel dimension, representative for waterline of an FPSO. Geometry adapted from Table 4.1 to induce beam-column type collapse. New dimensions are in italics.

Panel height	7640	mm
Panel length / stiffener span	4000	mm
Plate thickness	24	mm
Stiffener web height	400	<i>170</i> mm
Stiffener thickness	12.5	mm
Flange width	175	<i>100</i> mm
Flange thickness	20	mm
Stiffener spacing	955	mm

Figure 5.14 shows the displacement and plastic strain at the ultimate strength after dynamic wave impact. The following is observed:

1. The deformation is more global than located between the stiffeners.
2. Plastic strain is the highest at the flange of the stiffener, instead of the end points of the stiffener: a different failure mode than of previous panel.

Because of the change in failure mode, a different reaction to the load and its simplification is expected.

Figure 5.13 shows the new ultimate strength of the panel after applying the wave impact load. The following is observed:

1. The different resolutions give approximately the same failure load, except for $h = 2$ m for pure fore displacement.
2. The uniform dynamic loading is not close to the unloaded panel, also not close to the ultimate strength under a wave impact with any resolution.
3. The decrease in ultimate strength in fore direction does not give a new ultimate strength for wave impact, with only decreased ultimate strength in fore direction.

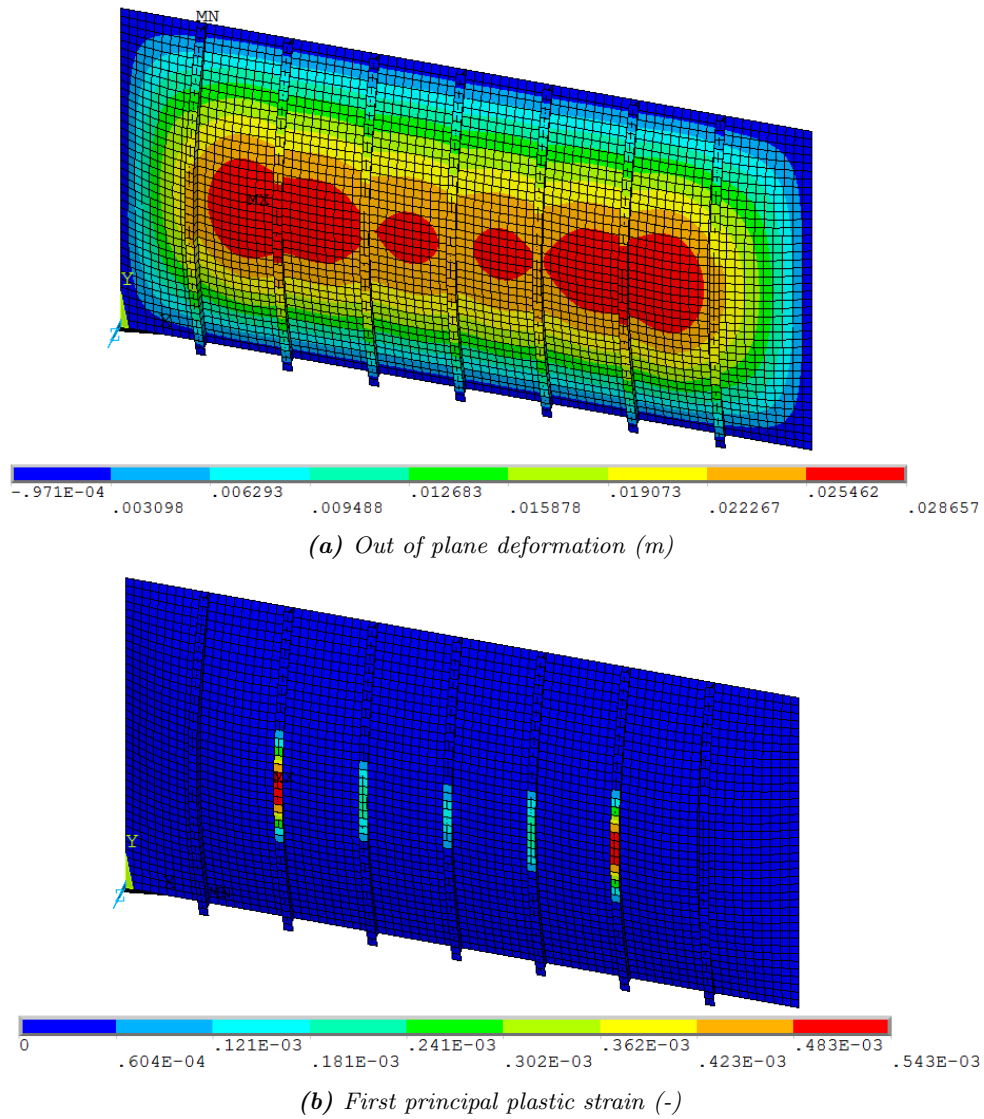


Figure 5.11: Results of quasi-static buckling analysis of the panel form Table 5.1. These figures were generated with an element size equal to the flange thickness, loaded in ship longitudinal direction (on the long end).

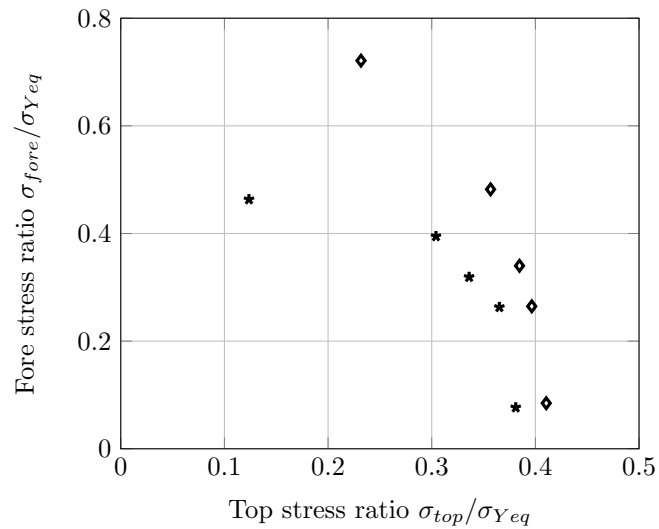


Figure 5.12: Convergence of quasi static buckling, using geometric non-linearities and a non-linear material model. Markers * denotes the ultimate strength of the panel in Table 5.1, \diamond is the ultimate strength of the original panel of Table 4.1.

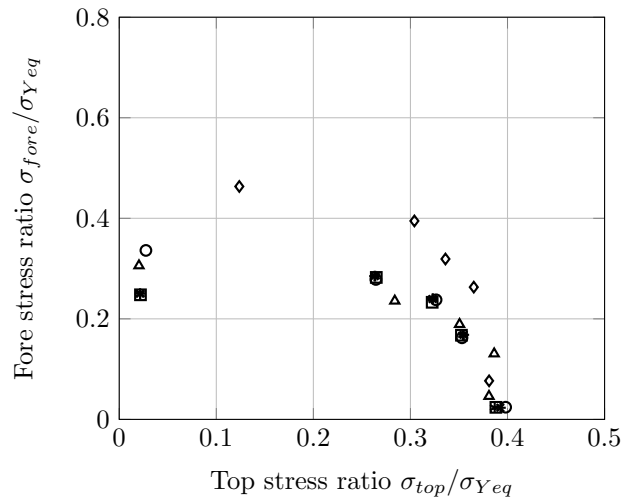


Figure 5.13: Prestrain of $0.9\delta_c$. Ultimate strength after lateral impact. Different pressure map resolutions were used for the lateral impact load: +, x, *, \square and \circ are for a resolution of $h = [0.1, 0.2, 0.5, 1, 2]$ m respectively and \diamond as ultimate strength without lateral loading. Marker \triangle is uniform in space, but changes in time.

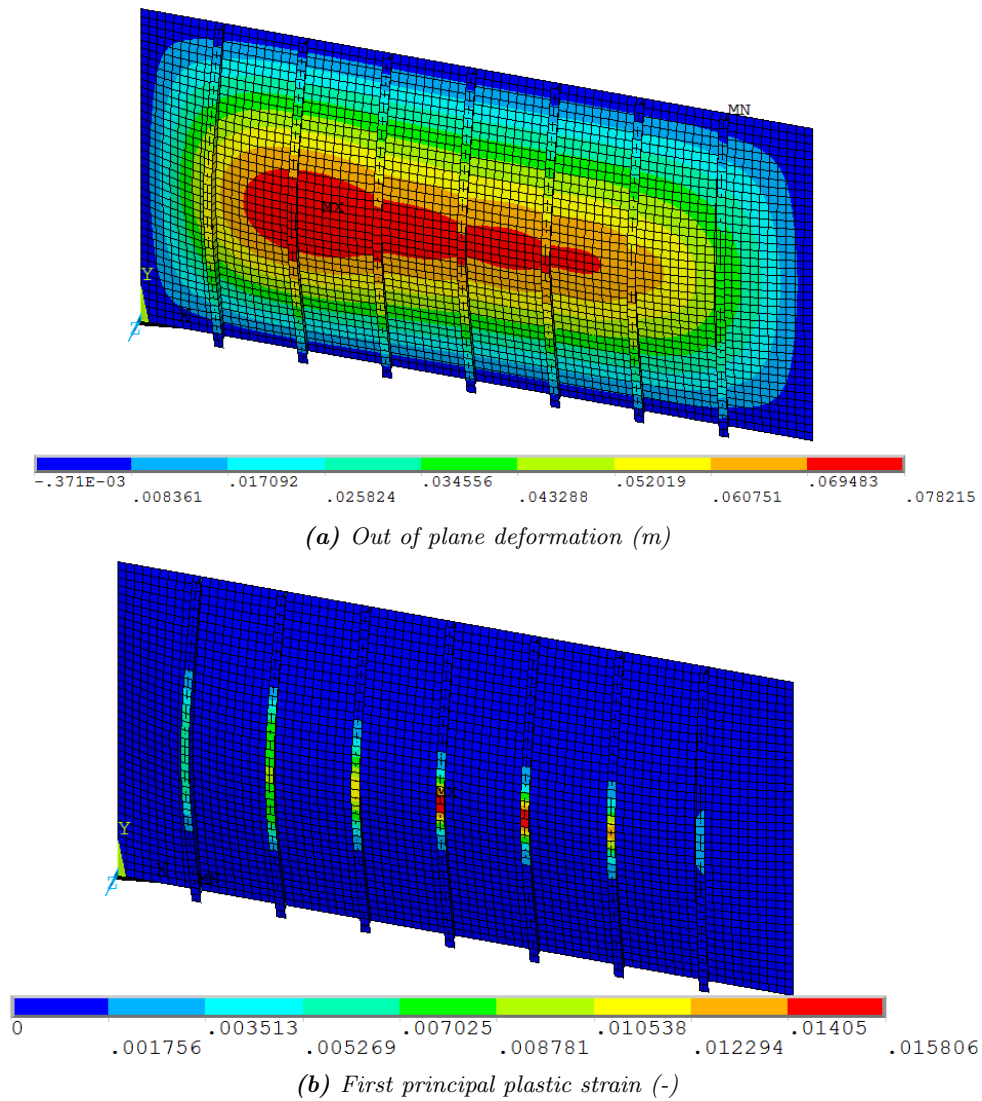


Figure 5.14: Results of dynamic analysis of the panel form Table 5.1, at the new US. Prestrain is in ship longitudinal direction (on the long end).

5.3 Static pressure comparison

The effect of the change of spatial resolution of the load is investigated, by comparing the ultimate strength (US) under the influence of a lateral wave impact load, without taking dynamics into account.

The lateral load or pressure of the wave is static, hence a cross-section of the pressure map in Figure 5.1a at a certain time. At each time instant the maximum and mean pressure are taken. The times at which their maximums occur are at $t = 0.1773$ s) and $t = 0.2367$ s, for the pressure map in Figure 5.1a.

The pressure integrated over the height gives the weight of the pressure, which is $0.7616 \cdot 10^5$ Pa for the highest peak load and $6.3298 \cdot 10^5$ Pa for the highest mean load. These pressure distributions are shown in Figure 5.15, and are close to the times in Figure 5.2. In the first time point ELP 1 is clearly shown: the pressure peak of the direct impact. At the second time point the direct impact is gone, but the gas entrapment gives a broader and lower pressure field, containing more weight than the pressure peak.

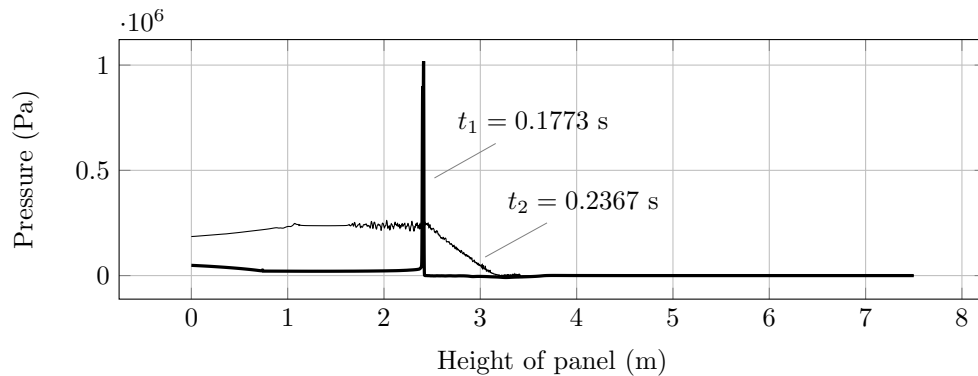


Figure 5.15: Two times at which the peak pressure is highest ($t = 0.1773$ s) and when the average pressure is the highest ($t = 0.2367$ s).

The loads in Figure 5.15 are again interpolated as explained in the previous paragraph, for the same resolutions. The result is shown in Figure 5.16. At the highest peak pressure, the peak is filtered out nearly completely after the highest resolution. If this peak has a large effect on the behaviour of the structure, the difference between the lowest and highest resolution should be visible. It is however questionable, whether the highest resolution is fine enough to capture this peak. The highest average pressure shows that the reduced resolution is able to follow the bulge quite well, and the noise is filtered out by the smoothening. The coarsest resolutions should show significant different result from the finest ones, if the shape of the bulge is important.

The results of the calculation are shown in Figure 5.17, for both the highest peak and highest mean pressure. The following observations are made:

1. The lateral load decreases the US in all cases, but the highest peak load has a much lower effect than the highest mean load.
2. For the highest peak load, the finest resolution results in a lower US than the coarsest resolution. The differences are, however, small.
3. The highest peak load has a shift in US mostly in top mean stress ratio direction between the resolutions. With respect to the reference solution the fore mean stress ratio is dominant.

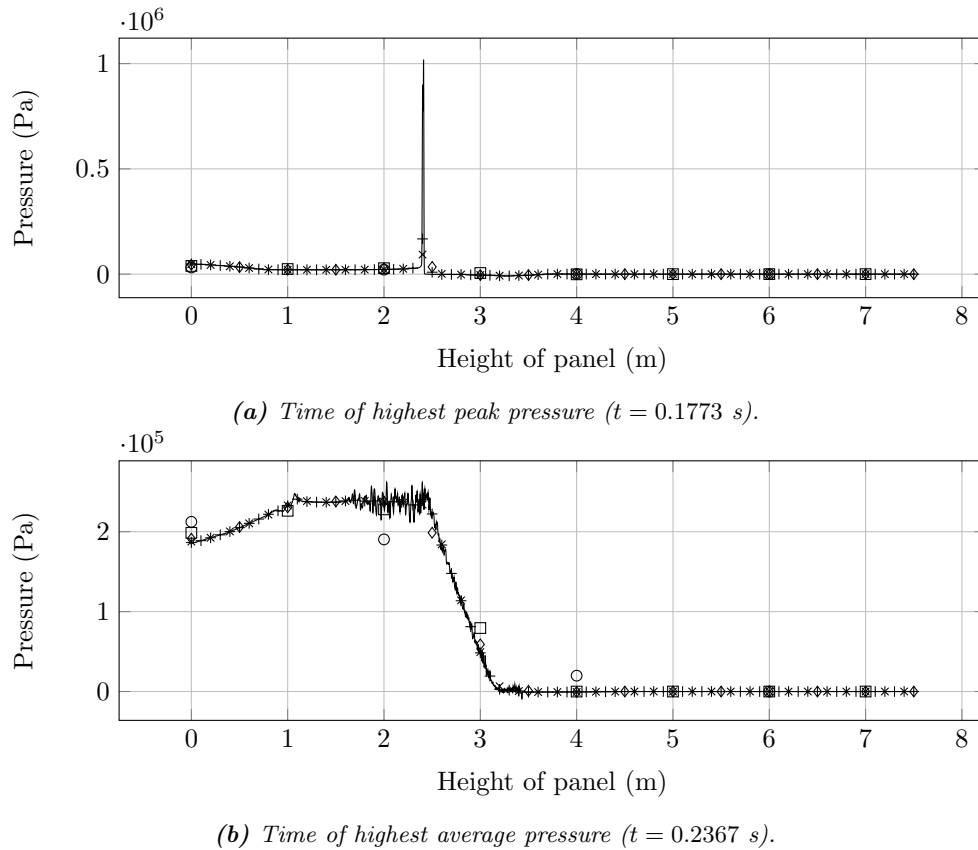
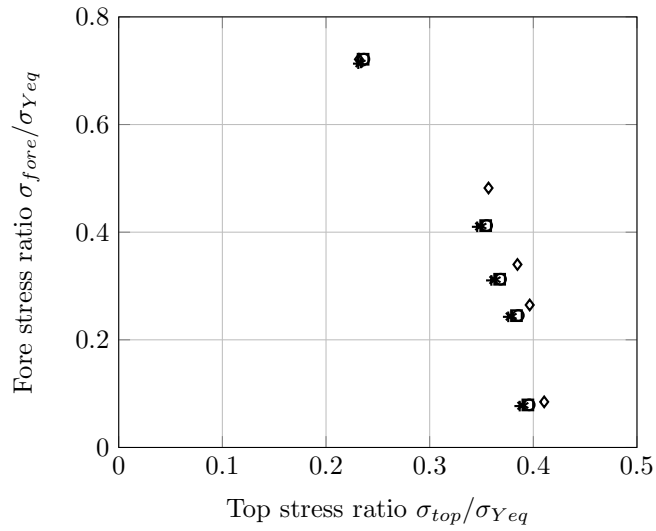


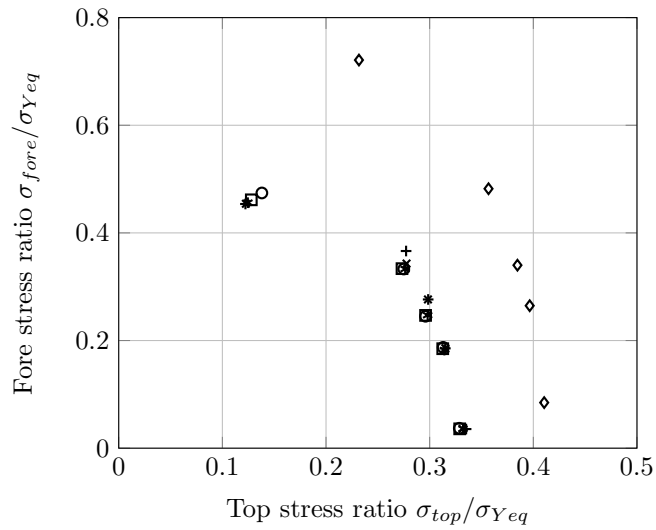
Figure 5.16: Pressure over height for original and different lower resolutions, denoted by +, \times , \diamond , and \circ for $h = [0.1, 0.2, 0.5, 1, 2]$ m respectively.

4. The highest mean load has the greatest effect on the fore mean stress ratio.
5. For the highest mean load, the lateral load has a large effect, but the resolution has a small effect, even smaller than for the peak load.

There is a clear difference between the ultimate strength under influence of both lateral loads. There is at maximum a 5% or $0.05\sigma_{Yeq}$ difference between the different resolutions within one loading direction. Between the two load maps, the difference is much larger. For the high peak load the finest resolution yields the best results. The high average load, which is smooth already, does not show much difference between the different resolutions.



(a) Time of highest peak pressure ($t = 0.1773$ s) as in Figure 5.16a.



(b) Time of highest mean pressure ($t = 0.2367$ s) as in Figure 5.16b.

Figure 5.17: Ultimate strength for five load directions, and five resolutions. Markers +, ×, *, □ and ○ are for a resolution of $h = [0.1, 0.2, 0.5, 1, 2]$ m respectively and ◇ is the reference solution without lateral load.

5.4 Discussion

A dynamic lateral loading was applied to a stiffened panel. The input files of Chapter 2 were used, with the geometry and mesh of Chapter 4. A detailed analysis of some of the results is presented in Appendix B.

5.4.1 Evaluation of results

There is a clear effect of lateral loadings on the US of a stiffened panel: the US decreases under the influence of lateral loading, both for static and dynamic cases. Looking at the parameters in the introduction of this chapter, the relevance of these parameters can be discussed, based on previous results:

- **In-plane prestrain** - The in-plane prestrain has a large influence on the dynamic results in accordance with the expectations, as illustrated in Figure 5.18. A larger prestrain increases the effect of lateral loading, leading to a smaller US. This weakening is not adequately described by a single factor, since the difference is often larger for one dimension than for the other.

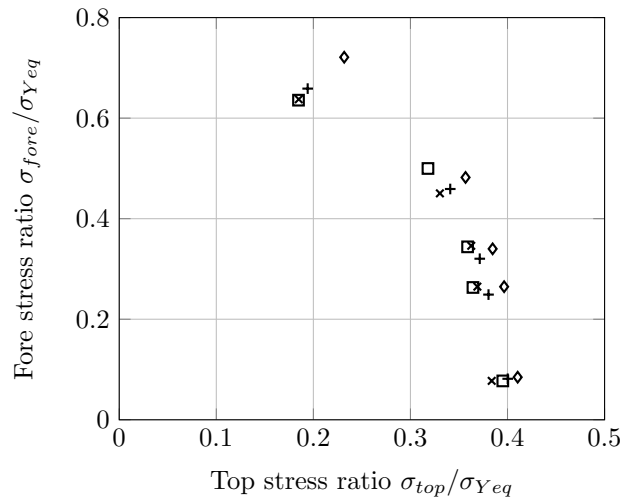


Figure 5.18: Ultimate strength after lateral impact with finest resolution. Different prestrains were used for the lateral impact load: +, x and □ for $\delta = [0.8, 0.9, 0.95]\delta_c$ respectively and ◇ as ultimate strength without lateral loading.

- **Out-of-plane load shape and magnitude** - The lateral load weakens the structure for all prestrain loads, but no universal truth is found regarding the change of resolution, as shown in Figure 5.19, except that the uniform load should not be used at all. It seems that different load resolutions have different failure loads, but these failure loads are close to each other. The same is observed for a shift of the load.

The static lateral load analysis reveals that the shape of the load is of large influence, and differences exist for different load shapes using different resolutions. Comparing to the dynamic US, the static results either overpredict the US, or underestimate it dramatically.

- **Geometry of the panel** - The geometry of the panel influences the failure mode, summarized in Figure 5.20. It is however not possible to scale the ultimate strength under wave impact with the difference in ultimate strength of another panel. The difference between ultimate strength under uniform dynamic loading

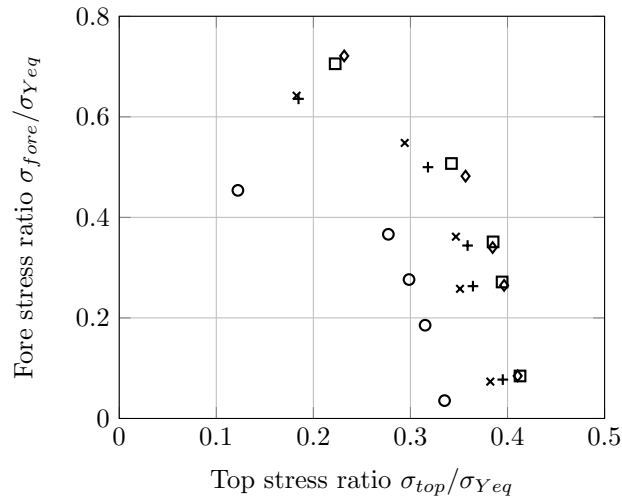


Figure 5.19: Summary, with \diamond as reference US, without wave impact load, $+$ as US with wave impact with finest resolution without shift and \times with largest shift, \circ as static wave impact with highest load resolution. Uniform dynamic loading is \square .

and without loading, which was very small for the original panel, is large for the panel with other failure mode.

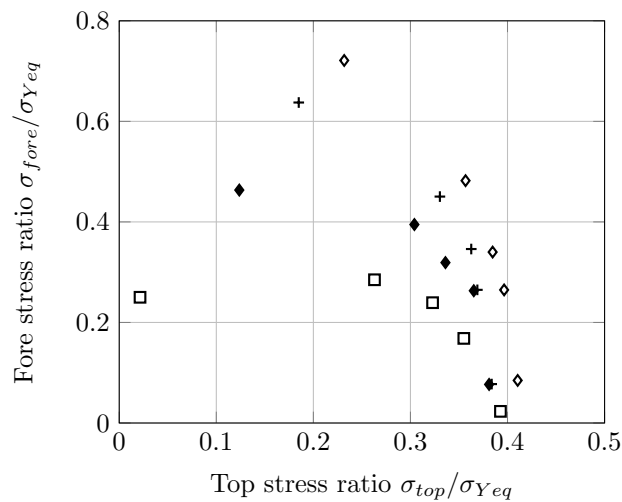


Figure 5.20: Ultimate strength under fine, coarse and uniform loading ($h = 0.1$ m) and reference without wave impact for original panel ($+$ and \diamond) and new, weaker panel (\square and \diamond).

5.4.2 Further possibilities

To make clear how the change of resolution influences the US, a few more analysis methods can be tried:

- Consider only an unstiffened panel between two stiffeners, for that structural member determine the effect of load degeneration. This also allows the use of the full resolution of the load, which was not yet possible.
- Apply more analysis method on the current data, to quantify the effects of resolution change, even though they seem small (such as maximum load norm).

Possibly least squares could be used to 'fit' the ultimate strength to the Von Mises criterium.

- Try different methods of load degradation, such as blurring techniques.
- Reduce the five points which are not uniaxial to two uniaxial points by least squares (hence, reduce the data to a few parameters).

6 Conclusions

Wave impact loads are hard to predict, due to complex physics and difficulties in scaling. To determine the reaction of the structure to a wave impact load, a simpler load might be used, derived from the 'original' wave load. This simpler load is obtained by decreasing the resolution of the wave impact.

The goal of this thesis is to: *develop a method to assess the maximum loss of resolution which can be allowed for load determination, while retaining the ability to predict failure of the local structure*, in order to answer the question *In what detail do loads need to be predicted, in order to predict structural failure?* In this thesis, the structural failure is defined as ultimate strength, after the wave impact.

6.1 Thesis goal

From literature two methods of determining ship strength are identified: direct calculations in the form of FEM and ISUM and its successors. In this thesis, these methods are combined to determine the US under combined in-plane and lateral loading. First, an in-plane displacement is applied quasi-static, then the lateral load is applied dynamically. The plastic strain induced during dynamic loading weakens the structure and decreases the US. Hence, the goal of the thesis is fulfilled.

6.2 Main question

By comparing the finest load resolution with the quasi-static unloaded and the dynamic constant pressure calculation the following conclusion is drawn. Clearly, *using no lateral pressure or applying a uniform dynamic pressure is not detailed enough*.

A first change in detail is to use loads which have a different spatial resolution. A difference is observed between the different resolutions, which is increasing as the pre-strain increases. However, *no clear trend is observed from which one resolution can be preferred over another from a structural point of view*, hence all resolutions, except the uniform dynamic loading are in this case detailed enough. This is confirmed using a second wave impact load.

To verify that the results are not influenced by the location of the load, a downward shift of roughly $s = [1/4, 1/2]l_{\text{span}}$ is applied. A difference is observed between the load shifts, yet the differences are too small to reject the former conclusion.

A second change in detail is the conversion of the dynamic problem to a static problem. Large differences with the US of highest resolution are observed, both in over- and underestimating. Therefore *the dynamic loading and response is important* as omission of it gives large difference with reference solution.

A final consideration is the failure mode of the structure, which can significantly alter the results. This was shown by the uniform loading not representing the failure of the structure well enough.

6.3 Recommendations

Regarding the development of the method the following recommendations are made:

- **Failure criteria** - The failure criteria which is used now is to take the first peak which is encountered in either reaction force, and use that point as US. However, other failure criteria may be used. For instance, the stress may be projected on the displacement direction. This recommendation is addressed in Appendix A.
- **Scale of structure** - A different scale of the structure might be chosen, to see whether the sensitivity to load degeneration is larger or smaller on another scale.

The final recommendation is the best starting point. In the additional analysis it was seen that the part of the panel without wave impact has the same deformed shape as the panel completely without wave impact. Hence, it is likely possible to calculate the strength of the panel under wave impact by only considering the impact region.

Regarding the validation of the method the following recommendations are made:

- **Loading** - Only two waves were tested, more and different waves will lead to more confidence in the method.
- **Degradation mechanism** - Degradation by change of resolution is one of the many ways of load simplification. Possibly the use of image processing techniques leads to different (usable) results. It should however be done with care, to make sure the results are usable in simplification of hydrodynamic loading.
- **Geometry of panel** - Testing the procedure on different geometries would surely increase the confidence in the conclusions. This was already done for a structure with another failure mode, leading to different additional conclusions.

As a starting point it is recommended to attempt to match loading conditions with failure modes. This could for instance be done by finding the most critical ELP for a structure with a certain (unloaded) failure mode.

6 Bibliography

- ANSYS, Inc., ed. (2013). *Theory Reference for the Mechanical APDL and Mechanical Applications*. Version Release 15.0.
- Arciniega, R. and J. Reddy (2007). “Tensor-based finite element formulation for geometrically nonlinear analysis of shell structures”. In: *Computational method in applied mechanics and engineering 197*. Elsevier, pp. 1048–1073.
- Bathe, K.-J. (1996). *Finite Element Procedures*. Prentice Hall.
- Bonet, J. and R. D. Wood (1997). *Nonlinear Continuum Mechanics for Finite Element Analysis*. Cambridge University Press.
- Brannon, R. M. (2004). *Curvilinear Analysis in a Euclidean Space*. University of New Mexico (Supplemental Book Draft).
- Buchner, B. and T. Bunnik (2007). *Extreme Wave Effects on Deepwater Floating Structures*. OTC18493.
- Chapelle, D. and K.-J. Bathe (2003). *The Finite Element Analysis of Shells - Fundamentals*. Computational Fluid and Solid Mechanics. Springer.
- Cho, S.-R. et al. (2012). “Impulse Pressure Loading and Response Assessment”. In: *International Ship and Offshore Structures Congress 2012*. Vol. 2. Schiffbautechnische Gesellschaft Hamburg, pp. 275–329.
- Cook, R. D. et al. (2002). *Concepts and Applications of Finite Element Analysis*. Fourth Edition. John Wiley and Sons, Inc.
- Det Norske Veritas AS, ed. (2013). *Determination of Structural Capacity by Non-linear FE analysis Methods*. DNV-RP-C208.
- Düster, A. and E. Rank (2001). “The p-version of the finite element method compared to an adaptive h-version for the deformation theory of plasticity”. In: *Computational Methods in Applied Mechanics and Engineering*. Elsevier, pp. 1925–1935.
- Dvorkin, E. N. and K.-J. Bathe (1984). “A continuum mechanics based four-node shell element for general non-linear analysis”. In: *Engineering with Computers*. Pineridge Press Ltd, pp. 77–88.
- Faltinsen, O. M. (1990). *Sea Loads on Ships and Offshore Structures*. Cambridge University Press.
- Ferziger, J. and M. Perić (2002). *Computational Methods for Fluid Dynamics*. Springer-Verlag.
- Guilcher, P. et al. (2014). “2D Simulations of Breaking Wave Impacts on a Flat Rigid Wall - Part 1: Influence of the Wave Shape”. In: *Proceedings of the Twenty-fourth (2014) International Ocean and Polar Engineering Conference*. International Society of Offshore and Polar Engineers, pp. 232–245.
- Holzappel, G. A. (2000). *Nonlinear Solid Mechanics. A continuum approach for engineering*. John Wiley & Sons Ltd.
- Hughes, T. J. R. (2003). *The Finite Element Method. Linear Static and Dynamic Finite Element Analysis*. Dover Civil and Mechanical Engineering.
- International Association of Classification Societies, ed. (2012). *Common Structural Rules for Double Hull Oil Tankers*.
- Kaminski, M. (1992). “Cyclic compression of imperfect steel plates”. PhD thesis. Delft University of Technology.
- Lafeber, W., L. Brosset, and H. Bogaert (2012). “Elementary Loading Processes (ELP) involved in breaking wave impacts: findings from the Sloskel project”. In: *Proceedings of the Twenty-second (2012) International Ocean and Polar Engineering Conference*. International Society of Offshore and Polar Engineers, pp. 265–276.

- Larsson, L. and H. C. Raven (2010). *Ship Resistance and Flow*. Ed. by J. R. Paulling. The Principles of Naval Architecture. The Society of Naval Architects and Marine Engineers.
- Lubliner, J. (2008). *Plasticity Theory*. Page numbers refer to online PDF, available for free in a legal way. Dover books on engineering.
- McGinty, B. (2012). *Continuum Mechanics. With emphasis on metals & viscoelastic materials*. <http://www.continuummechanics.org/cm/index.html>.
- Monaghan, J. (1992). “Smoothed Particle Hydrodynamics”. In: *Annual Review of Astronomy and Astrophysics*. Annual Reviews Inc., pp. 543–574.
- Okumoto, Y. et al. (2009). *Design of Ship Hull Structures*. Springer-Verlag Berlin Heidelberg.
- Özgül, O., P. K. Das, and N. Barltrop (2007). “The new simple design equations for the ultimate compressive strength”. In: *Ocean engineering 34*. Elsevier, pp. 970–986.
- Paik, J. K. et al. (2012). “Ultimate Strength”. In: *International Ship and Offshore Structures Congress 2012*. Vol. 1, pp. 285–363.
- Paik, J. K. (2010). “Large Deflection Behavior and Ultimate Strength of Stiffened Panels”. In: *Ship Structural Analysis and Design*. The Society of Naval Architects and Maritime Engineers, 15:1–15:26.
- Paik, J. K. and O. Hughes (2012). “Deformation and Strength Criteria for stiffened Panels Under Impact Pressure”. In: *Ship Structural Analysis and Design*. Society of Naval Architects and Marine Engineers, 10:1–10:8.
- Paik, J. K., G. Wang, and A. K. Thayamballi (2002). “Ultimate Limit State Design of Ship Hulls”. In: *SNAME Transactions*. Vol. 110, pp. 85–114.
- Paik, J., B. J. Kim, and J. K. Seo (2008). “Methods for ultimate limit state assessment of ships and ship-shaped offshore structures: Part II stiffened panels”. In: *Ocean Engineering 35*. Elsevier Science Ltd., pp. 271–280.
- Paik, J. and A. Thayamballi (2003a). “A concise introduction to the idealized structural unit method for nonlinear analysis of large plated structures and its application”. In: *Thin-Walled Structures 41*. Elsevier Science Ltd., pp. 329–355.
- (2003b). *Ultimate Limit State Design of Steel-plated Structures*. John Wiley and Sons Ltd.
- Reddy, J. (1984). *An Introduction to the Finite Element Method*. McGraw-Hill Book Company.
- (1991). *Theory and Analysis of Elastic Plates*. Taylor & Francis.
- Rogers, R. C. (1993). “Derivation of Linear Beam Equations Using Nonlinear Continuum Mechanics”. In: *Zeitschrift für angewandte Mathematik und Physik*. Birkhäuser Verlag, Berlin, pp. 732–754.
- Rules for the classification of ships* (2015). Det Norske Veritas.
- Sayas, F.-J. (2008). *A gentle introduction to the Finite Element Method*. <http://www.math.udel.edu/~fjsayas/anIntro2FEM.pdf>.
- Shoemaker, A. K. (1981). “Fracture Characteristics of Ship Steel under Extremely High Loading Rates”. In: *Extreme Loads Response Symposium*. Society of Naval Architects and Marine Engineers, pp. 177–188.
- Smith, C. (1977). *Influence of local compressive failure on ultimate longitudinal strength of ship's hull*.
- The European Union, ed. (2002). *EN 1990: Eurocode - Basis of structural design*. EN 1990:2002+A1.
- Ueda, Y. and S. Rashed (1974). *An ultimate transverse strength analysis of ship structures*.
- Willam, K. J. (2002). “Constitutive Models for Engineering Materials”. In: *Encyclopedia of Physical Science & Technology*. Academic Press, pp. 603–633.
- Wriggers, P. (2008). *Nonlinear Finite Element Methods*. Springer.
- Xu, M. C. et al. (2013). “Influence of boundary conditions on the collapse behaviour of stiffened panels under combined loads”. In: *Marine Structures 34*. Elsevier, pp. 205–225.

A Classification of failure

The method of determining the ultimate load carrying capacity is based on the maximum of the reaction forces with a displacement controlled simulation. This appendix will explain in detail how this point is determined and, based on the recommendations after numerical experiments, gives a possible improvement of this criterium. This will be done by analyzing some load-end shortening curves.

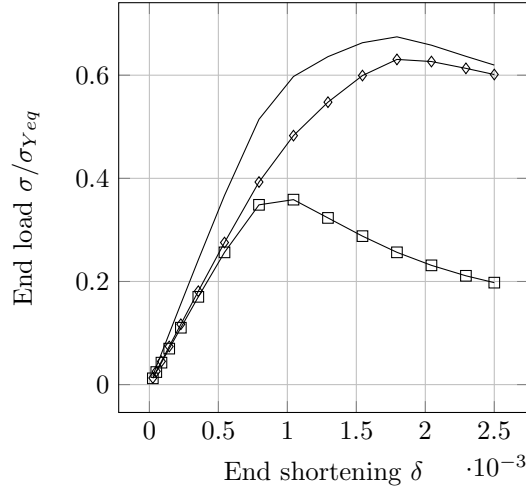


Figure A.1: Load-end shortening curve of biaxially loaded panel, with \square as component on top end, \diamond as component on fore end and — in displacement direction (top:fore = $1/2:\sqrt{3}/2$). No external loading, quasi-static with panel geometry as in Table 4.1.

Figure 2.6 shows the reaction forces plotted as function of edge displacement. The reaction forces are non-dimensionalized by Equation 2.2 and the end shortening by:

$$\delta = \frac{\Delta x}{L} \quad (\text{A.1})$$

where Δx is the edge displacement and L the length of the panel in displacement direction. Hence, it is a strain, but on the structural unit level. For the biaxial experiments the end shortening is represented by:

$$\delta = \sqrt{\delta_x^2 + \delta_y^2} \quad (\text{A.2})$$

where δ_x and δ_y represent the two directions.

Figure A.1 shows the two reaction stresses. In this thesis, the first maximum of either reaction stresses is taken as yield point of the panel. For this specific case, in which

biaxial deformations are applied with a ratio of (top:fore = $1/2:\sqrt{3}/2$), this results in breakdown of the curve for top reaction stress, while the fore reaction stress still increases. The obtained point on the USC is $\sigma_f/\sigma_{Yeq} = 0.483$ and $\sigma_t/\sigma_{Yeq} = 0.359$.

In Figure A.1 a third line is drawn, combining the reaction stresses and projecting them on the displacement direction. It is clear that this gives a much higher maximum, easily explained by the fact that the fore boundary is displaced much more than the top boundary, hence this reaction force is weighed more. The alternative point on the USC is $\sigma_d/\sigma_{Yeq} = 0.674$, which has a norm $0.07\sigma_{Yeq}$ higher than the previous point. Hence, this measure defines (in this case) a larger failure surface, hence the structure can be considered safer. Also, result comparison is easier because every test corresponding to one displacement direction can be evaluated with one value, instead of two.

In Figure A.2 the two failure criteria are compared. Except for one load direction, all the points determining the alternative method are outside the original method. This indicates that the original method is conservative, and the alternative method could be used.

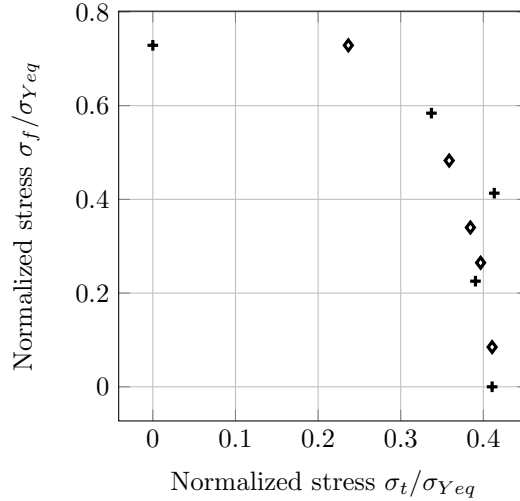


Figure A.2: Ultimate load carrying capacity calculated in alternative way +, compared to the normal way diamond also shown in Figure 4.6.

This is however not the whole story. There is also a second component to the load, comparable to the Poisson effect in uniaxial loading of a bar. It might be that the reaction forces orthogonal to the loading direction decrease before the ultimate strength is reached. Then, a perturbation of the loading direction towards this orthogonal direction can lead to collapse.

In conclusion, the second error measure (not used in the thesis) is easier to compare and gives (also for other load directions than mentioned here) a higher ultimate strength. It is however not guaranteed that the structure will not collapse due to change of load direction during the experiment.

B Detailed results analysis

In this appendix a detailed analysis is presented of the ultimate strength assessment of the stiffened panel, loaded with a prestrain of $\delta = 0.9\delta_c$. Comparison is made between the finest resolution $h = 0.1$ m, a coarse resolution of $h = 2.0$ m and a uniform dynamic load with a resolution of $h = 7.64$ m.

Note: During application of the prestrain, the first 'step' of the wave impact load is applied. Hence, the deformation patterns shown with prestrain are not necessarily symmetric.

B.1 Dynamic load analysis $h = 0.1$ m, breaking wave

A breaking wave impact is modelled with the finest resolution, see Figure 5.3f. Load direction is compression of the fore end, no displacement of top end. The normalized reaction forces over time are plotted in Figure B.16.

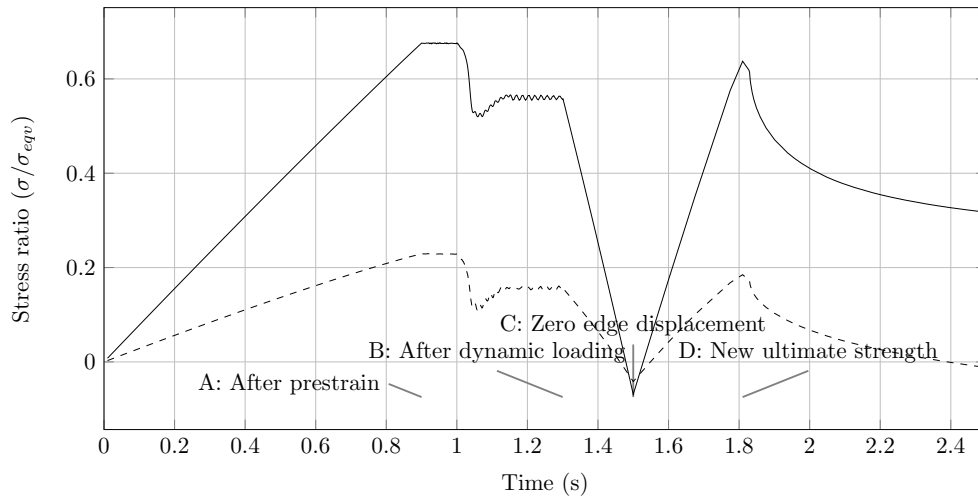


Figure B.1: Reaction forces over time normalized by the yield stress, due to compression of fore end. Dashed line is top end and solid line fore end, $h = 0.1$ m, $\delta = 0.9\delta_c$.

A: After prestrain Figure B.2 shows the structure after prestrain is applied. The out-of-plane deformation is shown, as well as the first principle plastic strain. The structure is more deformed on the lower end of the panel, due to the applied static wave impact loading. Plastic strain is very small, and concentrated at either the ends of the stiffeners or the last interstiffener plate.

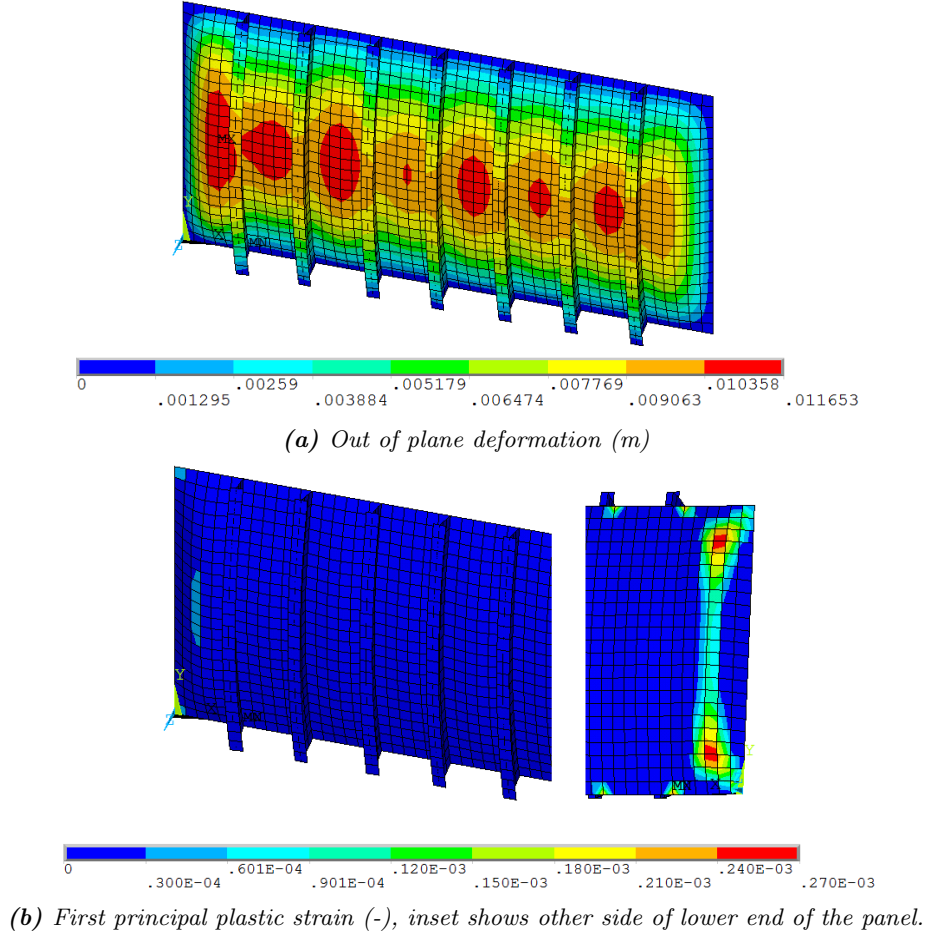
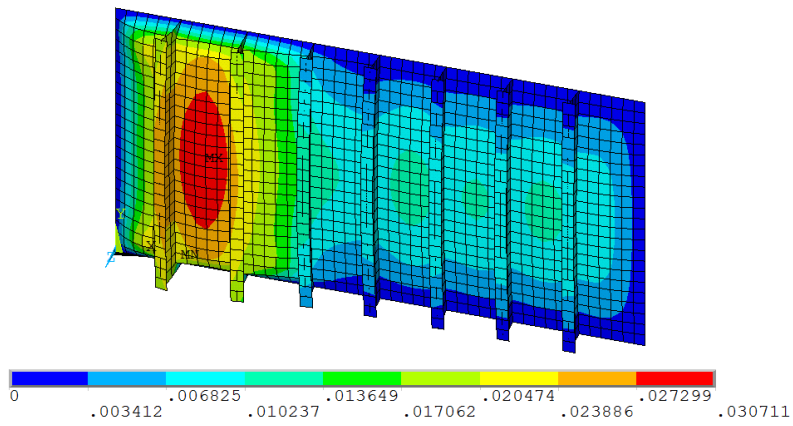


Figure B.2: Structure after prestrain, $h = 10$ cm, $\delta = 0.9\delta_c$.

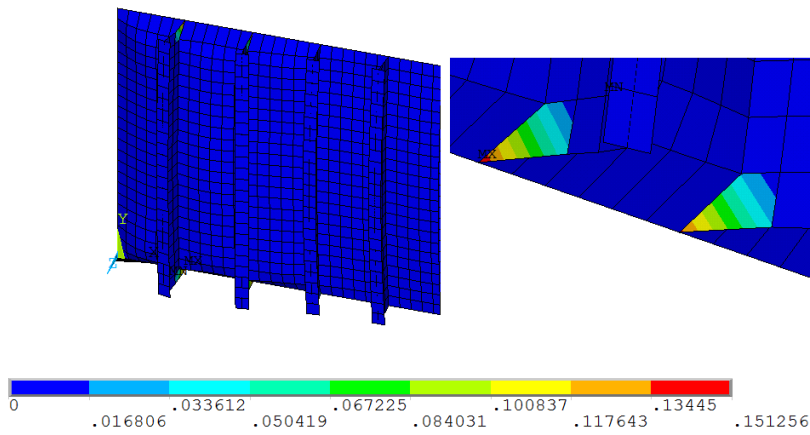
B: After dynamic loading Figure B.3 shows the structure after dynamic loading, but still under prestrain. The out-of-plane displacements on part without wave impact increased by roughly 30%, and the out-of-plane displacements on part with wave impact increased by roughly 200%. The plastic strain is also much higher, and localized to the corners of the stiffeners.

C: Zero edge displacement Figure B.4 shows the structure without edge displacement. All deformations at this point are due to plastic strains induced during the prestrain and wave impact. Clearly the location of wave impact is mostly deformed, whereas the rest of the structure has no significant changes.

D: New ultimate strength Figure B.5 shows the structure at its new ultimate strength. The deformation of the structure is very similar to that after dynamic loading, except that the half waves are wider and connected. The plastic strains are lower than after dynamic loading, indicating that the structure has regained some of its strength by bringing it back to zero edge displacement, also visible in the negative reaction force at point C in Figure B.16.



(a) Out of plane deformation (m)



(b) First principal plastic strain (-), inset shows other side of lower end of the panel.

Figure B.3: Structure after dynamic loading., $h = 10$ cm, $\delta = 0.9\delta_c$

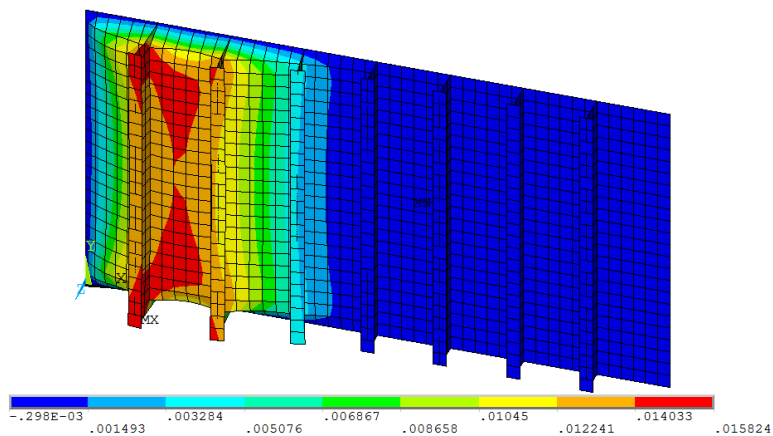


Figure B.4: Out of plane deformation (m) at original edge displacement, $h = 10$ cm, $\delta = 0.9\delta_c$.

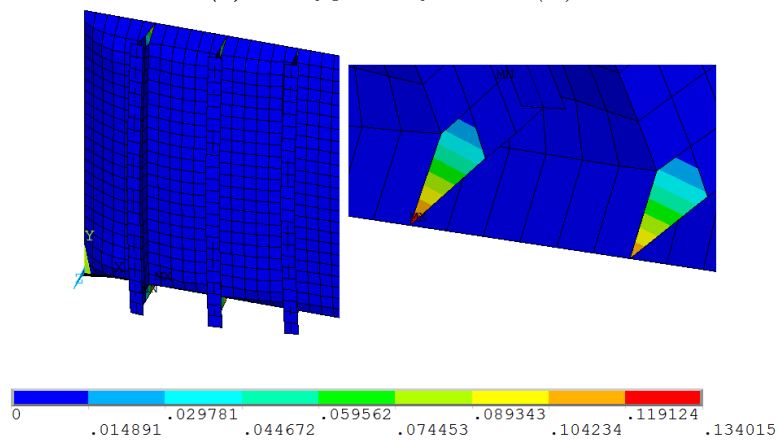
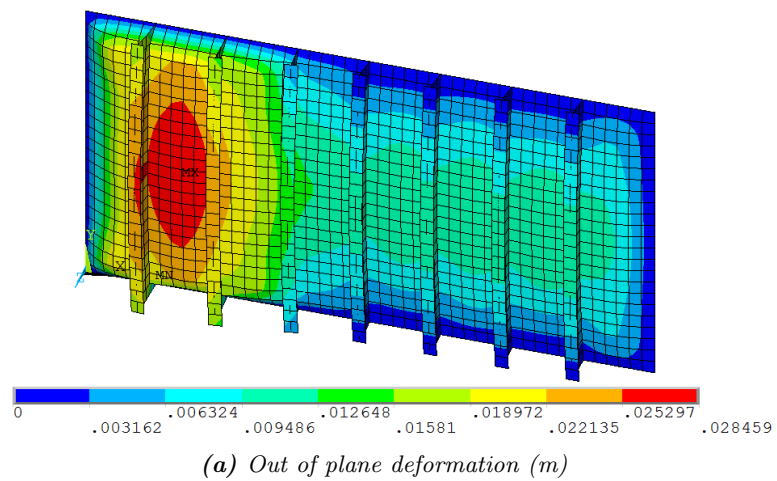


Figure B.5: Structure after dynamic loading, $h = 10$ cm, $\delta = 0.9\delta_c$.

B.2 Dynamic load analysis $h = 2.0$ m, breaking wave

The breaking wave impact with a coarse resolution of $h = 2.0$ m from Figure 5.3b is used here. The normalized reaction forces over time are plotted in Figure B.6. Note the similarities between this figure and Figure B.16, in which a higher resolution for the wave impact is used. The differences are explained for each point indicated in the plots.

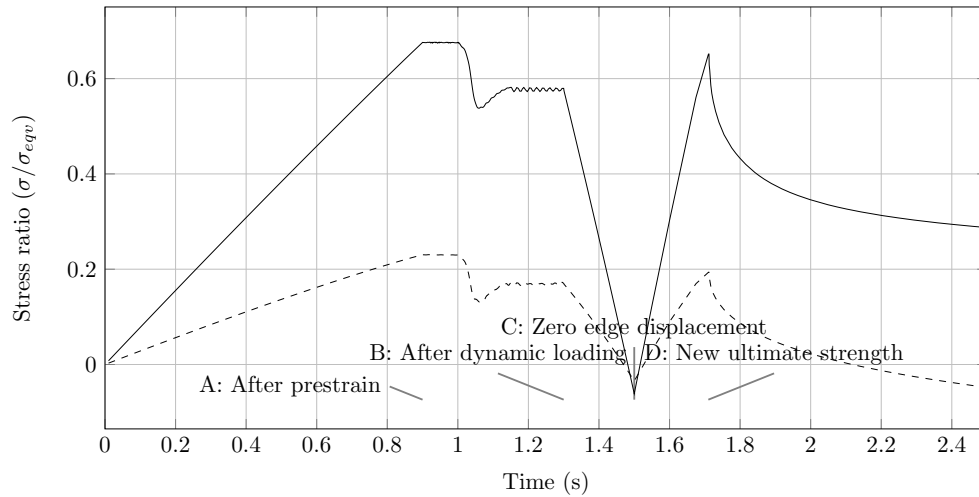


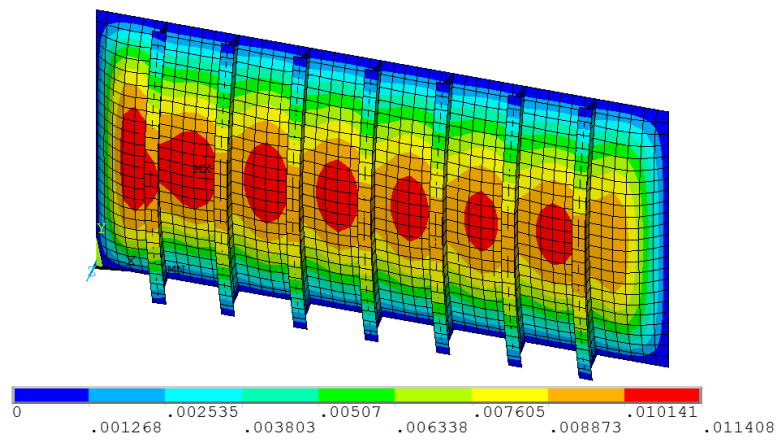
Figure B.6: Reaction forces over time normalized by the yield stress, due to compression of fore end. Dashed line is top end and solid line fore end, $h = 2.0$ m, $\delta = 0.9\delta_c$.

A: After prestrain Figure B.7 shows the structure after prestrain is applied. The out-of-plane displacement has the same shape as with the resolution of $h = 0.1$ m, it seems that the peaks are slightly wider and lower. A coarser resolution gives a coarser deformation pattern. The plastic strain is also very similar.

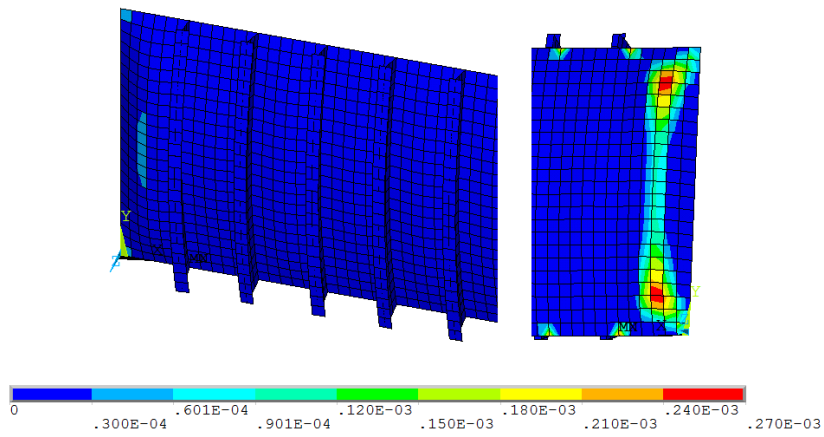
B: After dynamic loading Figure B.8 shows the structure after dynamic loading, but still under prestrain. As with the previous point, the deformation is slightly lower and wider, although the differences are minimal. The location of plastic strain is identical and the magnitude of the maximum about 10% lower than for the finest resolution.

C: Zero edge displacement Figure B.9 shows the structure without edge displacement. The difference in plastic strain is directly visible in the deformation of the structure in its original position. For the resolution of $h = 2.0$ m, the deformation is large at the edges, whereas the resolution of $h = 0.1$ m is more to the centre of the panel. Again, a 10% difference in maximum is observed.

D: New ultimate strength Figure B.10 shows the structure at its new ultimate strength. Again, the deformation is very similar to that of the resolution $h = 0.1$ m, with a wider and slightly lower peak. Also, the maximum plastic deformation are 10% lower, in accordance with earlier observations.

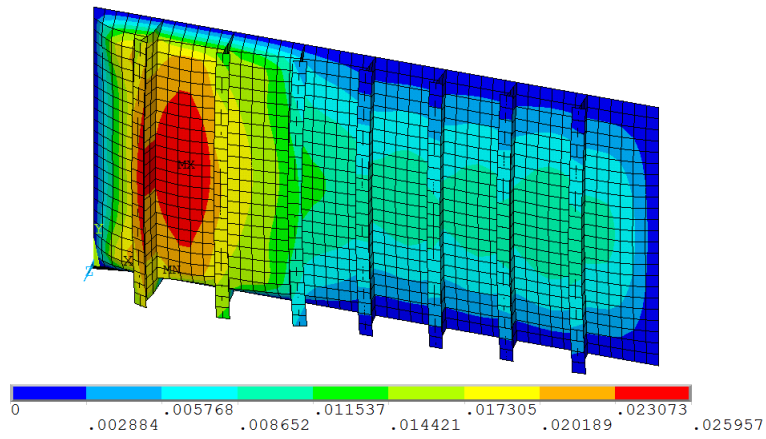


(a) Out of plane deformation (m)

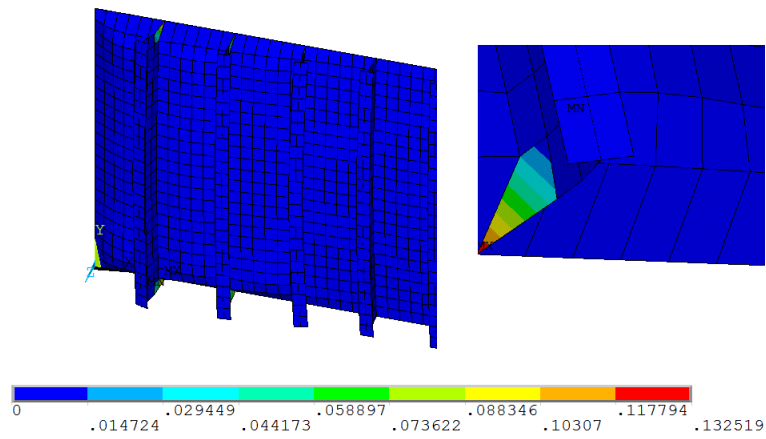


(b) First principal plastic strain (-), inset shows other side of lower end of the panel.

Figure B.7: Structure after prestrain, $h = 2.0$ m, $\delta = 0.9\delta_c$.



(a) Out of plane deformation (m)



(b) First principal plastic strain (-), inset shows other side of lower end of the panel.

Figure B.8: Structure after dynamic loading, $h = 2.0 m$, $\delta = 0.9\delta_c$.

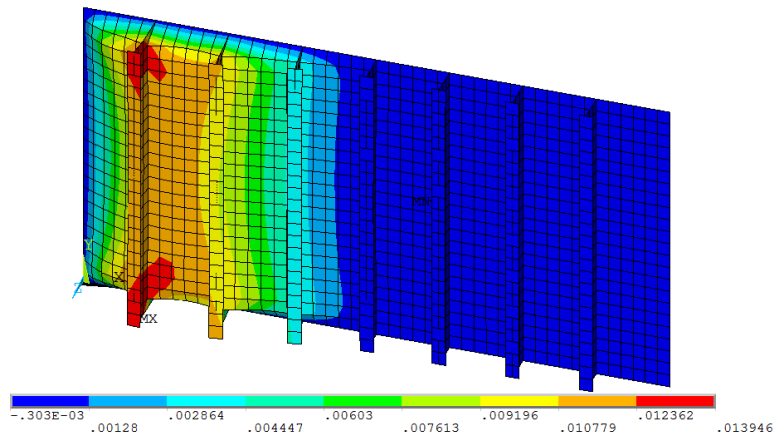
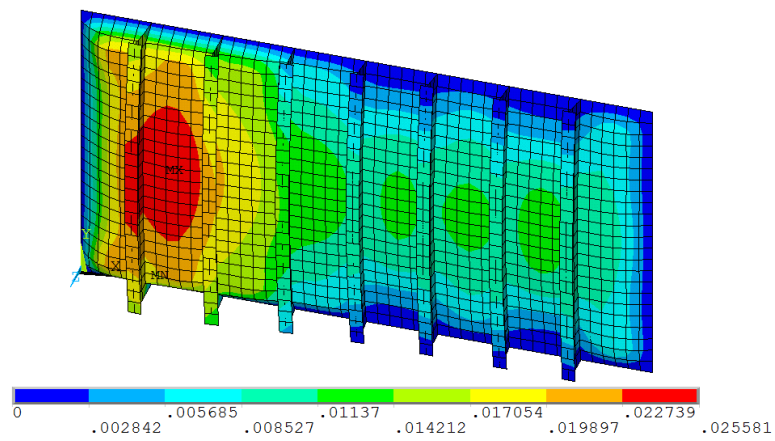
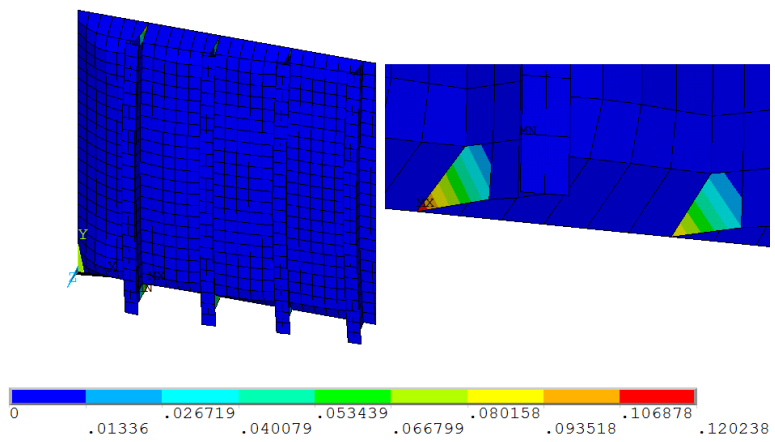


Figure B.9: Out of plane deformation (m) at original edge displacement, $h = 2.0 m$, $\delta = 0.9\delta_c$.



(a) Out of plane deformation (m)



(b) First principal plastic strain (-), inset shows other side of lower end of the panel.

Figure B.10: Structure after dynamic loading, $h = 2.0$ m, $\delta = 0.9\delta_c$.

B.3 Dynamic load analysis $h = 7.64$ m, breaking wave

The most extreme load degradation is a uniform dynamic load, as shown in Figure 5.3a. This simplified breaking wave is applied on the structure, the reaction forces are shown in Figure B.11. Differences in the configuration are explained for each point.

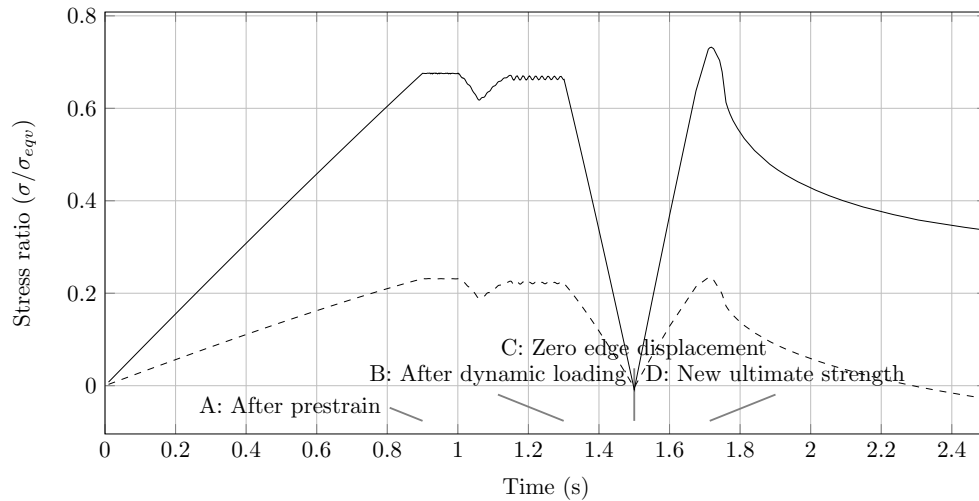


Figure B.11: Reaction forces over time normalized by the yield stress, due to compression of fore end. Dashed line is top end and solid line fore end, $h = 7.64$ m, $\delta = 0.9\delta_c$.

A: After prestrain Figure B.12 shows the structure after prestrain is applied. The out-of-plane displacement has the roughly the same shape as without the static impact load applied, see Figure 4.4a. Hence, the uniform load does not significantly change the deformation of the panel.

B: After dynamic loading Figure B.13 shows the structure after dynamic loading, but still under prestrain. The peaks are slightly larger, but have shifted to the edges of the panel. The wave impact has a low influence on the panel, confirmed by the reaction forces shown in Figure B.11.

C: Zero edge displacement Figure B.14 shows the structure without edge displacement. Small deformations are visible, 90% smaller than with the dynamic wave impact. The deformation are located at the outer edges of the panel, indicating that the plastic deformation is largest there. Hence, the uniform dynamic loading has shifted the deformations to plastic strains at the end of the panel.

D: New ultimate strength Figure B.15 shows the structure at its new ultimate strength. The deformation is very similar to the one shown in Figure 4.4a, both in magnitude and shape. The only difference is that the deformations with uniform dynamic loading are more spread out over the panel.

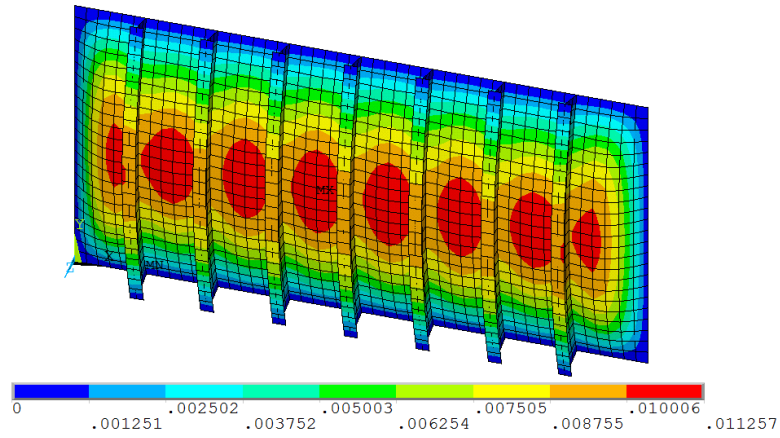


Figure B.12: Out of plane deformation (m) after prestrain, $h = 7.64$ m, $\delta = 0.9\delta_c$.

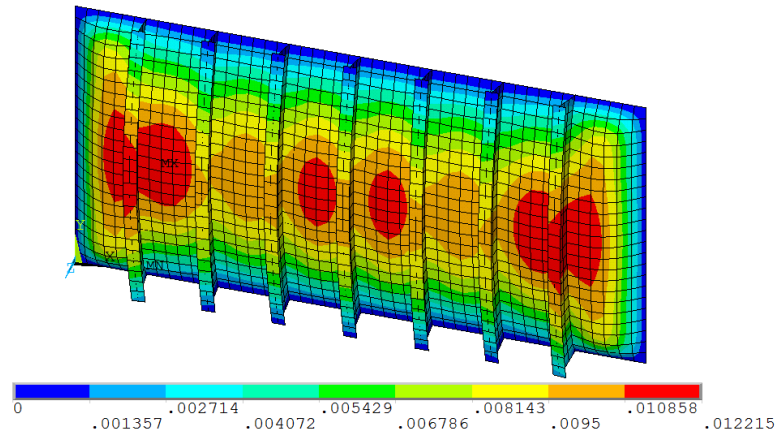


Figure B.13: Out of plane deformation (m) after dynamic loading, $h = 7.64$ m, $\delta = 0.9\delta_c$.

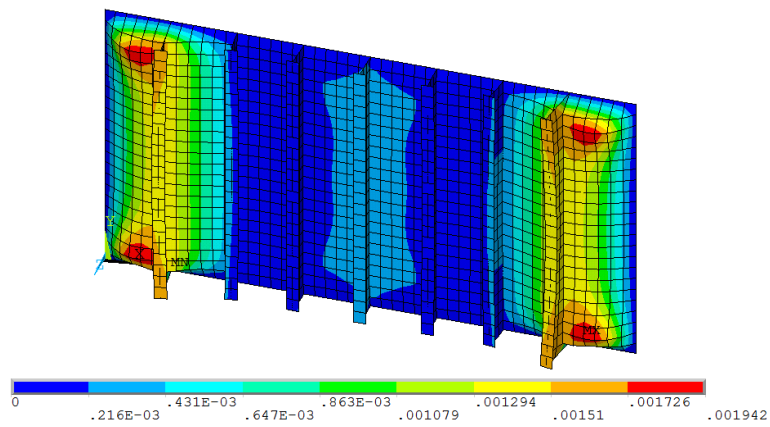


Figure B.14: Out of plane deformation (m) at original edge displacement, $h = 7.64$ m, $\delta = 0.9\delta_c$.

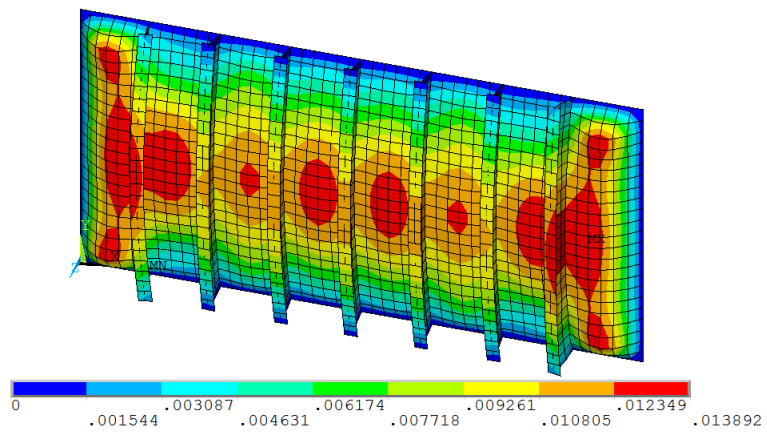


Figure B.15: Out of plane deformation (m) after dynamic loading, $h = 7.64$ m, $\delta = 0.9\delta_c$.

B.4 Dynamic load analysis $h = 0.1$ m, flip-through

The flip through wave impact is considered, with the finest resolution, see Figure 5.4f. Load direction is compression of the fore end, no displacement of top end. The normalized reaction forces over time are plotted in Figure B.16.

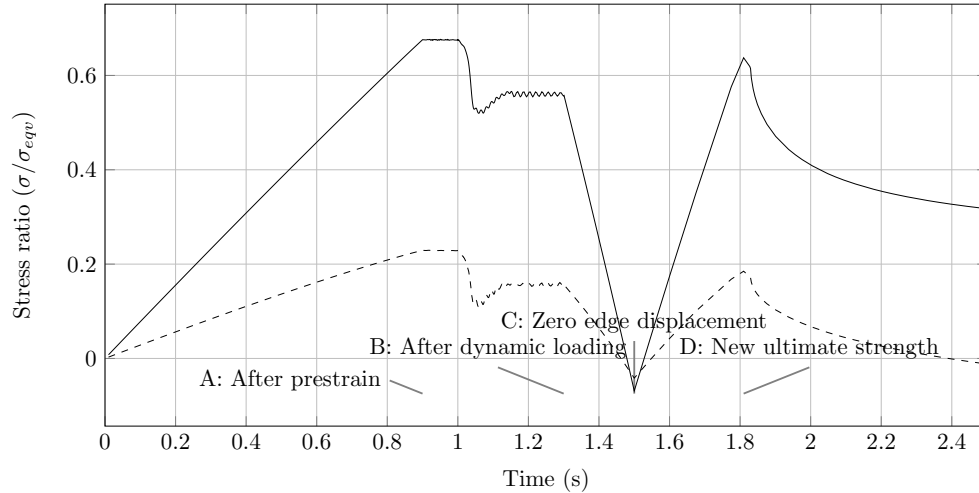


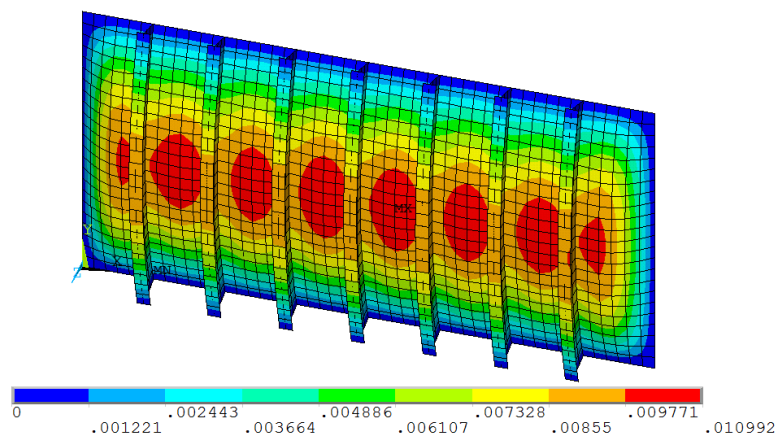
Figure B.16: Reaction forces over time normalized by the yield stress, due to compression of fore end. Dashed line is top end and solid line fore end, $h = 0.1$ m, $\delta = 0.9\delta_c$.

A: After prestrain Figure B.17 shows the structure after prestrain is applied. The deformation of the structure is much less localized than for the other wave load, because the first frame of the dynamic impact loading is very low. Small plastic strains are present, only on the edges of the stiffeners.

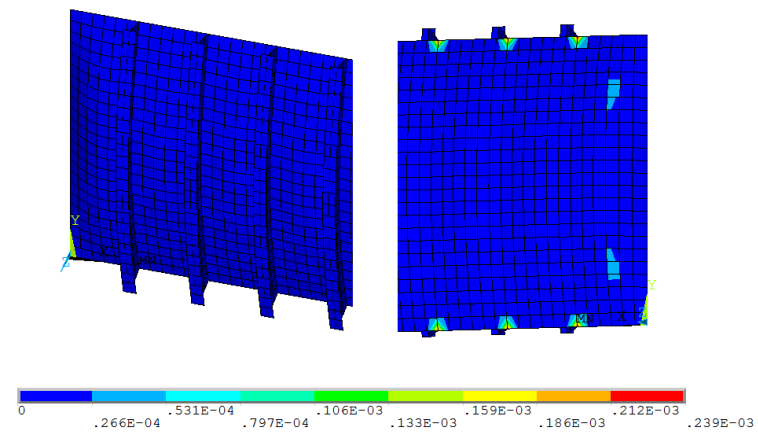
B: After dynamic loading Figure B.3 shows the structure after dynamic loading, but still under prestrain. In comparison with the other wave load, Figure B.2a, the displacements are at a lower position on the panel. This is in accordance with the impact point of the load, which is lower for the second wave load, compare Figure 5.3f with Figure 5.4f. Plastic strains are again only at the corners of the stiffeners.

C: Zero edge displacement Figure B.4 shows the structure without edge displacement. In comparison with the other wave load, the stiffener is more severely distorted, again explained by the impact location.

D: New ultimate strength Figure B.5 shows the structure at its new ultimate strength. The deformation of the structure is again most severe at the loaded stiffener, whereas the rest of the panel has roughly its unloaded failure mode.

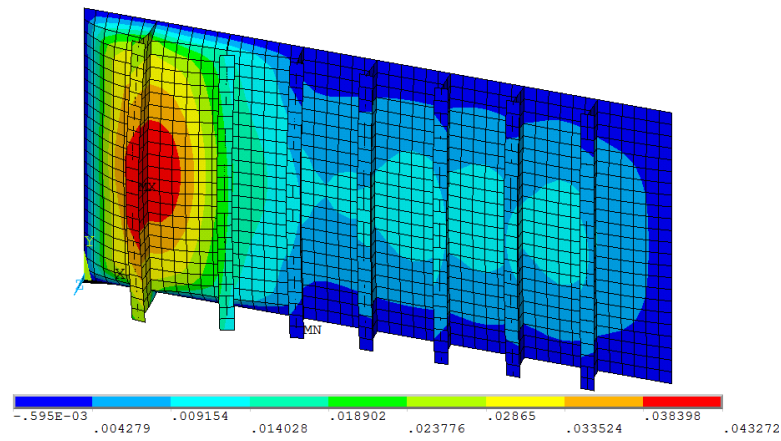


(a) Out of plane deformation (m)

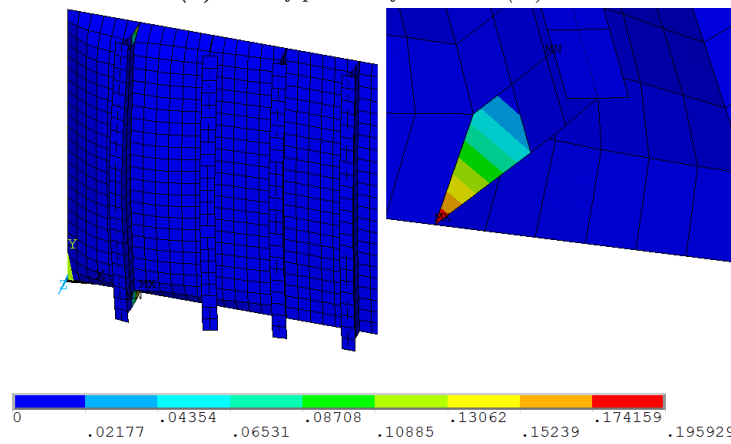


(b) First principal plastic strain (-), inset shows other side of lower end of the panel.

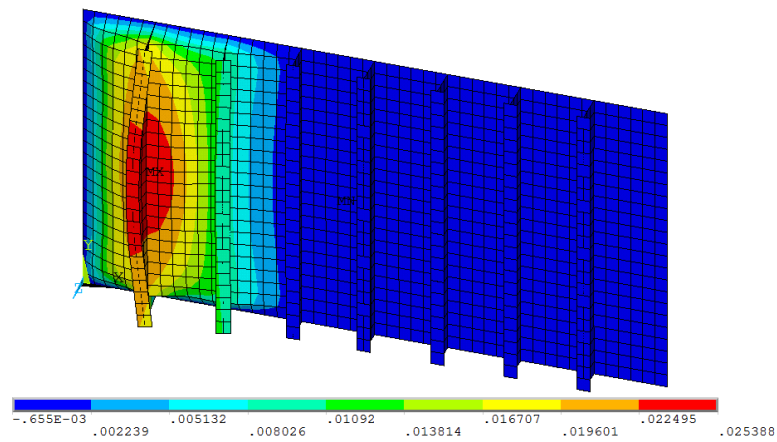
Figure B.17: Structure after prestrain, $h = 0.1 m$, $\delta = 0.9\delta_c$.



(a) Out of plane deformation (m)



(b) First principal plastic strain (-), inset shows other side of lower end of the panel.

Figure B.18: Structure after dynamic loading., $h = 0.1$ m, $\delta = 0.9\delta_c$ **Figure B.19:** Out of plane deformation (m) at original edge displacement, $h = 0.1$ m, $\delta = 0.9\delta_c$.

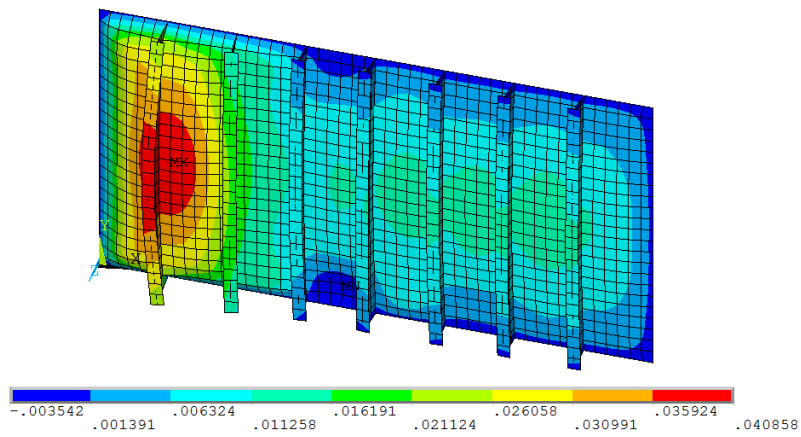


Figure B.20: Out of plane deformation (m) after dynamic loading, $h = 0.1 m$, $\delta = 0.9\delta_c$.

C Result tables

The tables below contain the data shown in Chapter 5: the new ultimate strengths determined after wave impact loading. The exact procedure is given in Section 2.4. All ultimate strengths represent a maximum reaction force due to displacement control. The reaction force is made dimensionless by Equation 2.2.

Table C.5: Data for $\delta = 0.8\delta_c$, with load simplifications from Figure 5.4.

α	h, s = 0.1, 0 m	h, s = 0.2, 0 m	h, s = 0.5, 0 m	h, s = 1, 0 m	h, s = 2, 0 m	h, s = 7.64, 0 m						
0	0.361	0.0606	0.363	0.0612	0.366	0.063	0.373	0.0666	0.388	0.0746	0.413	0.0845
30	0.344	0.27	0.337	0.246	0.346	0.261	0.34	0.265	0.36	0.263	0.395	0.272
45	0.338	0.372	0.337	0.372	0.339	0.363	0.337	0.332	0.349	0.362	0.378	0.325
60	0.3	0.536	0.298	0.536	0.296	0.539	0.293	0.543	0.319	0.487	0.33	0.371
60	0.149	0.655	0.151	0.655	0.155	0.657	0.163	0.661	0.188	0.68	0.254	0.743

Table C.6: Data for $\delta = 0.9\delta_c$, with load simplifications from Figure 5.4.

α	h, s = 0.1, 0 m	h, s = 0.2, 0 m	h, s = 0.5, 0 m	h, s = 1, 0 m	h, s = 2, 0 m	h, s = 7.64, 0 m						
0	0.346	0.0546	0.328	0.0534	0.332	0.0551	0.342	0.0593	0.362	0.0671	0.413	0.0845
30	0.328	0.273	0.327	0.273	0.323	0.274	0.319	0.244	0.338	0.268	0.395	0.272
45	0.328	0.368	0.328	0.368	0.327	0.37	0.326	0.373	0.342	0.358	0.385	0.351
60	0.294	0.531	0.295	0.532	0.294	0.535	0.293	0.54	0.299	0.533	0.354	0.447
60	0.144	0.645	0.147	0.646	0.15	0.646	0.155	0.645	0.175	0.656	0.236	0.73

Table C.7: Data for $\delta = 0.95\delta_c$, with load simplifications from Figure 5.4.

α	h, s = 0.1, 0 m	h, s = 0.2, 0 m	h, s = 0.5, 0 m	h, s = 1, 0 m	h, s = 2, 0 m	h, s = 7.64, 0 m						
0	0.327	0.0494	0.339	0.0529	0.335	0.053	0.323	0.0547	0.355	0.0653	0.413	0.0845
30	0.317	0.283	0.315	0.283	0.311	0.284	0.319	0.275	0.333	0.266	0.394	0.272
45	0.318	0.365	0.319	0.365	0.32	0.367	0.323	0.371	0.336	0.356	0.385	0.351
60	0.288	0.574	0.288	0.575	0.288	0.53	0.292	0.536	0.301	0.531	0.342	0.507
60	0.144	0.642	0.146	0.642	0.149	0.641	0.156	0.642	0.175	0.652	0.227	0.722

Table C.8: Data for $\delta = 0.9\delta_c$, with load simplifications from Figure 5.4 and panel from Table 5.1.

α	h, s = 0.1, 0 m	h, s = 0.2, 0 m	h, s = 0.5, 0 m	h, s = 1, 0 m	h, s = 2, 0 m	h, s = 7.64, 0 m						
0	0.393	0.0232	0.393	0.0232	0.387	0.0234	0.388	0.024	0.398	0.0242	0.381	0.0461
30	0.355	0.168	0.355	0.168	0.354	0.168	0.353	0.167	0.353	0.162	0.386	0.131
45	0.323	0.239	0.323	0.239	0.323	0.24	0.322	0.233	0.326	0.238	0.351	0.189
60	0.263	0.285	0.263	0.285	0.264	0.285	0.265	0.282	0.264	0.278	0.284	0.236
60	0.0214	0.25	0.0215	0.25	0.0216	0.25	0.0219	0.248	0.0275	0.336	0.0203	0.306